Title

High-Latitude Carbon Cycling: Improving Mechanistic Understanding of Heterogeneity and Change in Complex Ecosystems

Author

Shirley, Ian

Publication Date

2022

Peer reviewed|Thesis/dissertation

High-Latitude Carbon Cycling: Improving Mechanistic Understanding of Heterogeneity and Change in Complex Ecosystems

by

Ian Shirley

A dissertation submitted in partial satisfaction of the

requirements for the degree of

Doctor of Philosophy

in

Physics

in the

Graduate Division

of the

University of California, Berkeley

Committee in charge:

Dr. William J. Riley, Co-chair
Professor Edgar Knobloch, Co-chair
Professor Naomi Ginsberg
Professor Dennis Baldocchi

Summer 2022

High-Latitude Carbon Cycling: Improving Mechanistic Understanding of Heterogeneity and Change in Complex Ecosystems

Abstract

High-Latitude Carbon Cycling: Improving Mechanistic Understanding of Heterogeneity and Change in Complex Ecosystems

by

Ian Shirley

Doctor of Philosophy in Physics

University of California, Berkeley

Dr. William J. Riley, Co-chair

Professor Edgar Knobloch, Co-chair

High-latitude ecosystems play a key role in the global carbon cycle. There are large stocks of carbon stored in permafrost soils, protected by freezing temperatures and saturated soil conditions. However, the arctic is the fastest warming region on the planet, and as permafrost thaws much of the carbon will become vulnerable to microbial decomposition. At the same time, warming air temperatures, changing precipitation patterns, increasing nutrient availability, and rising CO_2 concentrations will lead to dramatic changes in vegetation dynamics and ecosystem carbon uptake. Because of strong feedbacks and system complexity, current estimates of the impact of climate change on regional net carbon balance are highly uncertain. Indeed, high-latitude carbon cycling was identified in the IPCC AR6 report as one of the largest sources of uncertainty in the global carbon cycle.

This thesis explores large- and fine-scale controls on high-latitude carbon cycling and examines uncertainties associated with regional estimates of carbon fluxes. This work relies heavily on *ecosys*, a process-rich mechanistic ecosystem model that has been extensively tested at high-latitudes. After a brief introduction, background on ecosystem ecology and the structure and process representation of *ecosys* is given. Then, an analysis on the large-scale controls on high-latitude carbon cycling, and how those controls will change with climate change, is presented through the lens of seasonality using *ecosys* simulations of Alaskan ecosystems. Next, key drivers of fine-scale variability of permafrost distribution, vegetation dynamics, and carbon cycling in a discontinuous permafrost watershed are identified using a sensitivity analysis of *ecosys*. Finally, machine learning models trained on *ecosys* outputs are shown to inaccurately predict both current and future high-latitude carbon balances.

Contents

List of Figures

List of Tables

Acknowledgments

Bill, thank you for your cheerful, insightful, and energetic guidance. Baptiste, thank you for your support and encouragement, your flexibility and curiosity, and for all of the trips to Alaska. Zelalem, I really appreciate all of the time you spent helping me to improve my research and my writing. Many thanks to Susan, Haruko, and Margaret for the many fruitful discussions early in my PhD that helped me to identify important questions related to high-latitude carbon cycling. I would also like to thank Stan Wullschleger and the NGEE Arctic project for supporting my studies and for making such a large research project feel open, inclusive, and exciting.

I'm very grateful to my co-advisor Prof. Edgar Knobloch for being so understanding and supportive of my research. To the other members of my committee - Prof. Naomi Ginsberg, Prof. Jonathan Wurtele, and Prof. Dennis Baldocchi - I truly appreciate your participation in my PhD and your willingness to engage with a dissertation topic that is unusual for the physics department. Thank you for all of your valuable input, and for being so gracious with your time.

Sebastian, John, Craig, Jack, Stijn, Chen, Sylvain, Carlotta, Hunter, Sebastien, Cristina, and Ori: thank you for all of the good times in Alaska. No matter the weather - rain, sun, snow, or mosquitoes - you all make fieldwork fun.

Jed, Jared, and Ben, thank you for your lasting friendship. Nicholas, thanks for the game nights and your incredible cooking. Ahmad, thank you for navigating PhD research, COVID lockdowns, and the aisles of Berkeley Bowl with me. I'm honored to call you my fellow grad student. Ioanna, thank you for all of your help and encouragement, for the hikes, road trips, and acrobatics, and for giving me fruit at Cafe Strada. You made these years into an adventure. Karl, thanks for all of the backpacking trips and burger nights, and for being such an important presence in my life. Mom, Dad, Annie, and Nate, thank you for your cheerful and grounded support. I couldn't ask for a better family.

Chapter 1

Introduction

Terrestrial ecosystems are an important, yet highly complex, component of the global climate system. Every year, about a third of the CO_2 emitted by humans is assimilated into vegetation and soil which, over the past decade, is about 3.4 Pg of carbon per year. This number is deceptively small, however, since the land CO_2 flux is the net result of two competing processes: photosynthesis, which converts light energy into chemical energy by fixing CO_2 into carbohydrates, and respiration, which breaks down sugars, proteins, and fats to provide energy for cellular activity in plants and microbes, releasing CO_2 in the process. In fact, 15% of the total CO_2 in the atmosphere (or about 120 Pg of carbon) cycles through terrestrial ecosystems each year. The controls on photosynthesis and respiration are completely different, and can change drastically from one hour and one patch of soil to the next. It is remarkable, then, that even in a strongly perturbed climate system these fluxes differ by only 3% across the globe.

Currently a negative feedback to climate change, terrestrial ecosystems dampen the warming effect of anthropogenic CO_2 emissions. However, only a relatively small shift in the balance between photosynthesis and respiration would be needed to switch the sign of this feedback. While CO_2 enters terrestrial ecosystems via photosynthesis, these systems have been net sinks of carbon for millenia, leading to substantial accumulation of soil carbon. The IPCC AR6 report [73] estimates that there are 3200-4100 Pg of carbon stored in the soil globally. For reference, there is currently 850 Pg of carbon in the atmosphere, and approximately 1500 Pg of carbon in global fossil fuel reserves. If changing conditions were to shift the balance towards respiration, there is enough carbon stored in the soil to sustain a positive feedback to climate change for a very long time.

Terrestrial ecosystems are intricate, interconnected, and dynamic systems. Energy, water, carbon, and nutrients are transferred and transformed as they flow through the soil-plant-atmosphere continuum. The mechanisms and controls of many of the important processes, when taken in isolation, are actually fairly well-characterized. In a controlled environment, for example, scientists can predict how the carbon fixation rate of a leaf, the flow of water through a soil column, and the amount of nitrogen released from organic matter upon decomposition will respond to changing conditions. Unpredictability arises when all of these

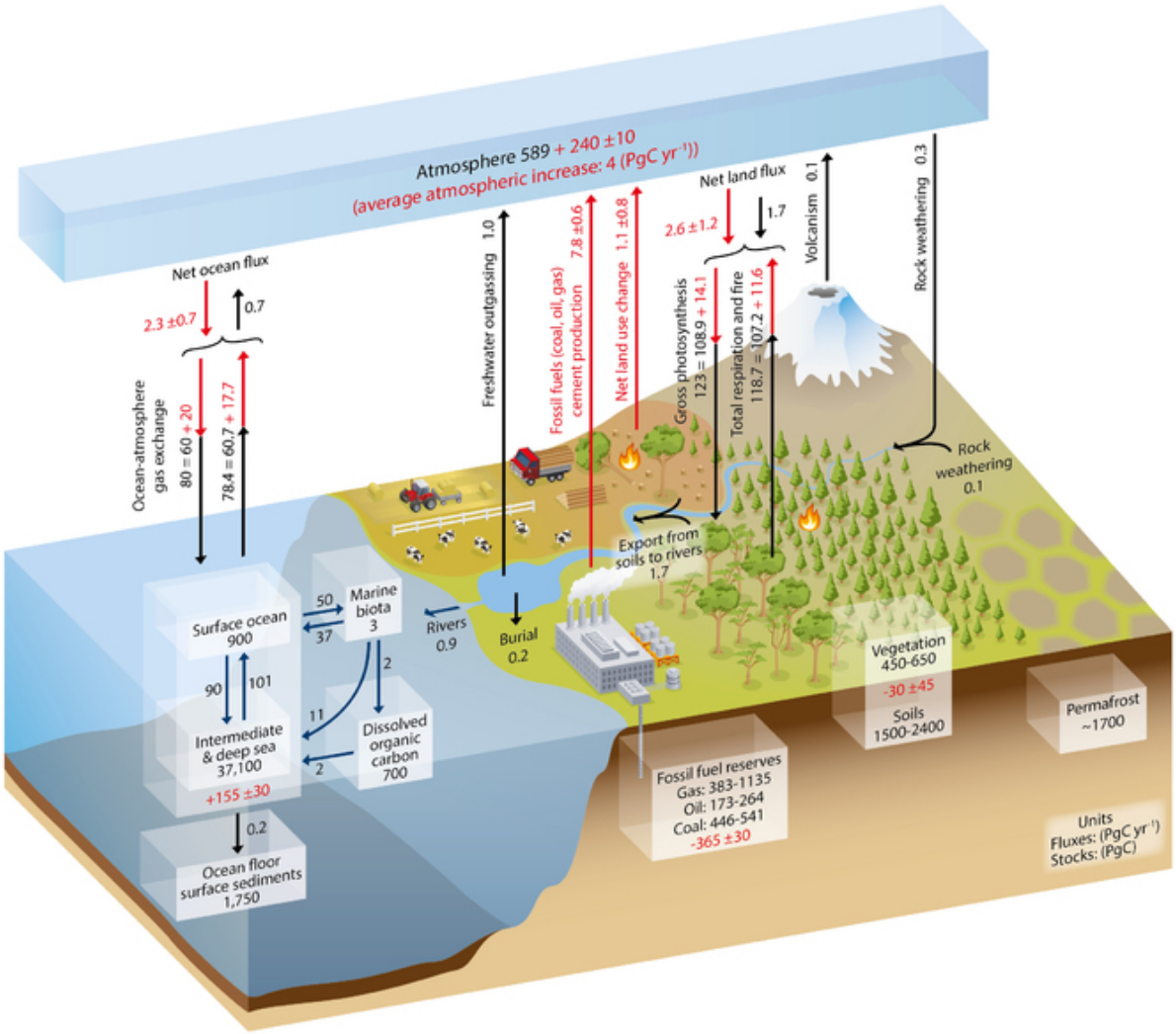

Figure 1.1: The global carbon cycle. Estimates from the IPCC 2013 report are shown for pre-industrial (black) and present-day (red) global carbon stocks (boxes) and annual fluxes (arrows). This figure is reproduced from [72].

processes are combined to form a living ecosystem. Energy, water, carbon, and nutrients cycle via many non-linear and strongly coupled processes that operate across an enormous range of temporal and spatial scales. An enzymatic reaction in the soil occurs in milliseconds, the rates of these reactions are sensitive to soil physical conditions (e.g., temperature, moisture) that change hourly, and the accumulation of these reactions change the structure of the top 10 cm - 1 m of soil over decades to millennia. While this complexity makes the system interesting to study, it also complicates attempts to predict how the net carbon balance of global ecosystems will shift in response to changes in air temperature, CO_2 concentration, and precipitation.

High-latitude ecosystems play an outsize role in the global carbon cycle. Approximately half of the global soil carbon stocks are stored in these systems. This carbon is protected from decomposition by cold temperatures and saturated soils. However, soil warming induced by climate change will potentially expose a substantial portion of these enormous carbon stocks to decomposition. Due to an effect called arctic amplification, the high-latitudes are expected to warm much more than the rest of the planet [145]. In fact, the region is already experiencing rapid change caused by anthropogenic warming [17, 144]. While the planet as a whole has warmed by about 1 ℃ since 1980, arctic temperatures have increased by 3 ℃ over the same period. Large changes to high-latitude ecosystem processes and characteristics attributed to this warming have already been observed (e.g., warming permafrost temperatures [151], lengthening growing seasons [6], and changing vegetation composition [155]) and these changes are expected to accelerate in the coming decades.

While high-latitude ecosystems are a very important component of the global carbon cycle, they are also remote and sparsely populated, with few people, few roads, and few powerlines. In the winter, temperatures are extremely cold and days are extremely short. And, there are bears. Historically, field research, data collection, and long-term monitoring have been more limited in these ecoystems than elsewhere in the world. Because of this, representation of high-latitude ecosystem processes is very poor in global climate models. In the IPCC AR6 report, the region is identified as one of the largest remaining sources of uncertainty in predictions of the response of the global carbon cycle to climate change:

> There is low confidence on the timing, magnitude and linearity of the permafrost climate feedback owing to the wide range of published estimates and the incomplete knowledge and representation in models of drivers and relationships [73].

This thesis was undertaken in order to improve understanding of high-latitude carbon cycling current and future climate conditions. Three guiding questions motivate the research presented here. First, what are the large-scale controls on high-latitude carbon balance and how will they be affected by climate change? Next, how does landscape structure control permafrost distribution and carbon flux heterogeneity at the watershed-scale? The second question is an acknowledgement of the large degree of variability in high-latitude ecosystems. Even if the large-scale controls on carbon cycling were well characterized, this variability would contribute to uncertainty in regional estimates of carbon balance. Such uncertainty

leads to the final guiding question: To what extent can information observable at large scales be used to infer high-latitude ecosystem processes, both now and in the future? Implicit in this question is a dichotomy between insights gained through observations and those gained through modeling. At present, regional carbon fluxes cannot be directly measured, so any estimate of high-latitude carbon balance must rely on both observations and models. However, disagreements frequently arise regarding the best types of observations, the best types of models, and appropriate balance between the two. Indeed, this tension shapes much of the discussion in this thesis.

Any attempt to answer the questions posed above will be faced with a number of challenges. Data availability for high-latitude ecosystems is very limited, particularly during the fall and winter. Further, these systems are highly complex, and large spatial and temporal heterogeneity that interacts across scales complicates both modeling and observational efforts to estimate high-level processes like ecosystem carbon balance. Finally, our current understanding and characterization of important high-latitude processes is both incomplete and not fully implemented in models.

The remainder of this thesis is organized into six sections. The next chapter provides a comprehensive description of the *ecosys* model, a process-rich, mechanistic terrestrial ecosystem model that is used throughout the thesis, along with some general background on terrestrial ecosystem ecology. In the third chapter, large-scale controls on the current and future high-latitude carbon cycle are investigated for each season of the year. The fourth chapter discusses heterogeneity in a transitional permafrost environment, and uses a sensitivity analysis of the *ecosys* model to rank the controls on watershed-scale variability in soil temperatures, vegetation dyanimcs, and carbon fluxes. In the fifth chapter, outputs from *ecosys* are used to evaluate the ability of machine learning models to upscale and forecast carbon fluxes across Alaska. Finally, the insights gained throughout the course of this research are summarized, and priorities for future data collection and model development in support of improved understanding of high-latitude carbon cycling are proposed.

Chapter 2

Background: Terrestrial ecosystem ecology and the *ecosys* model

Terrestrial ecosystem ecology is the study of the flows and transformations of energy, water, carbon, and nutrients that move through an ecosystem, which is composed of living organisms (primarily, typically, plants and microbes) and their physical environment. Energy first enters the system from the sun, water first enters the system from precipitation, carbon first enters the system from atmospheric CO_2, and nutrients enters the system either from the atmosphere (e.g., nitrogen) or the bedrock. However, as these components move throughout the ecosystem, they are transformed, transferred, and stored in different forms. For example, microbes primarily acquire energy from carbon structures that were created by plants, perhaps centuries before, and plants typically use nutrients that have been processed by microbial metabolisms. A high-degree of complexity arises in these systems because ecosystem processes interact with the controls that influence them. Soil temperature is a strong control over microbial activity, but is also affected by shading from the plant canopy. Water availability is a strong control over both plant and microbial activity, but increases in soil organic material affects soil drainage. Some controls are typically assumed to be purely external by terrestrial ecosystem ecologists. Hans Jenny, one of the pioneers of the field, identified five state factors that are external controls on ecosystem processes: climate, bedrock, topography, potential biota (i.e., what plants and animals are nearby), and time since disturbance (e.g., fire) [77]. However, ecosystem processes occur over a huge range of spatial and temporal scales. At the right scale, even these state factors can be affected by ecosystem processes.

An ecosystem model tracks the flows of energy, water, and carbon as they move throughout the system and are modified by ecosystem processes. There are a number of terrestrial ecosystem models currently deployed in the suite of global climate models that form the coupled model intercomparison projects (CMIP5, CMIP6) used in the IPCC reports. These models have widely varying levels of process representation, and key processes important to high-latitude carbon cycling, such as permafrost [19] and realistic nutrient cycles [33], are poorly represented in many of these models. While it has not been implemented in a global

climate model, the *ecosys* model is one of the most complex and process-rich mechanistic ecosystem models available today. In particular, mechanistic representation of soil physical and biogeochemical processes in *ecosys* is very advanced.

ecosys was developed by Robert Grant at the University of Alberta in the 1990s, with continual improvements over the past three decades. Development of *ecosys* has been guided by an intentional philosophy that prioritizes mechanistic representation of ecosystem processes. Model parameters are based on physical or biological processes and can be evaluated independently of the model, parameters function at smaller spatial and temporal resolution than is used for testing and prediction, and representation of physical and biological processes are detailed enough to allow for well-constrained tests.

In *ecosys*, an ecosystem is evolved through time using hourly meteorological inputs (air temperature, wind speed, radiation, humidity, and precipitation). The model is initialized with information about soil properties, topography, climate, and plant traits of multiple plant functional types (PFTs; e.g., sedge, moss, shrub). Ecosystem processes such as photosynthesis, respiration, transfers and transformations of heat, water, carbon, and nitrogen, are represented in a fully connected system from the atmosphere to the bedrock that includes a multi-layer plant canopy composed of multiple PFTs, snowpack, litter layer, and a soil profile. In each hourly timestep, the model simulates the following processes in the following order:

1. Soil energy balance, water, and heat fluxes
2. Microbial growth and respiration and other biological transformations of carbon and nutrients in the soil
3. Plant phenological changes
4. Plant canopy CO_2 uptake in absence of water limitation
5. Plant canopy energy balance and water uptake
6. Plant canopy CO_2 uptake under water limitation
7. Plant respiration and growth
8. Exchange of carbon and nutrients between roots and soil
9. Solute equilibria and gas and solute fluxes throughout soil profile

In the sections below, I give a comprehensive description of the processes outlined above. Energy, heat, and water fluxes and transformations are described in the first section, vegetation dynamics are described in the second section, and microbial dynamics and soil organic matter transformations are described in the third section. A summary of past evaluations of model performance is given in the final section. Additional detailed information on algorithms and parameterization of *ecosys* can be found in the Supplementary Material of Mekonnen et al (2019) [107].

2.1 Energy, Heat, and Water

Energy balance of plant canopy

Energy can be transferred between the plant canopy and the atmosphere via radiation, conduction, turbulent transfer of heat and water, and change in heat storage of the plant material itself. In each model step, these terms should all balance to zero. This is calculated as

$$R_N + S + LE + H = 0 \tag{2.1}$$

where R_{N} is the net radiation balance of the canopy, LE is the latent heat transfers from transpiration and evaporation from leaf surfaces, and H is the sensible heat transfer. These terms depends on temperature and water fluxes between the canopy and the atmosphere. In *ecosys*, this equation is balanced iteratively until convergence on first canopy temperature and then canopy water potential are reached.

In *ecosys*, radiation is divided into short wavelength (SW) and long wavelength (LW) components. The incoming SW component from the atmosphere is given by the weather file, and is split into direct and diffuse components depending on the sun angle. This radiation is scattered throughout the multi-layer and multi-species canopy, with reflection, absorption, and transmission calculated for each leaf and stem surface. Incoming LW radiation from the sky and soil is balanced against canopy emission of LW, each of which is determined by temperature using the Stefan-Boltzmann law,

$$R_{LW} = \epsilon \sigma T^4 \tag{2.2}$$

where ϵ is the emissivity of the ground, canopy, or atmosphere, σ is the Stefan-Boltzmann constant, and T is the temperature of the ground, canopy, or atmosphere.

The change in canopy heat storage is calculated as the change in temperature in a time-step multiplied by the heat capacity of the canopy. The canopy heat capacity is calculated from the carbon and water contents of all of the above-ground plant material.

The remaining heat fluxes from latent and sensible heat transfers occur because of turbulent transfer of heat and water between the canopy and atmosphere. This turbulence is created by the interaction of the plant canopy with surface winds and by heating of the surface which creates buoyant lift of air parcels and is incredibly complex. In practice, turbulent exchanges of heat, water and momentum generated by surface friction are approximated using gradient-diffusion theory, which assumes that vertical turbulent transport can be characterized as flow across a mean concentration gradient through a material characterized by a diffusivity. To simplify calculations in process models, this diffusivity is typically integrated into an aerodynamic resistance that can be calculated as a function of wind speed and canopy height. The aerodynamic resistance is modified to account for effects of buoyancy using the Richardson number, which is a dimensionless ratio of buoyancy-generated turbulence to shear-generated turbulence that can be estimated using modeled temperature and wind speed gradients. In *ecosys*, the aerodynamic resistance (r_a) is represented as

$$r_a = \frac{1}{1 - 10R_i} \frac{1}{k^2 u} \ln \frac{z - d + z_c}{z_c} \ln \frac{z - d + z_v}{z_v} \tag{2.3}$$

where R_i is the Richardson number, k is von Karman's constant, u is wind speed evaluated at height z, d is the zero-plane displacement height, and z_c (z_v) is the momentum (vapor) roughness parameter determined by vegetation height and structure. Turbulent fluxes of heat and water can then be calculated by dividing differences in canopy and atmospheric temperature and vapor density by the aerodynamic resistance. For example, the sensible heat flux is calculated as

$$H = \rho C_p \frac{T_a - T_c}{r_a} \tag{2.4}$$

where $/rho$ is the air density, C_p is the heat capacity of the atmosphere at constant pressure and T_a (T_c) is the temperature of the atmosphere (canopy).

Transpiration is the flux of water from inside the leaf to the atmosphere, so for this flux an additional resistance called the stomatal resistance. Stomata are pores that connect the internal cavity of leaves to the atmosphere. The size of the opening is controlled by guard cells in the leaf cell wall that react to soil water availability and photosynthetic demand for CO_2. In *ecosys*, stomatal resistance is first set in order to maintain a fixed internal-to-ambient CO_2 ratio, and then increased if canopy turgor is lowered by limited water availability [64].

Transfers and transformations of heat and water in the soil

In *ecosys*, the soil profile is divided vertically into 10-20 layers that increase exponentially in size with depth. Fluxes and transformations of heat and water are calculated in each soil layer at each time step. The energy balance of the soil or snow surface is calculated in a similar manner as for the plant canopy by balancing net radiation fluxes, latent heat exchanges from evaporation of surface water, sensible heat fluxes, and changes in heat storage. Heat is transferred via adjacent layers via conduction, which is calculated using Fourier's Law, and advection:

$$G_{i,j} = \kappa \frac{T_i - T_j}{\Delta z} + c_w T_i Q_{i,j} \tag{2.5}$$

where $G_{i,j}$ is the heat transfer between layer i and layer j, κ is the average thermal conductivity of the soil between layer i and layer j, T_i is the soil temperature of layer i, Δz is the vertical distance between the two layers, c_w is the heat capacity of water, and $Q_{i,j}$ is the water transfer between layer i and layer j. The thermal conductivity and heat capacity of each soil layer are determined in each time step using a function of the organic and mineral components, dry bulk density, water content, and temperature. Soil freezing (thawing) begins when the temperature of a soil layer falls below (rises above) a freezing point that is calculated using the soil layer water potential.

Water enters the soil column via precipitation, snow melt or water table exchanges. Water transfer between adjacent layers is calculated using hydraulic conductivity and potential differences:

$$Q_{i,j} = K(\psi_i - \psi_j) \tag{2.6}$$

where K is the hydraulic conductivity and ψ_i is the water potential of layer i. Soil pores can be large (macropores) or small (micropores) and water flow through the different sizes of pores behaves differently. Water transfer through micropores is calcuated using Darcy's equation, which is given by Equation 2.6 where the water potential is the sum of the matric water potential (created by attraction among water molecules and between water molecules and soil or root surfaces), osmotic water potential (created by gradients in salt concentrations), and gravimetric water potential (created by differences in height). Water transfer through macropores is simulated using Poiseuille–Hagen theory for laminar flow in tubes. This also takes the form of Equation 2.6, but only the gravimetric potential difference is used. The hydraulic conductivity of macropores is also much larger than that of the micropores.

Snowpack

In the version of ecosys used throughout this thesis, snowpack is modeled as a single uniform layer that contains snow, water, ice and gas. The density depends on snowpack thickness and on snow, ice, and water contents. Snowpack thermal conductivity is calculated using snowpack density, and heat capacity is calculated using snow, ice, and water contents. Phase changes within the snowpack can occur via precipitation inputs, melting, evaporation, and sublimation.

2.2 Vegetation Dynamics

Vegetation structure and plant traits

The plant community of an ecosystem is composed of any number of different species, ranging from one in monoculture systems like agriculture to 100 species per hectare in tropical rain forests. In ecosystem models, individual species are typically combined into groups characterized by similar growth forms, phenology (defined as the timing of events in plant development such as flowering, leaf-out, and senescence), and nutrient acquisition strategies known as plant functional types (PFTs). The PFTs of high-latitude ecosystems include deciduous and evergreen trees and shrubs, sedges and grasses, lichens, and mosses. *ecosys* is a dynamic global vegetation model (DGVM), meaning that PFTs (communities of individuals with identical traits) compete for light, water, and nutrients. Thus the vegetation composition is prognostic rather than prescribed, and varies throughout the course of the simulation in response to changing conditions.

The above-ground vegetation structure is composed of branches, stems, leaves, and flowers, and its primary functions are photosynthesis and reproduction. In *ecosys*, this structure

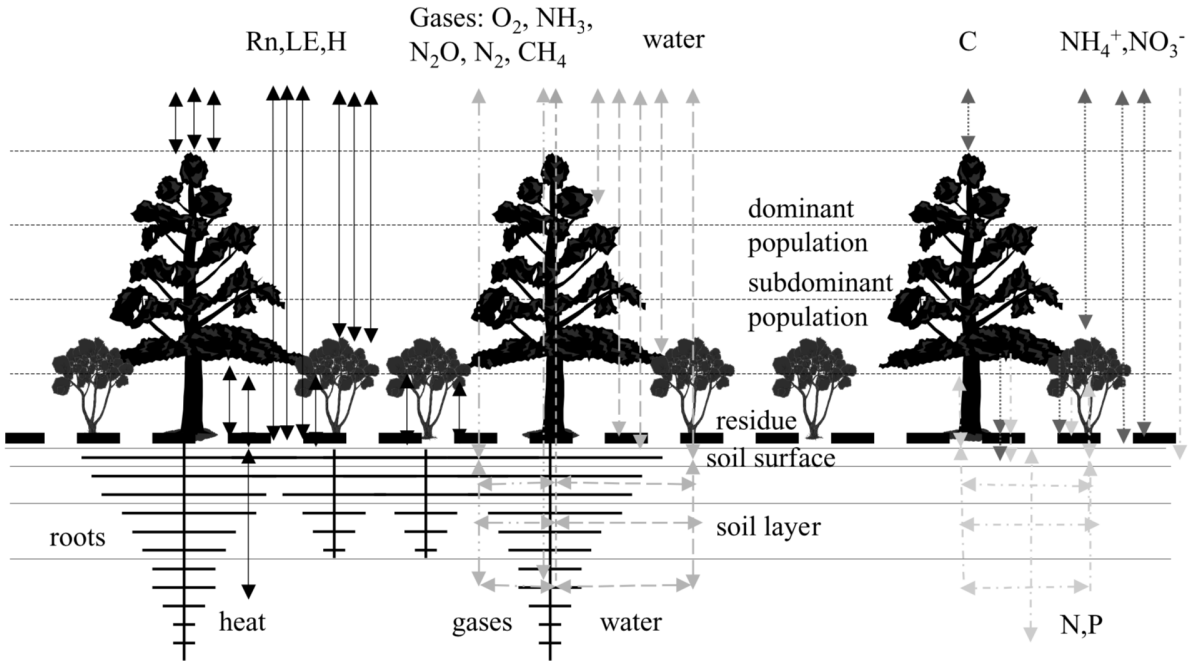

Figure 2.1: Ecosystem-atmosphere exchanges and subsurface transfers of heat, gases, water, carbon, nitrogen, and phosphorous simulated in ecosys. Reproduced from [50]

is distributed vertically among multiple PFTs and canopy layers through which radiation is transmitted, reflected, and absorbed (Figure 2.1). Each leaf is defined by its height, inclination, and azimuth, and a clumping factor parameter is used to simulate the evenness of the horizontal leaf distribution for each species. Other traits of the PFT canopy that need to be specified by the user include morphology (e.g., leaf area to mass ratio, branch length to mass ratio, branch angle, distribution of leaf inclination), leaf optical properties (transmissivity and albedo), phenology and growth strategies (e.g., leaf appearance rates, leaf-out and leaf-off requirements, deciudousness, plant carbon turnover, thermal adaptation), CO_2 fixation kinetics, and nutrient partitioning (C:N and C:P ratios under non-limiting conditions for each plant organ).

Below-ground vegetation structure is primarly used to acquire nutrients and water from the soil. In *ecosys*, the root system of each plant is a branched structure, with the primary root axes growing straight down into the soil profile, and secondary axes extending laterally in each soil layer (Figure 2.1). The user specifies a number of root system traits for each PFT. These include parameters related to morphology (e.g., root diameter, branching habit and frequency, and root porosity), water uptake (e.g., axial and radial root resistivity), active nutrient uptake, and associations of mycorrhizal fungi that fix atmospheric nitrogen.

Photosynthesis

In the cells of plant leaves, organelles called chloroplasts house the machinery that is used to convert light energy to chemical energy via photosynthetic carbon fixation. The process occurs in two stages: the light-dependent and light-independent reactions. In the light-dependent reaction, solar radiation is absorbed by chlorophyll in the thylakoid membranes of the chloroplasts, leading to excitation and release of electrons. The excited electrons travel down an energy gradient through a chain of proteins (the 'electron transport chain'). This processes generates the energy-rich organic compounds ATP and NADPH which are used to drive many cellular processes. In the light-independent reactions, also known as the Calvin cycle, the ATP and NADPH from the light-dependent reactions is used to synthesize six carbon sugars using atmospheric CO_2. This process relies on RUBISCO, an enzyme that fixes CO_2 to a five carbon sugar to generate two three carbon sugars. RUBISCO does not discriminate well between CO_2 and O_2, and frequently fixes oxygen to the five carbon sugar (oxygenation) instead of CO_2 (carboxylation). This leads to waste in a process known as photorespiration, which uses energy, releases CO_2, and does not produce sugars.

In *ecosys*, these processes are represented using the Farquhar biogeochemical growth model [43], which is commonly used in mechanistic representations of photosynthesis. This model calculates the maximum carboxylation rate based on (1) CO_2 availability and (2) solar radiation, and sets the actual carboxylation rate as the lesser of the two.

The maximum carboxylation rate based on CO_2 availability (V_C) is calculated for each leaf using Michaelis-Menten kinetics modified by competitive inhibition from O_2:

$$V_{\rm C} = V_{{\rm C}max}\frac{[{\rm CO_2}] - \Gamma}{[{\rm CO_2}] + k_{\rm O_2}(1 + [{\rm O_2}]/k_{\rm O_2})} \tag{2.7}$$

where V_{Cmax} is the leaf carboxylation rate in saturating CO_2 in the absence of O_2, and $[CO_2]$ ($[O_2]$) is the leaf concentration of CO_2 (O_2), k_{CO_2} (k_{O_2})is the Michaelis-Menten constant for CO_2 (O_2) in the absence of O_2 (CO_2). Γ is the CO_2 compensation point is the CO_2 concentration at which net CO_2 assimilation is zero, given by

$$\Gamma = 0.5[{\rm O_2}]\frac{k_{\rm CO_2}V_{{\rm O}max}}{k_{\rm CO_2}V_{{\rm C}max}} \tag{2.8}$$

where V_{Omax} is the leaf oxygenation rate in saturating O_2 in the absence of CO_2.

The maximum carboxylation rate based on solar radiation (V_J) is calculated according to a hyperbolic function of the radiation incident on each leaf:

$$V_J = JY \tag{2.9}$$

where J is the electron transport rate and Y is the carboxylation efficiency. J is given by:

$$J = \frac{(QR + J_{max} - (QR + J_{max})^2 - 4\alpha QRJ_{max})^{0.5}}{2\alpha} \tag{2.10}$$

where Q is the quantum yield, R is the photosynthetic photon flux density, J_{max} is the electron transport rate at saturating photon flux density, and α is an empirically determined shape parameter. Y is calculated by counting the number of photons needed for carboxylation and oxygenation, and is given by:

$$Y = \frac{[CO_2] - \Gamma}{4.5[CO_2] + 10.5\Gamma} \tag{2.11}$$

.

In *ecosys*, maximum rates for the two processes are set by (1) leaf rubisco content and (2) leaf chlorophyll content, both of which are determined from leaf protein content. Leaf temperature directly controls fixation rates through an Arrhenius temperature dependence of maximum rate constants, Michaelis Menten coefficients, and light-saturated electron transport rates, and a negative exponential temperature dependence of CO_2 and O_2 aqueous solubility. Arrhenius curves include low and high deactivation temperatures and a constant offset to account for the thermal adaptation of each PFT:

$$f_T = \frac{e^{(A-H_a)/(RT)}}{1 + e^{(H_{dl}-ST)} + e^{(ST-H_{dh})}} \tag{2.12}$$

where T is temperature of the reaction, A is a parameter such that $f_T = 1$ at 20 ℃, H_a is the energy of activation, H_{dl} (H_{dh}) is the energy of low (high) temperature deactivation, and S is the change in entropy of the reaction.

Carboxylation rates are also controlled by water potential (both directly and indirectly via stomatal effects on CO_2 availability) and nutrient availability (via reduction in leaf areal concentration of chlorophyll and rubisco and product inhibition of the activities of these molecules).

Plant water and nutrient uptake

Plant hydraulics in ecosystem models are typically represented as resistive systems, following Darcy's law as in the soil. Water potentials in the soil-plant-atmosphere continuum drop across roots, stems, leaves, and stomata, all of which are represented as resistive elements with varying conductivities. The total water uptake of a plant is calculated as the sum of the difference in water potential between the soil and the canopy divided by the total hydraulic resistance between the soil and the canopy for each root of the plant. The calculation of the hydraulic resistance is split into three components. The first is the radial resistance between the soil and the root surface, which is a function of water content, soil hydraulic conductivity, root radius, root length, and distance between adjacent roots. The second component is the radial resistance between the root surface and the root axis, which varies inversely with the length of the root. The third component is the axial resistance from the tip of the root to the stomata in the leaf, which is proportional to the path length and inversely proportional to the fourth power of the radius.

Plant nutrient uptake occurs in two stages. The first is transport of nutrients from the soil solution to the root surface. This can occur via mass flow, when nutrients are transported with water that is taken up by the root system, or via diffusion, when concentration gradients between the soil solution and root surface drive transport of nutrients. The second stage is active nutrient uptake by the root surfaces. In this process, proteins in the plant cell membranes selectively transport nutrients into the cells. This process requires energy, and is only performed if there is need for a specific nutrient. In *ecosys*, this process is simulated for three of the most important mineral nutrients for plant physiology: NH_4^+, NO_3^-, and $H_2PO_4^-$.

Plant growth, allocation, and senescence

Sugars produced during photosynthesis are stored in non-structural pools in the branches. Concentration gradients between carbon reserves in branches and roots drives transfer of carbon throughout the plant structure, with conductance between proportional to the axial distance between the reserves. The stored energy in these sugars is used to maintain existing plant structures, to grow new branches, leaves, flowers, and roots, and to drive active nutrient uptake from the soil.

Respiration of stored carbon reserves in each organ is an Arrhenius function of temperature as in Equation 2.12. In roots, respiration rates are also controlled by oxygen availability. The energy produced from this respiration is first used to maintain of existing plant structures. Energy requirements for this purpose are calculated using a temperature-dependent function of the nitrogen stored in each plant organ. Energy remaining after maintenance respiration needs are met is used to drive growth of above- and below-ground biomass according to phenology-dependent partitioning coefficients and organ-specific growth yields.

Allocation of carbon and nutrients in *ecosys* follows the philosophy of the Thornley model [158]. Carbon enters the plant from the leaves, and nutrients enter the plant via the roots. In the Thornley model, carbon and nutrients move between above- to below- ground pools according to concentration gradients that are created by mismatch between uptake and consumption. In *ecosys*, the potential transfer of carbon from each above-ground pool to each below-ground pool is calculated to balance the carbon concentrations of the two pools [51]:

$$C_{s,i,c} - F'_{i,c} = C_{r,i,c} + F'_{i,c} \tag{2.13}$$

where $C_{s,i,c}$ ($C_{r,i,c}$) is the ratio of stored carbon to total carbon of the i^{th} shoot (root) pool and $F'_{i,c}$ is the potential transfer of carbon between the two pools. The actual transfer of carbon is slowed by a rate constant K:

$$F_{i,c} = K_i F'_{i,c}. \tag{2.14}$$

The rate constant K_i between the shoot and root carbon pool varies with conductance between the leaf and root, which is proportional to the root cross-sectional area, and inversely proportional to the root length. Transfer of nutrients between roots and shoots follows a

similar algorithm, except that the relevant concentration is the ratio of stored nutrients to stored carbon in each pool.

The approach to simulation of carbon and nutrient allocation outlined above allows the modeled plant to respond realistically to variations in environmental conditions. For example, low nutrient concentrations in roots create imbalances that drive carbon transfer from shoots to roots, leading to prioritization of root growth and nutrient acquisition. Conversely, high nutrient concentrations in roots create imbalances that drive nutrient transfer from roots to shoots, leading to prioritization of above-ground structure growth and increased photosynthesis. Allocation is also affected by a number of other environmental factors in *ecosys*, including temperature, water, and oxygen availability, that slow or accelerate respiration of carbon reserves (used to drive growth or maintenance of existing plant structures) in shoot and root pools. For example, in dry conditions, the water potential of above-ground material is lower than root water potential, such that above-ground respiration slows relative to below-ground respiration. This results in carbon transfer from above-ground to below-ground and relative increase in root growth, facilitating increased plant water uptake.

Different plants allocate carbon and nutrients differently. In *ecosys*, these differences are created by plant traits that are input parameters in the model. For example, optimal ratios of carbon to nutrients that can be set for each plant organ lead to different relative nutrient demands for plant growth, and variation in root porosity leads to different root oxygen availability (and therefore respiration rates) under saturated soil conditions.

If photosynthesis is slowed by cold temperatures, low light, dry conditions, or nutrient limitations, plant carbon reserves will decline. When the reserves drop so low that plant respiration rates are lower than required for maintenance needs, carbon and nutrients are pulled from leaves and roots to meet those needs, leading to senescence of those organs. Only a portion of the carbon and nutrients in each leaf and root can be recovered in this way, and the rest is lost to the soil or ground surface in the form of litterfall.

2.3 Microbial Dynamics and Soil Organic Matter Transformations

Soil hierarchical biological organization

In natural ecosystems, soil organic matter is strongly variable in spatial distribution, structure, nutrient content, and lability (amenability to decomposition). Microbial populations are similarly variable, responding to spatial and temporal variations in soil organic matter properties and the physical conditions in the soil such as temperature and water availability. In *ecosys*, this variability is represented using a hierarchical organization of soil biological material. In each soil layer, there are five top-level complexes of organic matter and associated microbial populations: coarse woody plant litter, fine non-woody plant litter, animal manure, particulate organic matter, and humus (the most recalcitrant pool of organic matter). Five organic states are associated with each of these complexes: solid organic matter,

soluble organic matter, sorbed organic matter, microbial biomass, and microbial residues. Each organic state in each complex is divided into different structural or kinetic components that are characterized by varying susceptibility to decomposition. For each of these components, elemental fractions of carbon, nitrogen, and phosphorous are tracked in the model.

Microbial growth and metabolism

Organic matter transformations begin with hydrolysis, in which soil organic matter is broken into pieces of soluble organic matter small enough to be absorbed by microbes. This process is facilitated by excocelluar enzymes generated by microbes. In *ecosys*, the activity of these enzymes is assumed to be directly related to the active microbial biomass of each organic matter complex. Hydrolysis rates (D) are determined using a Michaelis-Menten function of the substrate concentration with a constraint that slows hydrolysis when microbial densities are high, as when soil water is limited:

$$D = M_C \frac{D_s[S]}{[S] + K_h(1 + [M]/K_i)} \tag{2.15}$$

where M_C is the microbial carbon associated with the organic matter complex, D_s is the specific decomposition rate of the complex at 30 ℃, $[S]$ is the substrate concentration, K_h is the Michaelis-Menten constant for hydrolysis, K_i is an inhibition constant, and $[M]$ is the concentration of microbial biomass in the soil water. Hydrolysis rates are additionally modified by an Arrhenius function of soil temperature, as in Equation 2.12. The soluble organic matter produced by hydrolysis can adsorb to, or desorb from, soil surfaces, be exported from the model cell, or be absorbed by microbial populations. Adsorption and desorption is calculated in the model using the Freundlich equation:

$$A = k_{ts} a F [Q]^b - X \tag{2.16}$$

where k_{ts} is the equilibrium rate constant for sorption, a is the total substrate + microbial residue carbon, F is the equilibrium ratio between hydrolysis and humification, and $[Q]$ is the soil solution concentration of hydrolysis products, and X is the mass of adsorbed hydrolysis products. Export of dissolved organic matter follows the movement of soil bulk water.

Dissolved organic matter taken up by microbial populations is used for metabolism and growth. Microbial respiration (R_h) is constrained by the concentration of soluble hydrolysis products:

$$R_h = M_C R_{G0} \frac{[Q]}{[Q] + k_G} \tag{2.17}$$

where R_{G0} is the aerobic respiration under non-limiting substrate availability at 30 ℃ and k_G is the Michaelis-Menten coefficient for microbial respiration. Microbial aerobic respiration is also constrained by oxygen availability, soil water potential, and soil temperature. This respiration is first used for maintenance of existing microbial populations (R_M, the energy

needs of which are determined by the nitrogen content of the microbial population and the temperature of the soil:

$$R_M = R_{M0} M_N f_T \tag{2.18}$$

where R_m0 is the specific maintenance respiration of the microbial population at 30 ℃, M_N is the nitrogen content of the microbial population, and f_T is an exponential function of soil temperature. Any remaining energy is used for growth of active microbial biomass. Microbial decay (D) is calculated as a first-order function of active microbial biomass:

$$D = D_0 M_C f_T \tag{2.19}$$

where D_0 is the specific decomposition rate of the microbial population at 30 ℃. Additional microbial decay occurs when uptake of dissolved organic matter is insufficient to maintain existing active microbial biomass. The change of microbial biomass in each time step is equal to the carbon taken up by a microbial population minus the carbon lost to maintenance and growth respiration and decay:

$$\frac{\delta M_C}{\delta t} = U - R_h - D \tag{2.20}$$

where U is the carbon taken up in each time step. Some of the carbon, nitrogen, and phosphorous from microbial decay is recycled and reused by the active microbial population, and the rest is split between the dissolved organic, humus, and microbial residue pools.

Microbial need for nitrogen and phosphorous changes with population growth and decay. Each microbial population is characterized by set C:N and C:P ratios, and nitrogen and phosphorous are either taken up (immobilization) or released (mineralization) with changes in biomass in order to maintain these fixed ratios. Microbial immobilization of nitrogen and phosphorous is limited by availability the the soil solution, and if a microbial population does not take up enough nutrients, the respiration and consequent energy availability of that population is reduced. These nutrient dynamics assoicated with changes in microbial populations change concentration of mineral nutrients in the soil solution and strongly affect the availability of nutrients for plant uptake.

11 different microbial functional guilds (bacteria and fungi) with different metabolic pathways and traits are represented in *ecosys*. Aside from aerobic microbes (which reduce O_2 and produce CO_2), nitrifiers and denitrifiers oxidize and reduce nitrates [109], diazatrophic microbial populations in the soil or associated with plant roots transform atmospheric N_2 into NH_4^+ [54], and fermenters, methanogens, and methanotrophs are all involved in the production and consumption of methane in the soil [52, 53].

2.4 Definition of Common Terms

- Microbial respiration (R_h) is the total respiration by all microbial populations in all soil layers.

- Gross primary productivity (GPP) is the total amount of carbon fixed by all plant species.
- Autotrophic respiration (R_a) is the total amount of carbon respired by all plant species.
- Net primary productivity (NPP) is GPP minus R_a
- Net ecosystem exchange (NEE) is the total amount of carbon exchanged between the ecosystem and the atmosphere: NPP + R_h. Net carbon uptake by the ecosystem is defined as negative NEE.

2.5 Model Evaluation

ecosys representation of ecosystem carbon, nutrients, energy, and hydrological dynamics has been tested in many high-latitude sites. For example, modeled active layer depth matched long-term measurements at 28 Circumpolar Active Layer Monitoring sites ($R^2 = 0.63$; RMSE = 10 cm) [106], modeled North American tundra gross primary production (GPP) matched upscaled EC tower measurements (geographically weighted regression, $R^2 = 0.78$) [103], modeled tree composition of the Alaskan boreal forest agreed well with LANDFIRE–FCCS maps [107], and modeled NEE agreed well with EC tower measurements at twelve North American tundra and boreal sites ($0.6 < R^2 < 0.9$) [59, 58, 55, 61]. Additionally, *ecosys* accurately captured thermal and biological dynamics of short-term soil warming experiments at four sites across Alaska [16]. Fifteen studies of *ecosys* performance in high-latitude systems are described in Table 2.1.

Reference	Study Area	Study Years	Metric	Data Product	R^2	RMSE
[59]	Boreal Region, Canada	1998 - 2006	Hourly CO_2 Flux	Site Measurements	0.57 - 0.87	1.2 - 3.8 m^{-2} s^{-1}
[58]	Daring Lake	2004 - 2007	Measured CO_2 Fluxes	Site Measurements	0.69 - 0.78	0.59 - 0.69 m^{-2} s^{-1}
[58]	Daring Lake	2004 - 2007	Gap-filled CO_2 Fluxes	Site Measurements	0.64 - 0.85	NA
[58]	Daring Lake	2004 - 2007	Measured LE Fluxes	Site Measurements	0.7 - 0.81	27 - 30 W m^{-2}
[55]	Daring Lake	2005 - 2009	Mixed Tundra Hourly CO_2 Flux	Site Measurements	0.72 - 0.83	0.61 - 0.69 m^{-2} s^{-1}
[55]	Daring Lake	2006 - 2009	Fen Hourly CO_2 Flux	Site Measurements	0.71 - 0.79	0.57 - 0.72 m^{-2} s^{-1}
[60]	Barrow, AK	2013	LCP CO_2 Flux	Site Measurements	0.7	1.07 umol m^{-2} s^{-1}
[60]	Barrow, AK	2013	LCP CH4 Flux	Site Measurements	0.86	0.047 umol m^{-2} s^{-1}
[60]	Barrow, AK	2013	FCP CO_2 Flux	Site Measurements	0.88	0.96 umol m^{-2} s^{-1}
[60]	Barrow, AK	2013	FCP CH4 Flux	Site Measurements	0.93	0.008 umol m^{-2} s^{-1}
[61]	Barrow, AK	2013	LCP Soil Water Content	Site Measurements	0.44	0.05 m^3 m^{-3}
[61]	Barrow, AK	2013	FCP Soil Water Content	Site Measurements	0.72	0.09 m^3 m^{-3}
[61]	Barrow, AK	2013	Rn	Site Measurements	0.97	NA

[61]	Barrow, AK	2013	LE	Site Measurements	0.76	6 W m^{-2}
[61]	Barrow, AK	2013	H	Site Measurements	0.78	9 W m^{-2}
[61]	Barrow, AK	2013	G	Site Measurements	0.58	NA
[103]	Arctic	1982–2010	GPP	FLUXCOM	0.78 (GWR)	NA
[104]	Arctic Tundra	1980-2010	Interannual variation in max LAI/NDVI	AVHRR NDVI3g	0.71 (GWR)	NA
[23]	Stordalen Mire, Sweden	2003-2007	Thaw Depth	Site Measurements	0.41-0.93	NA
[23]	Stordalen Mire, Sweden	2003-2007	3-hourly CO_2 Flux	Site Measurements	0.48-0.64	8.4 - 19.1%
[23]	Stordalen Mire, Sweden	2003-2007	3-hourly CH4 Flux	Site Measurements	0.31-0.44	11.1 - 16.4%
[24]	Stordalen Mire, Sweden	2011-2013	CH4 Flux	Site Measurements	0.38 - 0.46	NA
[56]	Barrow, AK	2015	Soil Temperature at 10 cm	Site Measurements	0.92	NA
[56]	Barrow, AK	2014-2015	Rn	Site Measurements	0.93-0.95	NA
[56]	Barrow, AK	2014-2015	LE	Site Measurements	0.71 - 0.77	9 - 13 W m^{-2}
[56]	Barrow, AK	2014-2015	H	Site Measurements	0.85 - 0.88	8 - 16 W m^{-2}
[56]	Barrow, AK	2014-2015	G	Site Measurements	0.57 - 0.72	5 W m^{-2}
[62]	Barrow, AK	2014-2015	Hourly CO_2 Flux	Site Measurements	0.41 - 0.55	1.04 - 1.57 umol m^{-2} s^{-1}

[62]	Barrow, AK	2014	Hourly CH4 Flux	Site Measurements	0.47	NA
[107]	Alaska boreal region	Present Day	Evergreen Tree Relative Dominance	LANDFIRE–FCCS	0.77 (GWR)	NA
[107]	Alaska boreal region	Present Day	Deciduous Tree Relative Dominance	LANDFIRE–FCCS	0.65 (GWR)	NA
[107]	Alaska boreal region	2003	Energy fluxes across stand age fire chronose-quence sites	Site Data	0.52 - 0.79	NA
[107]	Alaska boreal region	2003	CO_2 fluxes across stand age fire chronose-quence sites	Site Data	0.59 - 0.73	NA
[16]	Alaska		ALD, Change in Reco, Change in GPP	Site Measurements	NA	NA
[16]	Stordalen Mire, Sweden	2012-2017	Temperature hysteresis of CH4 Flux	Site Measurements	NA	NA
[106]	North Slope of Alaska	1990-2018	ALD	CALM	0.63	10 cm
[106]	North Slope of Alaska	1990-2018	ALD	Nicolsky et al 2017	0.68 (GWR)	NA

[108]	Seward Peninsula, AK	2016	Shrub Biomass across Hillslope	SIte Measurements	0.89	NA

Table 2.1: Previously published comparisons of *ecosys* with site and regional data products at high-latitudes. R^2 and Root Mean Square Error (RMSE) are included when reported in the reference.

Chapter 3

Large-scale controls on high-latitude carbon balance throughout the 21st century

Conditions for plant and microbial activity are particularly harsh at high-latitudes and the region is characterized by low plant productivity and slow rates of microbial decomposition. Climate change will lead to drastic changes in these conditions via shifts in air and soil temperatures, radiation, nutrient availability, and the water cycle. This chapter describes how these shifting large-scale controls will change high-latitude carbon cycling. Site observations and regional observation-based estimates of carbon fluxes are used to evaluate *ecosys* model performance across Alaska. A current discrepancy between process-model and some recently published observation-based estimates of high-latitude carbon balance is discussed. Then, an analysis of the controls on changes in R_h, NPP, and NEE throughout the 21st century is presented for each season. The text and figures in this chapter are excerpted from [148],

3.1 Introduction

Surface air temperature and solar radiation exhibit strong seasonality and shape seasonal and annual cycles of plant and microbial activities in high-latitude ecosystems [42]. Late snowmelt, cool summers, and short autumn days lead to short and relatively unproductive growing seasons [13, 42], and frozen soils and harsh winters inhibit organic matter decomposition [110]. The high latitudes are particularly susceptible to anthropogenic climate warming [145], and recent rapid increases in air temperature are projected to accelerate throughout the 21st century [17, 144]. This climate warming will shift the relative effects of temperature and radiation limitations on biological activity, and therefore the carbon cycle (Figure 3.1). While previous modeling and observation-based studies have demonstrated that climate warming will induce increased carbon fixation and a longer growing season at high-latitudes

[8, 46, 74, 157], the impacts of climate change on the seasonality of high-latitude carbon cycling remain uncertain.

The amplitude of the seasonal cycle of atmospheric CO_2 concentrations in northern latitudes has been increasing steadily over the past 50 years and has been explained by changes in the seasonality of the terrestrial carbon cycle [65]. Earlier leaf-out in the spring [29, 174, 177] and higher productivity and allocation to woody biomass during the summer [92, 103] increase the regional carbon sink strength. Fall and winter soil warming increases regional carbon losses due to higher microbial respiration rates [29, 118, 124]. The sum of these seasonal changes, which represents the balance between climate induced changes in vegetation productivity and microbial activity, has important implications for the global carbon cycle as the large organic carbon stocks stored in permafrost soils [143] have the potential to drive important climate feedbacks [46, 135].

Model predictions of current high-latitude ecosystems mostly suggest that they are net carbon sinks [8, 74, 100], while several recent observation-based studies indicate the opposite. For example, Natali et al [118], using machine learning to spatially and temporally extrapolate high-latitude measurements, predicted higher fall and winter regional carbon losses than did a suite of process-models for the years 2003-2017. The non-growing season losses predicted by Natali et al [118] are also larger than the growing season uptake predicted by the process-models. Commane et al [29], using aircraft observations and upscaled eddy covariance measurements, argued that high rates of fall respiration caused Alaska to be a carbon source between 2012 and 2014. These discrepancies between process-model predictions and observation-based estimates raise concerns that missing or misrepresented cold-season mechanisms could bias process-model predictions of high-latitude ecosystem responses to climate change. Consideration of seasonal changes in carbon fluxes is needed to disentangle mismatches between modeling and observation-based studies, to provide insight into driving forces behind model results, and to identify important measurements needed to evaluate and build confidence in model predictions.

Here, we examine climate change impacts on Alaska carbon cycle seasonality using *ecosys*. This study is also motivated by the large reported differences in process-model and observation-based assessments of carbon cycle seasonality dynamics, particularly during the fall and winter [29, 118, 174, 177]. Because of its rich process representations (i.e., process-specific temperature cutoffs and activation energies that can represent low-temperature biogeochemical activity and climate-change acclimation, mineralization and plant nutrient uptake that is driven by availability and capability rather than photosynthetic activity), *ecosys* is well-suited to address these questions. After further evaluating the model and showing it is broadly consistent with recent site- and regional-scale observations (including those mentioned above), we apply it to analyze processes that control seasonality of plant and microbial activity, and explore how these controls are expected to change over the 21$^{\text{st}}$ century and how these changes will affect regional carbon budgets.

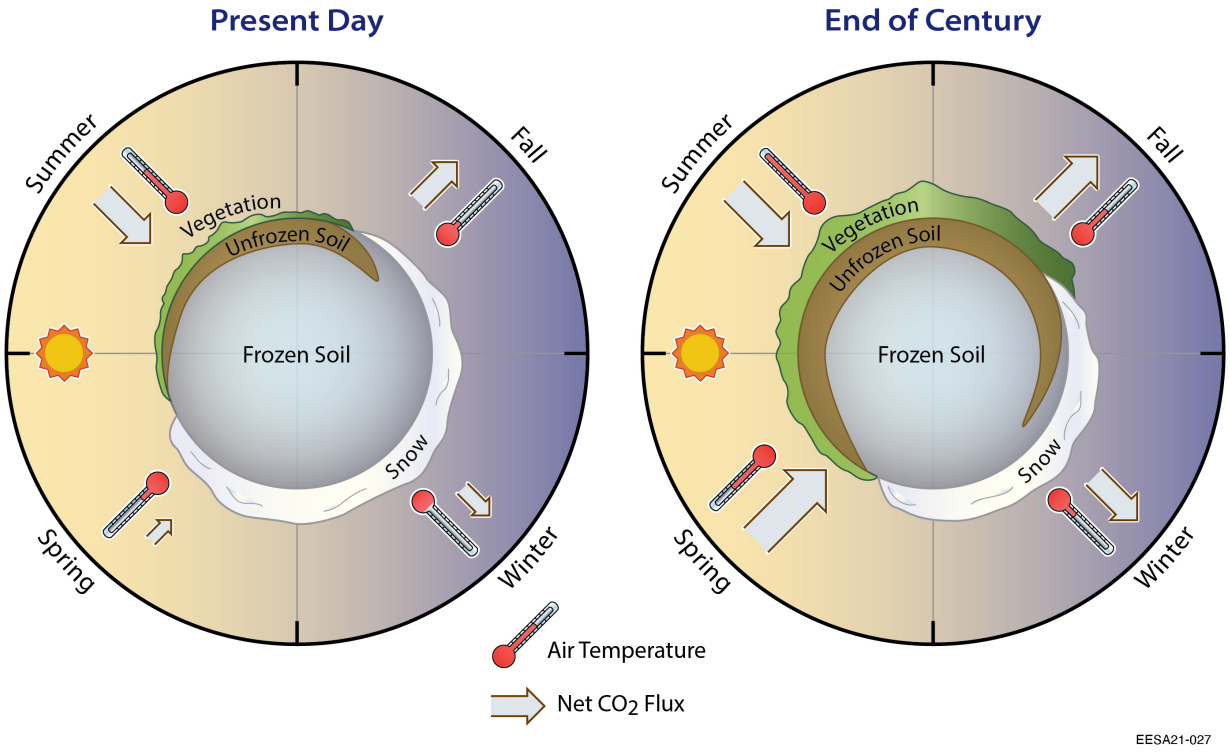

Figure 3.1: 21st century climate warming will shift the seasonality of the carbon cycle across Alaska. As depicted in this schematic, there will be important changes to the seasonality of high-latitude NEE throughout the 21st century. Relaxation of temperature limitation to plant productivity will cause large increases in spring net carbon uptake. Warming air and soil temperatures, coincident with persistent radiation limitation to plant productivity, will cause large increases in fall and winter net carbon losses. Summer net carbon uptake also increases with increasing air temperatures and CO_2 concentrations, but will be smaller in magnitude than spring carbon uptake and combined fall and winter carbon losses by year 2100. Also depicted are changes to snow, soil freeze and thaw, and vegetation dynamics that result from and contribute to changing carbon cycle seasonality. Changes to soil biogeochemical processes during fall and winter, including N mineralization and uptake, are Implied in the changes to soil freeze and thaw state. The seasons are equinox based (i.e., Spring is the period March 21 - June 20, Summer is the period June 21 - September 20, Fall is the period September 21 - December 20, and Winter is the period December 21 - March 20).

3.2 Methods

Model Forcing and Simulation Design

The model was run at a 0.25° × 0.25° grid that covers Alaska. Clay and sand fraction, pH, cation exchange capacity, and bulk density were extracted from the Unified North America Soil Map [95] and values for initial soil organic carbon content were extracted from the Northern Circumpolar Soil Carbon Database [71]. Surface air temperature, precipitation, incoming shortwave radiation, relative humidity and wind speed were taken from the North American Regional Reanalysis (NARR) [171] for the years 1979 - 2019. The first decade of the NARR record was used to spin-up the model over the years 1800 - 1978. NARR weather forcing for 2020-2100 was modified using seasonal anomalies from a CCSM4 ensemble member under the Representative Concentration Pathway 8.5 (RCP8.5). Since global carbon emissions are increasing at a rate consistent with RCP8.5, use of this high emissions scenario is common practice [90, 91, 173, 99, 124]. Historic CO_2 concentrations were used for 1800-2019, and CO_2 concentrations from RCP8.5 were used for 2020-2100. These simulations include nitrogen deposition taken from global spatially-distributed estimates [35, 171] and stand-replacing fire events, with frequency derived from the Mean Fire Return Interval (MFRI) dataset of the LANDFIRE product [136].

Model Evaluation

Here we perform further validation of the *ecosys* model. Simulated soil temperatures at 24 locations were compared to data from the Soil Climate Analysis Network (SCAN; Table 3.1) [141] and the Snow Telemetry (SNOTEL) Network [146]. Simulated NEE at 8 sites in Alaska was compared to data from Ameriflux EC towers (Table 3.2). Where available, weather observations, rather than NARR forcings, were used to force the model for each Ameriflux site.

At the regional scale, we compared *ecosys* outputs with 7 observation-based estimates of monthly NEE across Alaska: (1) an estimate of NEE by Commane et al [29] based on observed atmospheric CO_2 concentrations, remotely sensed data, and meteorological inputs; (2) NOAA's CarbonTracker (CT2019) estimates of NEE based on global measurements of atmospheric CO_2 concentration and an atmospheric transport model [75]; (3-5) three FLUXCOM estimates of NEE (FLUXCOM-RS-METEO-ERA5, FLUXCOM-RS-METEO-CRUNCEP, FLUXCOM-RS) based on machine-learning upscaling of global EC tower measurements using ERA5 weather forcing, CRUNCEP weather forcing, and no weather forcing, respectively [80]; (6) an estimate of winter CO_2 flux by Natali et al [118] based on machine learning upscaling of site chamber, soda lime, and EC measurements; and (7) an alternate machine-learning upscaling of global EC tower measurements using ERA5 weather forcing produced by Zeng et al [179].

Site Name	**Data Network**	**Latitude**	**Longitude**	**R^2**	**MBE [C]**	**RMSE [C]**
Aniak	SCAN	61.6	-159.6	0.74	0.55	3.15
Atigun Pass	SNOTEL	68.1	-149.5	0.77	-0.87	5.02
Canyon Lake	SCAN	59.4	-161.2	0.67	-0.44	3.08
Checkers Creek	SCAN	65.4	-164.7	0.42	3.88	6.32
Coldfoot	SNOTEL	67.3	-150.2	0.61	0.04	2.52
Galena	SNOTEL	64.7	-156.7	0.75	-1.29	3.22
Gobblers Knob	SNOTEL	66.8	-150.7	0.69	2.02	4.39
Granite Creek	SNOTEL	63.9	-145.4	0.73	1.43	3.07
Imnaviat Creek	SNOTEL	68.6	-149.3	0.74	-0.01	5.02
Jack Wade Jct	SNOTEL	64.2	-141.3	0.81	0.23	7.01
Kanuti Lake	SCAN	66.2	-151.8	0.87	1.31	3.00
Kenai Moose Pens	SNOTEL	60.7	-150.5	0.77	0.08	2.52
Little Chena Ridge	SNOTEL	65.1	-146.7	0.82	-0.83	3.47
Lower Mulchatna	SCAN	59.8	-157.0	0.60	1.81	4.69
Mcneil River	SNOTEL	59.1	-154.3	0.63	-2.40	3.71
Nenana	SCAN	64.7	-148.9	0.87	-1.81	7.81
Prudhoe	SNOTEL	70.3	-148.6	0.50	2.10	6.04
Spring Creek	SCAN	61.7	-149.1	0.76	-1.79	3.70
Susitna Valley	SNOTEL	62.1	-150.1	0.59	-0.66	3.82
Telaquana Lake	SNOTEL	61.0	-153.9	0.62	-0.61	3.51
Tok	SCAN	63.4	-143.0	0.75	-0.65	4.99
Tokositna Valley	SNOTEL	62.6	-150.8	0.71	-0.69	2.78
Upper Nome Creek	SNOTEL	65.4	-146.6	0.85	-0.89	5.09

Table 3.1: Soil Climate Analysis Network (SCAN) and Snow Telemetry (SNOTEL) Network sites used for comparison to *ecosys* gridded outputs of snow depth and soil temperature. R^2, Mean Bias Error (MBE), and Root Mean Square Error (RMSE) are reported for soil temperatures at 5 cm depth sampled every 10 days.

Site Name	Latitude	Longitude	IGBP	R^2	MBE [gC m^{-2}]	NSE
Barrow	71.2	-157	BSV	0.61	0.19	0.55
Bonanza Creek	64.0	-148	WET	0.70	-0.06	0.70
Council	64.9	-163.7	GRA	0.67	-0.26	0.29
EML	63.9	-149.2	OSH	0.45	-0.42	-0.89
Imnavait Creek	68.6	-149.3	WET	0.70	-0.12	0.43
Ivotuk	68.5	-155.6	WET	0.63	-0.11	0.47
Toolik	64.9	-147.8	WET	0.83	-0.01	0.81
UAF	64.9	-147.8	ENF	0.75	0.09	0.69

Table 3.2: Ameriflux sites used for comparison to *ecosys* outputs forced with site weather data. R^2, Mean Bias Error (MBE), and the Nash-Sutcliffe model efficiency coefficient are reported for monthly NEE. The International Geosphere–Biosphere Programme (IGBP) vegetation classification is also reported (BSV - Barren Sparse Vegetation; ENF - Evergreen Needleleaf Forests; GRA - Grasslands; OSH - Open Shrublands; WET - Permanent Wetlands).

Calculation of temperature and radiation limitation to net primary production (NPP)

Temperature and radiation limitations to plant productivity were quantified according to the methodology outlined in Donohue et al, 2013 [38], Keenan and Riley, 2018 [83], and Ukkola et al, 2016 [163]. All daily modeled NPP values for the years 2010-2019 and 2090-2099 were combined and grouped by air temperature (incoming shortwave radiation) into bins of 1 °C (0.3 kWh m^{-2} d^{-1}). For each bin the 99th percentile NPP was calculated. Using breakpoint regression analysis, air temperatures and radiation levels that limit NPP, and the lowest air temperatures and radiation levels that do not limit NPP, were calculated. Temperature and radiation scalars were linearly interpolated between these values.

3.3 Results and Discussion

Model evaluation and present day carbon cycle seasonality

In addition to the extensive validation of model performance in high-latitude ecosystems discussed above and listed in Table 3.1, we also compared simulations of soil temperatures and NEE to site observations and regional observation-based estimates. At the site scale, *ecosys* soil temperatures at 5 cm depth agreed very well with measurements at 8 Soil Climate Analysis Network (SCAN) and 15 Snow Telemetry (SNOTEL) Network locations that are broadly representative of Alaskan climatic zones and land cover types (mean $R^2 = 0.70 \pm$

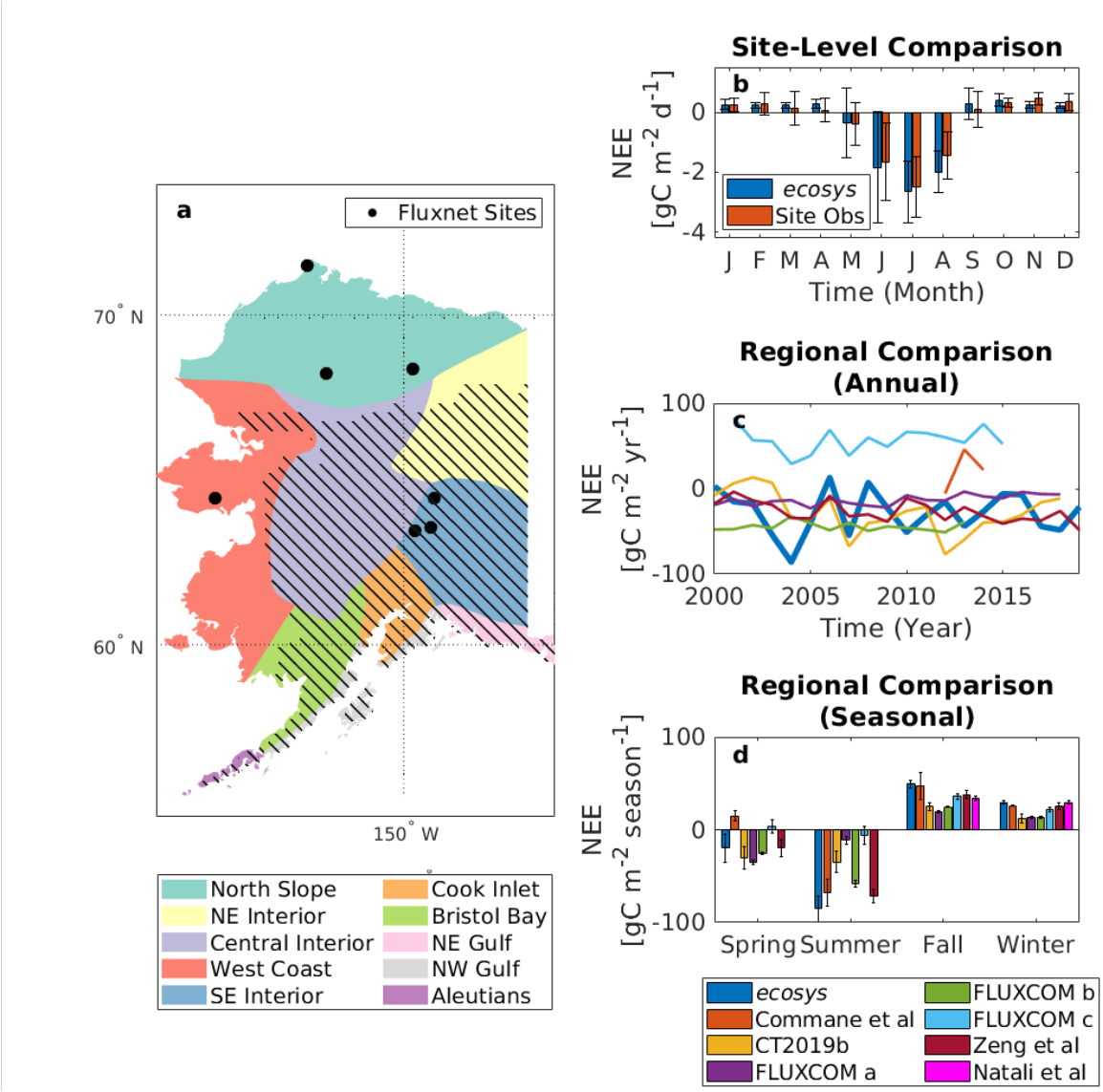

Figure 3.2: *ecosys* accurately represents NEE at site and regional scales. **a**, Map of the study region with climate zones, land cover types, and FLUXNET site locations. NOAA climate zones for Alaska are delineated by filled colors. The land cover type of the hatched regions is Koppen class 43 (boreal forest PFTs) and the land cover type of the unhatched regions is Koppen class 62 (tundra PFTs). FLUXNET site locations are marked with black filled circles. **b**, Comparison of FLUXNET measurements of NEE with *ecosys* outputs at 8 sites across Alaska. The simulations used for the FLUXNET comparison were forced with site weather data. Error bars denote the standard deviation observed and modelled across the sites. **c**,**d** Seven observation-based estimates of Alaska NEE (Commane et al, 2017 [29]; CT2019b [75]; FLUXCOM a,b,c (forced with ERA5, CRUNCEP v6, and no weather forcing, respectively) [80]; Zeng et al, 2020 [179]; Natali et al, 2019 [118]) are compared with *ecosys* predictions for Alaska annual (**c**) and seasonal (**d**) NEE. Error bars represent the standard deviation across years of observation. The seasons are equinox based.

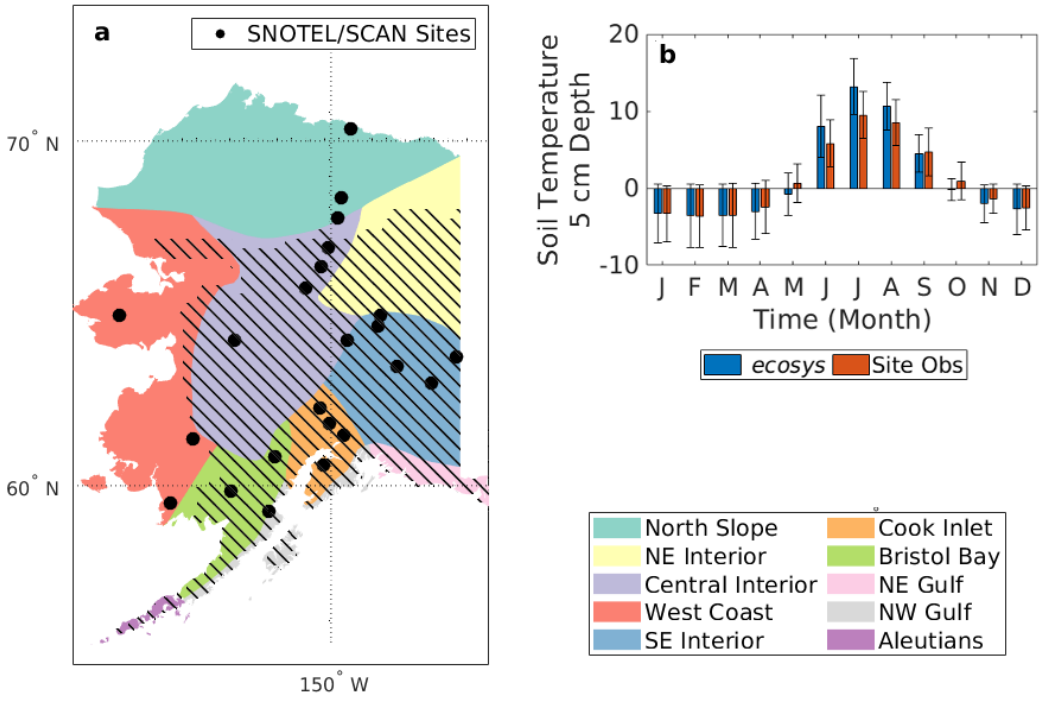

Figure 3.3: *ecosys* accurately represents soil temperatures at site scale. **a**, Map of the study region with climate zones, land cover types, and SCAN and SNOTEL site locations. NOAA climate zones for Alaska are delineated by filled colors. The land cover type of the hatched regions is Koppen class 43 (boreal forest PFTs) and the land cover type of the unhatched regions is Koppen class 62 (tundra PFTs). SCAN and SNOTEL site locations are marked with black filled circles. **b**, Comparison of SNOTEL and SCAN measurements of soil temperature at 5 cm depth with *ecosys* outputs at 23 sites across Alaska.

0.11, mean bias = 0.09 ± 1.46 °C, and RMSE = 4.22 ± 1.41 °C; Figure 3.3, Table 3.1). We also found excellent agreement with *ecosys* monthly NEE and EC tower measurements at eight Alaskan AmeriFLUX sites (mean R^2 = 0.67 ± 0.11, mean bias = -0.09 ± 0.19 gC m^{-2} d^{-1}, and Nash-Sutcliffe coefficient = 0.41 ± 0.56 gC m^{-2} d^{-1}; Figure 3.2, Table 3.2).

At the regional scale, we evaluated *ecosys* NEE against seven observation-based products [29, 75, 80, 118, 179]. These products were generated by others, either through machine learning upscaling of site measurements or through estimation of land surface flux contributions to measured atmospheric CO_2 gradients using atmospheric transport models. We

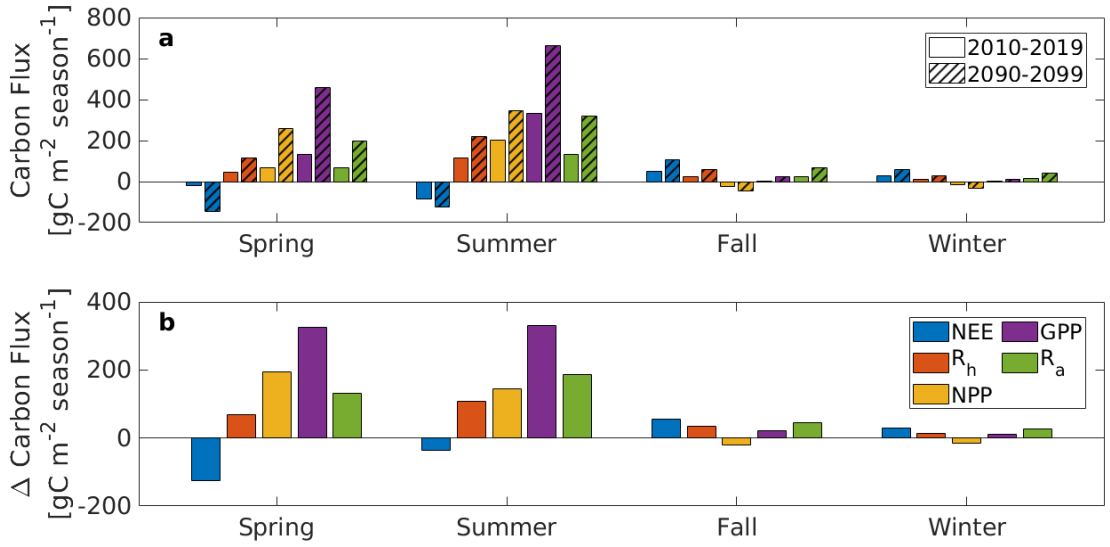

Figure 3.4: Large relative changes in Alaska spring carbon fluxes will control annual carbon budgets by 2100. a, Seasonal NEE (blue), microbial respiration (denoted as Rh, red), NEE (yellow), GPP (purple), and autotrophic respiration (denoted as Ra, green) averaged across Alaska for the years 2010-2019 (open) and 2090-2099 (hashed). **b**, Difference between 2090-2099 and 2010-2019 Alaskan seasonal carbon fluxes. The seasons are equinox based.

modeled an annual average NEE of -28 $\pm$ 25 gC m^{-2} yr^{-1} across Alaska for the years 2000-2019 (i.e., a net CO_2 sink from the atmosphere; uncertainty is expressed as standard deviation across years). The long-term mean modeled NEE is in excellent agreement with four of the six observation-based products that produced annual NEE estimates (Figure 3.2c). Previous studies have expressed concern that process-model underestimation of fall and winter high-latitude carbon fluxes [29, 118] has led to an incorrect characterization of the region as a carbon sink. However, *ecosys* predicted a 27 gC m^{-2} (50%) larger combined fall and winter CO_2 flux than the average of the observation-based products, while still predicting that Alaska is currently a net carbon sink.

Under current climate conditions, modeled Alaska NEE for years 2000-2019 is largest in magnitude during summer (Figure 3.4). Modeled summer dominance of the Alaskan carbon cycle is corroborated by the site measurements and 4 of the 6 observation-based products discussed above (Figure 3.2 c,d). The NEE seasonality of the observation-based products is broadly consistent with modeled NEE seasonality (Table 3.3). These comparisons, and those described in the Addenda, give confidence that *ecosys* is reasonably capturing the carbon cycle seasonality across our study domain.

	ecosys		Observation-based Products (mean)	
Season	**gC m^{-2} season^{-1}**	**% of summer NEE**	**gC m^{-2} season^{-1}**	**% of summer NEE**
Spring	-19.8	23	-15.3	37
Summer	-85.2	100	-41.7	100
Fall	49.3	-59	31.8	-76
Winter	29.6	-36	18.7	-45

Table 3.3: Modeled NEE seasonality is broadly consistent with NEE seasonality of observation-based products. NEE of *ecosys* outputs and the mean of the observation-based products (Commane et al (2017); CT2019b (Jacobson et al 2020); FLUXCOM a,b,c (forced with ERA5, CRUNCEP v6, and no weather forcing, respectively; Jung et al 2020); Zeng et al (2020)) is reported for each season. Also reported are normalized NEE expressed as a percentage of summer NEE for each season and product. The seasons are equinox based.

Future changes to the spring carbon cycle

To assess how carbon cycle seasonality will change across Alaska with climate warming, we ran *ecosys* through the year 2100 using a CCSM4 RCP8.5 scenario. In spring (March 21 - June 20), modeled NPP increases from 66 to 260 gC m^{-2} season^{-1} by year 2100 (positive NPP signifies positive plant growth; Figure 3.4). This large increase in spring carbon fixation is due to increases in air temperature (on average 6.7 °C by year 2100, Figure 3.5) that lead to enhanced carbon fixation rates and earlier carbon uptake, particularly since temperature sensitivity of fixation rates is larger at lower temperatures [85]. Growing season onset (defined as the first day that modeled NPP is positive) in Alaska advances by 39 days by the year 2100 (5.8 days °C^{-1}; Figure 3.6), consistent with published estimates of leafout advancement sensitivities in the northern hemisphere (Xu et al, 2019 [176]: -1 to -4.5 days °C^{-1}; Piao et al, 2015 [129]: -4.3 days °C^{-1}; Linkosalo et al, 2009 [94]: -2.2 to -7.3 days °C^{-1}). Current observations of the effect of interannual variation in spring temperatures on high-latitude leaf emergence [4, 15, 130], growing season length [27, 82, 116], and plant productivity [68, 128] confirm that high-latitude plants experience severe temperature limitations during spring.

We quantified temperature and radiation limitations to modeled plant productivity using breakpoint regression analysis of daily air temperatures, incoming SW radiation, and modeled NPP (Figure 3.7, Methods, [83]). According to this method, NPP is considered to be limited by, e.g., cold temperatures if outlying NPP values increase at warmer temperatures. Under current Alaska climate conditions, modeled NPP experiences a 61% limitation due to air temperature in the spring. By year 2100, however, spring temperature limitation to NPP will relax by more than a factor of 3 (to 19%; Figure 3.7). Since incoming shortwave radiation during these months is high, photosynthetic activity can respond positively to warmer spring temperatures. The geographically weighted regression coefficient (R^2) between spring

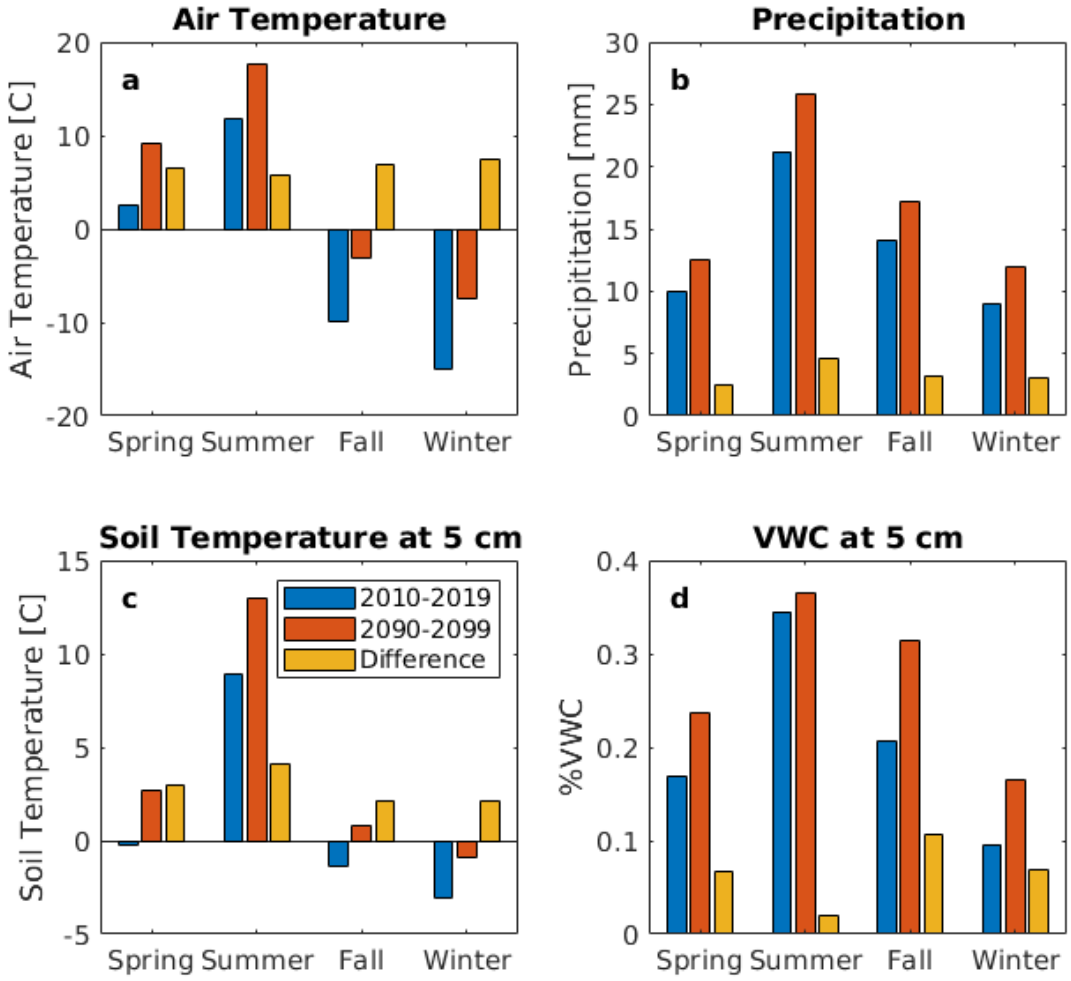

Figure 3.5: Changes in temperature and water across Alaska throughout the 21st century. Seasonal mean air temperature (**a**), precipitation (**b**), soil temperature at 5 cm (**c**), and volumetric water content (VWC) (**d**) are shown for the years 2010-2019 (blue) and 2090-2099 (red). The difference between the two decades for each variable is shown in yellow. The seasons are equinox based.

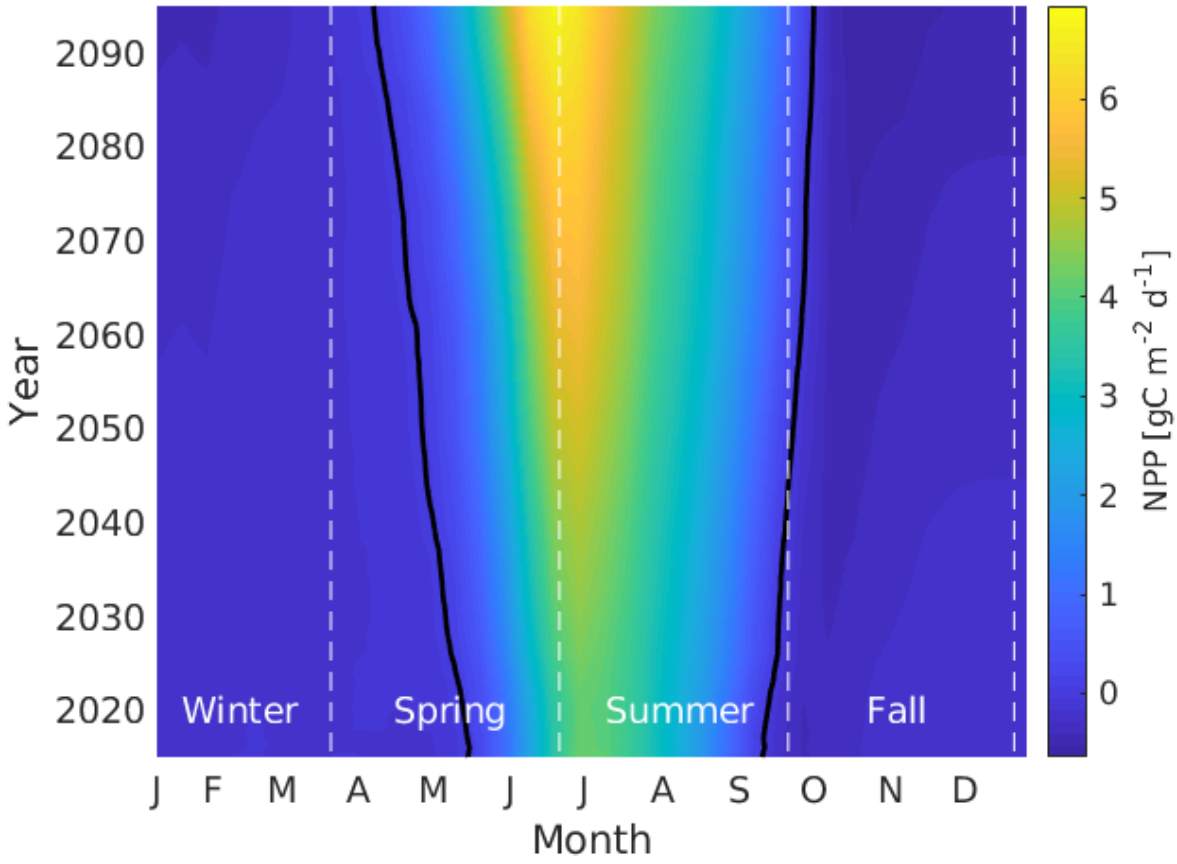

Figure 3.6: Start of the growing season in Alaska advances by 39 days throughout the 21st century. 10-year rolling mean of the annual cycle of Alaska NPP is shown for the years 2010-2100. The black lines show the dates that NPP switches between positive (carbon loss) and negative (carbon uptake) for each year, and the end of each season is shown with a white dashed line. The seasons are equinox based.

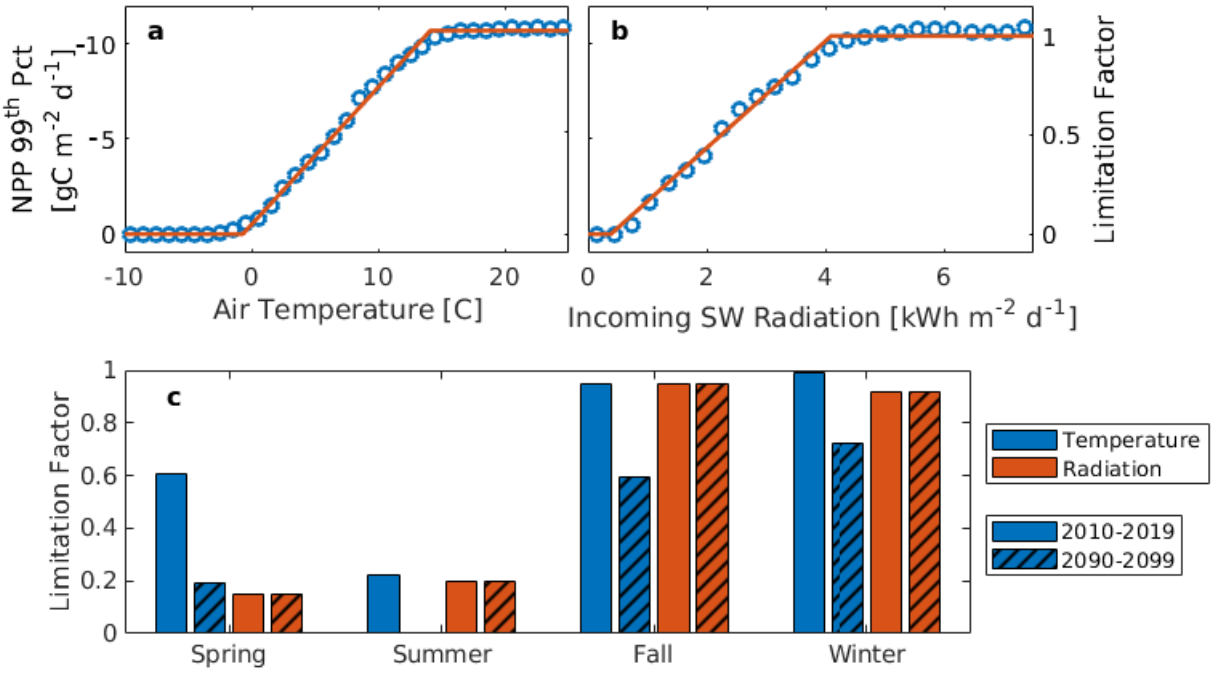

Figure 3.7: Large relative changes in Alaska spring carbon fluxes will control annual carbon budgets by 2100. **a**, **b**, Breakpoint regression analysis (red line) of the 99th percentile NPP (blue circles) is used to calculate limitations to modelled NPP by air temperature (**a**) and incoming SW radiation (**b**). **c**, Seasonal average temperature and radiation limitation factor across Alaska for the years 2010-2019 (open) and 2090-2099 (hashed). The seasons are equinox based.

temperature limitation and spring NPP remains high (0.83-0.85) throughout the century for the study domain (Figure 3.8), providing confirmation that temperature remains a primary control of spring NPP throughout the century.

Modeled spring microbial respiration (denoted as R_h in Figure 3.4) increases from 48 to 116 gC m^{-2} season^{-1} throughout the century in response to earlier snowmelt and warmer soil temperatures. Soil temperatures increase more slowly than air temperatures in the spring (Figure 3.5), so the increase in microbial respiration is much smaller than the projected increase in NPP. This difference results in a very large increase in the magnitude of spring NEE by year 2100 (-19 to -144 gC m^{-2} season^{-1}; Figure 3.4a).

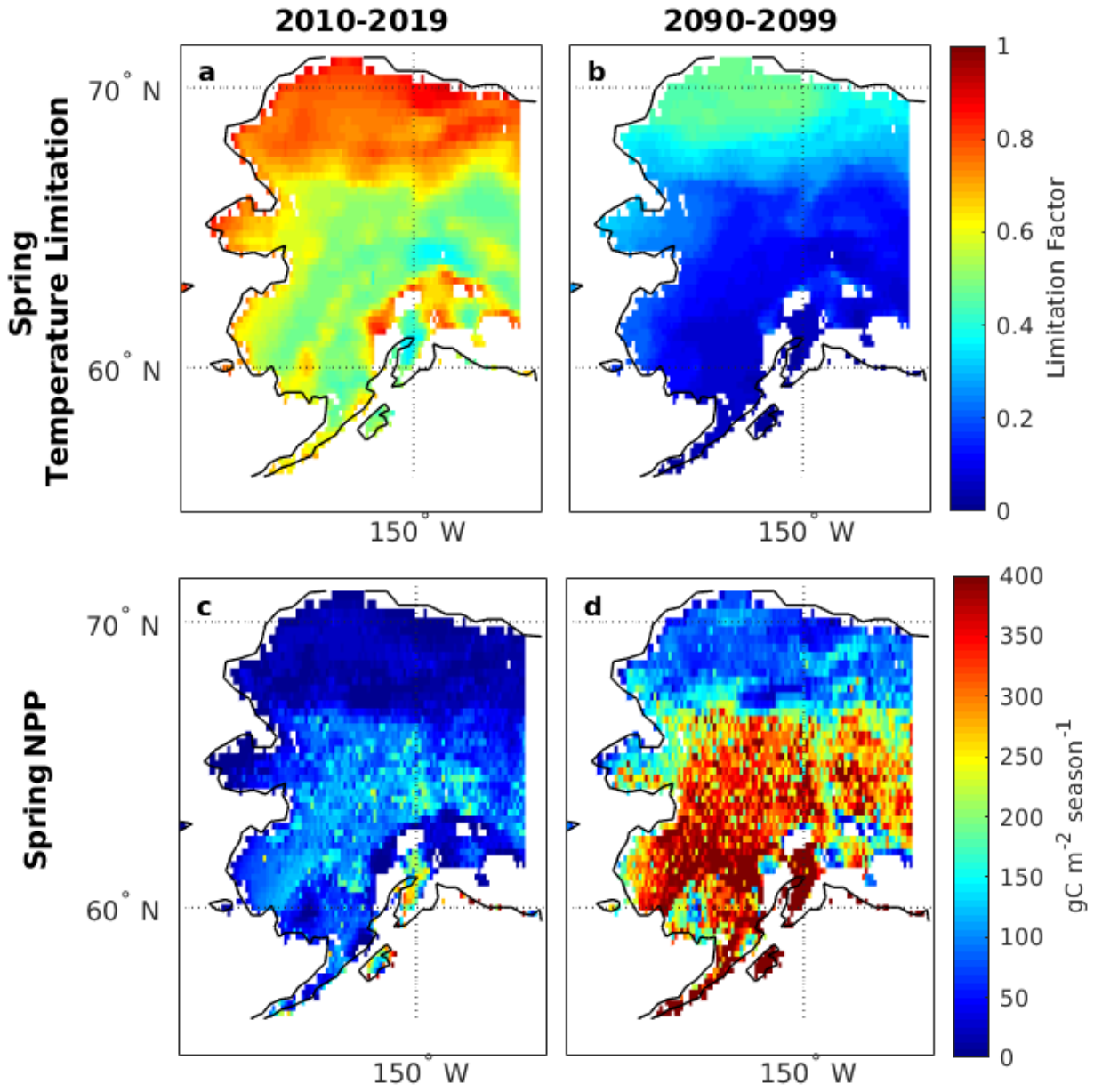

Figure 3.8: Spatial distribution of spring NPP matches spatial distribution of spring temperature limitation throughout the 21st century. Spring temperature limitation (**a**,**b**) and spring NPP (**c**,**d**) are strongly correlated (geographically weighted regression coefficient (R^2) of 0.83 for the years 2010-2019 (**a**,**c**) and 0.85 for the years 2090-2099 (**b**,**d**)). The seasons are equinox based.

Future changes to the summer carbon cycle

In summer (June 21 - September 20), modeled NPP increases from 201 to 344 gC m^{-2} $season^{-1}$ throughout the century (Figure 3.4a). Similar increases in spring and summer air temperature ($\sim$ 6 - 7 °C; Figure 3.5) lead to similar increases in spring and summer Alaska GPP by year 2100 (326 vs. 331 gC m-2; Figure 3.10). However, higher baseline air temperatures during summer lead to larger increases in autotrophic respiration (187 gC m^{-2} in summer vs. 132 gC m^{-2} in spring; denoted as R_a in Figure 3.4), resulting in smaller increases in NPP compared to spring (Figure **??**).

Some studies have hypothesized that increases in growing season water stress may lead to a reduction in summer GPP [18, 96]. Consistent with these studies, the impact of warming on summer water stress has been demonstrated using *ecosys* in an analysis of boreal forest dynamics [59]. In this study, we find that increasing summer water stress is buffered by increasing precipitation and increasing atmospheric CO_2 concentrations that reduce transpiration. The RCP8.5 climate forcing we applied here (Methods) predicts a 22% increase in summer precipitation across Alaska (Figure 3.5), consistent with studies that suggest rainfall is projected to increase with warming at high latitudes [14]. As a result, we predicted slightly wetter summer soils, almost no change in summer evapotranspiration (0.4% decrease), and a small increase ($\sim$ 16%) in summer water stress (calculated as the number of hours that the canopy water potential drops below a threshold value; Methods) across Alaska by year 2100.

Modeled summer microbial respiration increases from 114 to 221 gC m^{-2} $season^{-1}$ throughout the century (Figure 3.4). This increase is larger than that during spring because there are larger plant litter inputs and warmer and drier soils in summer than in spring. Summer net carbon uptake is projected to increase by only 36 gC m^{-2}, which is much smaller than the increase in spring net carbon uptake. By year 2100, summer net carbon uptake (123 gC m^{-2} $season^{-1}$) is less than spring net carbon uptake (144 gC m^{-2} $season^{-1}$) across Alaska (Figure 3.4,3.9).

Future changes to the fall and winter carbon cycle

In fall (September 21 - December 20) and winter (December 21 - March 20), there is only a small change in NPP throughout the century (21 gC m^{-2} $season^{-1}$ for fall and 16 gC m^{-2} $season^{-1}$ for winter). In fall, the current complete temperature limitation reduces to a partial limitation by year 2100 (Figure 3.7). However, day lengths during fall in Alaska are very short, and there is not enough sunlight to drive photosynthesis. Since incoming shortwave radiation seasonality is driven primarily by earth-sun geometry (i.e., not climate change), the extreme radiation limitation to fall and winter NPP is not expected to change significantly over the coming century [70]. In fall, temperature and radiation are each currently strongly limiting, but by year 2100 radiation will become the dominant limiting factor to fall carbon fixation. This prediction is consistent with observed large-scale increases in radiation limitation across northern latitudes [181].

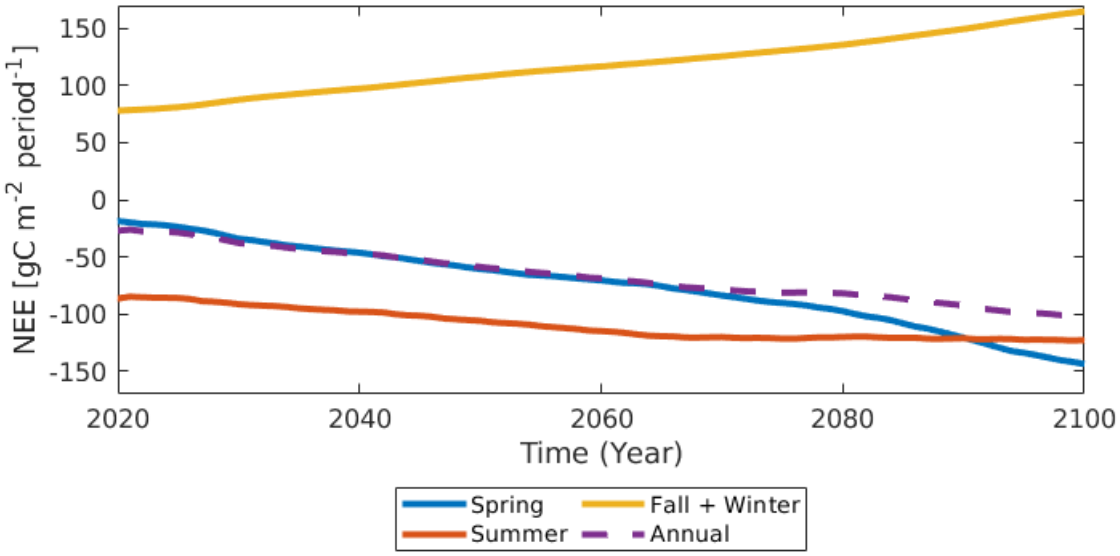

Figure 3.9: Spring net carbon uptake becomes larger than summer uptake by year 2100. 10-year rolling mean of Alaska spring (blue), summer (red), combined fall and winter (yellow), and annual (purple) NEE for the years 2020-2100. The seasons are equinox based.

By year 2100, average fall soil temperatures increase from -1.3 ℃ to 0.8 ℃, average winter soil temperatures increase from -3.0 ℃ to -0.9 ℃, and the first frost (defined as the date when surface soil temperature first drops below -0.2 ℃) is delayed by one month on average. Modeled microbial respiration by year 2100 increases in response to warming soil temperatures from 25 to 61 gC m^{-2} season^{-1} in fall, and from 15 to 31 gC m^{-2} season^{-1} in winter. Net carbon loss during fall and winter is projected to shift from 76 gC m^{-2} season^{-1} (88% of summer net carbon uptake) to 163 gC m^{-2} season^{-1} (133% of summer net carbon uptake) over the course of the century (Figures 3.4,3.9). Adding in the large increase in spring net carbon uptake, modeled annual Alaska NEE will increase in magnitude from -30 gC m^{-2} yr^{-1} in the current decade to -108 gC m^{-2} yr^{-1} by year 2100 (Figure 3.9).

Fall and winter nitrogen cycle is linked to the spring carbon cycle

Whereas most large-scale land models link plant nutrient acquisition with instantaneous photosynthetic demand, *ecosys* allows plants to use nonstructural carbon reserves to uptake and store nutrients whenever they are available [134]. In the model, rates of mineralization and nitrogen fixation (symbiotic and non-symbiotic) control soil nitrogen availability and depend on soil temperature and liquid water availability. During fall and winter, modeled

plant nitrogen uptake varies with the number of days that soil temperatures at 5 cm depth remain above freezing ($R^2 = 0.60$). Throughout the 21st century, the number of days above freezing increases from 21 days to 60 days, synchronous with an increase in fall and winter plant nitrogen uptake from 0.26 gN m^{-2} to 0.69 gN m^{-2} (Figure 3.10).

Nutrient acquisition during the fall and winter has been shown to strongly influence year-round vegetation growth and competitive dynamics in northern ecosystems [26, 89, 98]. By the end of the century, 22.5% of modeled plant nitrogen acquisition occurs during fall and winter, and it is likely that the large increase in spring productivity discussed above would not be possible without this source of nitrogen. Indeed, we find that modeled increases in spring NPP throughout the century are more strongly correlated with increases in fall and winter plant nitrogen uptake ($R^2 = 0.69$) than with increases in spring plant nitrogen uptake ($R^2 = 0.47$; Figure 3.6). This result highlights the importance of accounting for fall and winter plant nutrient uptake in predictions of seasonal and annual high-latitude ecosystem response to climate change.

Methane and high-latitude carbon balance

Methane is a potent greenhouse gas, with a sustained global warming potential ($SGWP_{100}$) 16.4 times larger than CO_2 over a 100 year time span [120]. At high-latitudes, the highest rates of methane fluxes to the atmosphere are found in wetland systems [111], which cover approximately 30% of the land surface area of Alaska [172]. While *ecosys* simulates methane production and consumption, the simulations presented in this chapter are only of upland ecosystems - not wetlands. However, atmospheric transport models coupled with tower measurements of methane concentrations [81] and airborne measurements of methane fluxes [25] estimate that Alaska is a net source of 1.5 - 2.5 gC (CH^4) m^{-2} yr^{-1}. The $SGWP_{100}$ of these methane emissions is equivalent to a flux of 25 - 41 gC (CO^2) m^{-2} yr$_{-1}$, which offsets the 28 $\pm$ 25 gC m^{-2} yr^{-1} net carbon uptake of Alaskan upland ecosystems estimated by *ecosys*.

Future rates of high-latitude methane production are highly uncertain, with some models predicting little increase in methane production [166] and others predicting large increases [147]. Uncertainty in future changes to regional precipitation and subsurface hydrology (and therefore wetland extent) is one of the main sources of uncertainty in estimates of future high-latitude methane emissions [62].

Caveats and Uncertainties

Some processes important to ecosystem carbon balance and export, such as topography, landscape-scale hydrology, thermokarst, and other geomorphological dynamics, are not represented in these model runs. Additionally, since boreal forest PFT species are not initialized in regions of present-day tundra, boreal treeline advance, which has been observed across the high-latitudes [67], does not occur in these simulations. However, trends in the seasonality of terrestrial ecosystem carbon exchange identified here are expected to be robust since they are attributed primarily to seasonal light availability driven by earth-sun geometry

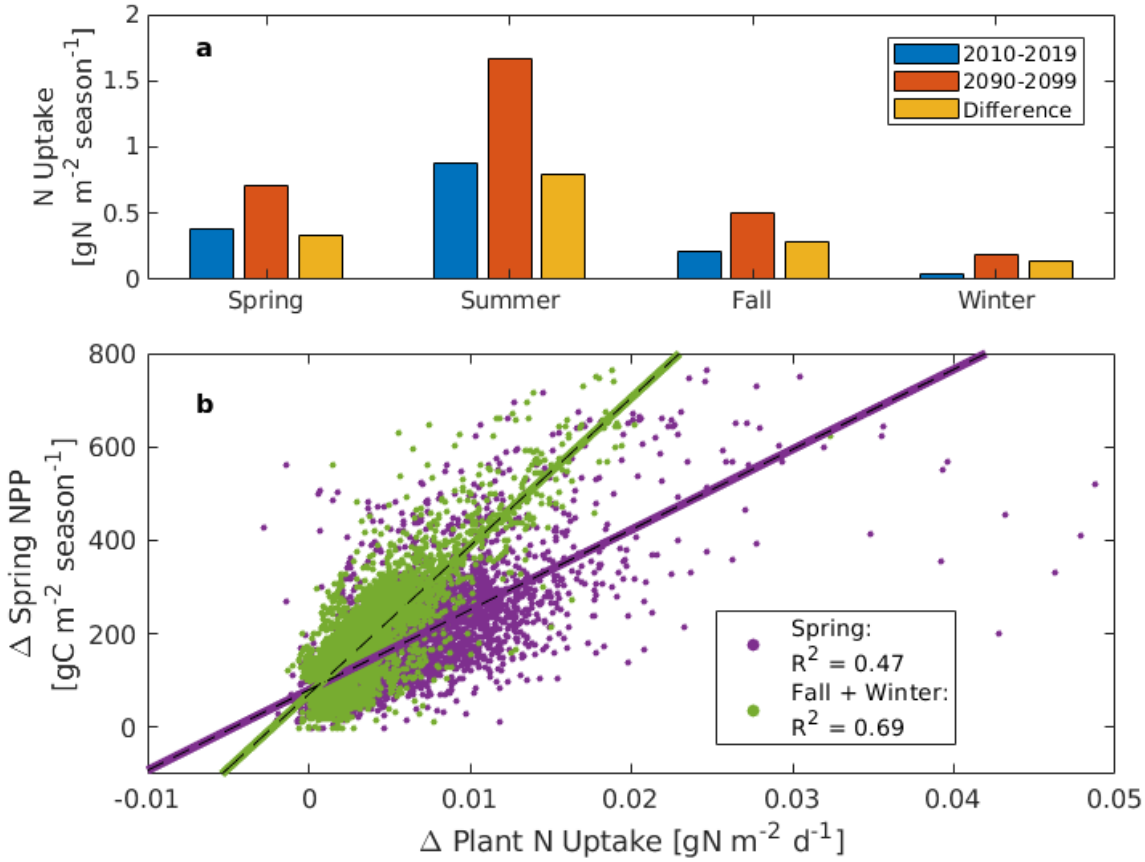

Figure 3.10: Increasing fall and winter plant N uptake drives increasing spring NPP. a, seasonal plant N uptake in each grid cell is shown for the years 2010-2019 (blue) and 2090-2099 (red). The difference between the two decades for each variable is shown in yellow. **b**, Differences in spring NPP between 2090-2099 and 2010-2019 are plotted against differences in mean daily plant N uptake during spring (purple) and fall and winter (green) for the same period. The seasons are equinox based.

and large-scale shifts in seasonal temperature driven by climate change. As is the case for all model analyses of ecosystem dynamics, there is uncertainty associated with the gridded climate data and soil information we used to force *ecosys* [102, 169]. Biases in temperature forcing data would affect the rates of processes (e.g., maximum fixation rates, electron transport rates) that drive modeled plant productivity and microbial respiration. While this uncertainty has an impact on comparisons between *ecosys* and observation-based products, it does not affect our conclusions, as we show using a sensitivity analysis (see Addenda).

3.4 Conclusions

We show that 21st century climate warming will shift carbon cycle seasonality across Alaska. Spring carbon sink strength will become larger than summer carbon sink strength by year 2100 due to relaxation of temperature limitations to plant productivity and nutrient availability. This result represents a striking, and to our knowledge, previously unreported shift in the timing of high-latitude net carbon uptake. Severe radiation limitation to NPP in fall and winter is not projected to change, so increased temperatures during these months will not benefit plant carbon uptake. Instead, warming soils and increased plant inputs will lead to higher rates of autotrophic and microbial respiration, and net carbon loss during the fall and winter will become larger than net carbon uptake during the summer by year 2100. Further investigation is needed to ascertain the impacts of shifting carbon cycle seasonality, and associated changes in energy and water fluxes, on climate.

Our results address the conflict between modeled and observation-based assessments of high-latitude ecosystem carbon balance. Our model predictions of large and increasing fall and winter carbon losses are consistent with observation-based estimates produced by Natali et al [118] and Commane et al [29], unlike most process models referenced in those studies. However, our results also agree with the process model consensus that high-latitudes will remain a carbon sink throughout the 21st century. This result is attributable in part to increased nitrogen mineralization and plant nutrient uptake coincident with fall and winter carbon losses. Nevertheless, data used to build observation-based products and to parameterize and validate process models is very sparse at high-latitudes. Increased spatial and temporal coverage of measured ecosystem carbon fluxes would be very helpful to verify the trends predicted here, and to further close the gap between mechanistically modeled and observation-based estimates of seasonal carbon fluxes.

3.5 Addenda

June and July mismatch between model and observation-based products

There is a mismatch between *ecosys* and the observation-based products during June and July. During these months, the biases relative to the ensemble regional means (defined as *ecosys* minus the observational product) are -1.1 and -0.9 gC m^{-2} d_{-1}, respectively (Figure 3.11). This disagreement is likely due to biases in the NARR climate reanalysis we used to force *ecosys*, particularly since NARR is known to significantly overestimate incoming shortwave radiation and precipitation at high-latitudes [171]. For example, we found that the model NEE biases in June and July disappear when the model is forced with measured site weather data (Figure 3.12). However, there are also known uncertainties associated with each of the observation-based products that are challenging to quantify. Variation in the parameters, model structure, and boundary conditions used in atmospheric transport models can have large impacts on estimated ground surface fluxes [142, 28] and site measurements of carbon fluxes needed for machine learning model training are very sparse in northern high-latitude ecosystems [80].

To evaluate the potential uncertainty to our conclusions resulting from these biases, we filtered out grid cells that had a bias larger than 25% relative to the mean of the observation-based products during June and July. We found that the remaining grid cells had a low bias in each month and that trends in carbon flux seasonality over the coming century for this subset of grid cells are the same as for the full set of grid cells (Figure 3.13).

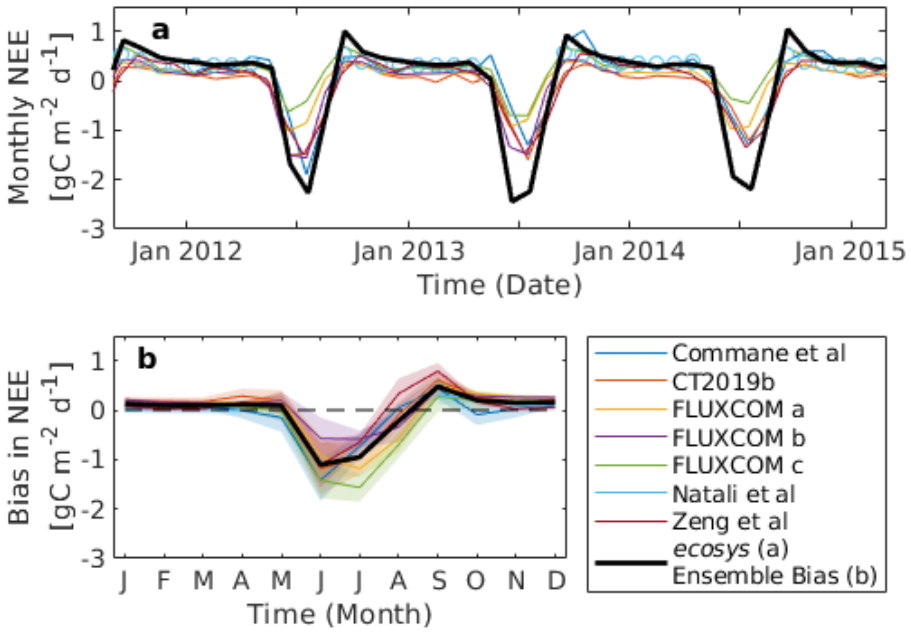

Figure 3.11: There is a bias of *ecosys* NEE relative to observation-based products during the months of June and July. **a**, Comparison of *ecosys* outputs of NEE with 7 observation-based products (Commane et al, 2017 [29]; CT2019b [75]; FLUXCOM a,b,c (forced with ERA5, CRUNCEP v6, and no weather forcing, respectively) [80]; Zeng et al, 2020 [179]; Natali et al, 2019 [118]) is shown for the years 2012-2015. **b**, Monthly bias of *ecosys* relative to each observation-based product for the years 2000-2019 where data is available. The bias is defined here as *ecosys* minus the observation-based product, and the mean ensemble bias is shown in black.

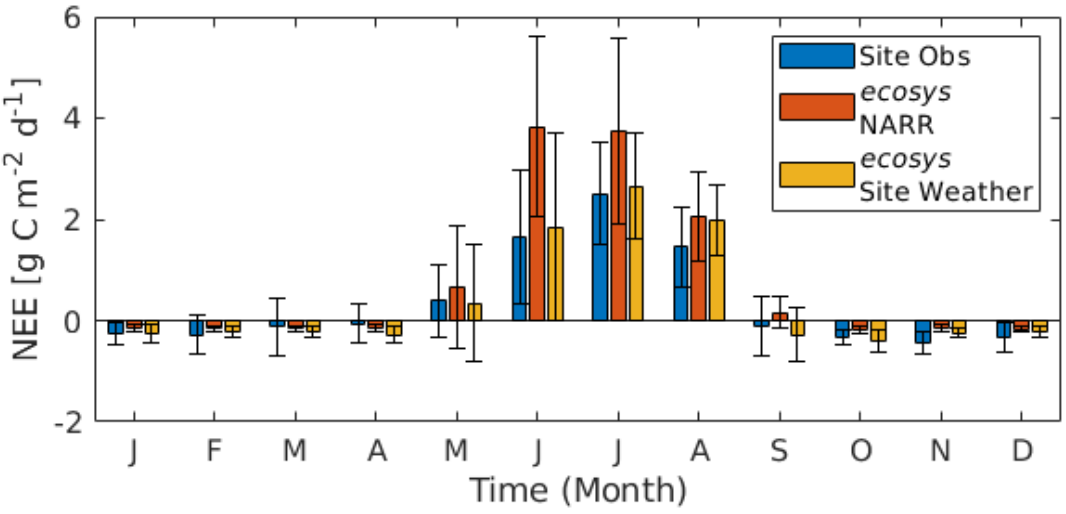

Figure 3.12: June and July bias in NEE disappears when site weather is used to force *ecosys* at FLUXNET sites. Comparison of FLUXNET measurements of NEE at 8 sites across Alaska (blue) with *ecosys* outputs when forced with NARR reanalysis product (red) and weather data collected from the site (yellow). Error bars denote the standard deviation observed and modelled across the sites.

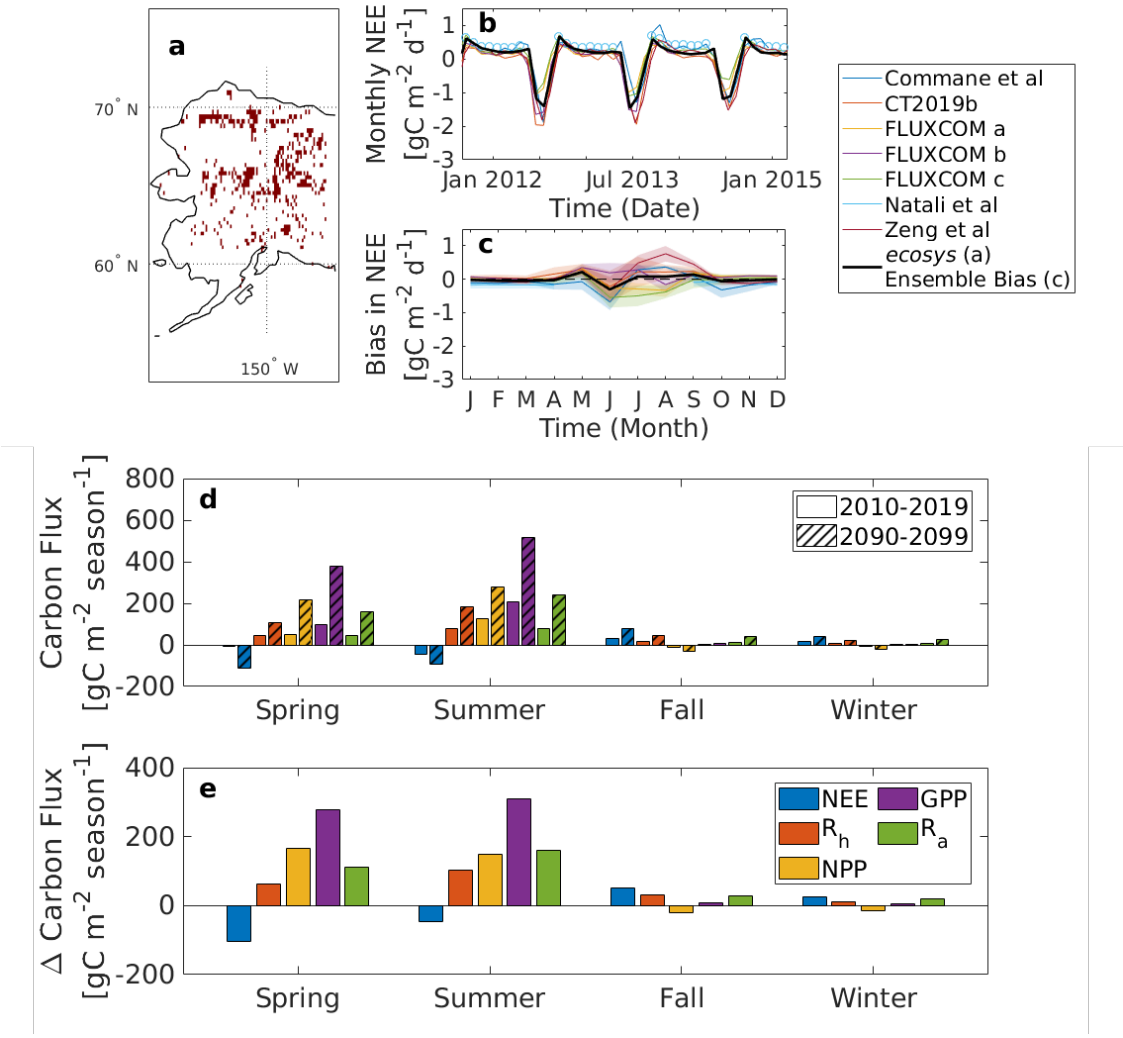

Figure 3.13: Filtering grid cells by regional product bias in June and July does not affect trends in seasonal carbon fluxes across Alaska throughout the 21st century. A mask was created by selecting grid cells in which the mean of the observation-based products during the months of June and July is within 25% of the *ecosys* prediction for those months (**a**). **b**, Observation-based estimates of NEE (Commane et al, 2017 [29]; CT2019b [75]; FLUXCOM a,b,c (forced with ERA5, CRUNCEP v6, and no weather forcing, respectively) [80]; Zeng et al, 2020 [179]; Natali et al, 2019 [118]) are compared with *ecosys* outputs for the masked monthly NEE for the years 2012-2015. **c**, Bias in monthly NEE for the masked region is shown for each product. **d**, Seasonal NEE (blue), microbial respiration (denoted as Rh, red), NEE (yellow), GPP (purple), and autotrophic respiration (denoted as R_a, green) averaged across the masked grid cells for the years 2010-2019 (open) and 2090-2099 (hashed). **e**, Difference between 2090-2099 and 2010-2019 for the masked seasonal carbon fluxes. The seasons are equinox based.

Chapter 4

Drivers of variability in ecosystem processes across a sub-arctic watershed

Complexity and feedback loops create strong heterogeneity in high-latitude ecosystems. Ecosystem characteristics like vegetation cover, soil temperatures, and carbon fluxes vary strongly across scales too small to be driven by the large-scale controls discussed in the previous chapter. In this chapter, the causes and implications of this fine-scale heterogeneity are explored. A sensitivity analysis of the *ecosys* model is used to identify and rank the drivers of the variability in ecosystem processes observed in a watershed underlain by discontinuous permafrost. This sensitivity analysis is used as a case study to show that missing representation of this heterogeneity can introduce bias into predictions of the high-latitude carbon budget produced by earth system models.

4.1 Introduction

Spatial heterogeneity in permafrost ecosystems drives uncertainty in predictions of carbon cycle responses to climate change [88, 161]. The horizontal grid spacings of CMIP5 and CMIP6 models used by the IPCC to forecast the global response to climate change (100-300 km) [152] are much coarser than typical scales of landscape heterogeneity in permafrost ecosystems. In these systems, snow depth, soil properties, and vegetation composition can vary over horizontal distances of 1-10 m [60, 162].

Landscape heterogeneity is particularly pronounced in discontinuous permafrost environments, where perennially frozen (permafrost) and perennially unfrozen (talik) soils coexist at local scales (O(m)) [162, 183]. Such strong heterogeneity in subsurface physical conditions is created by complex interactions and feedbacks between climate, hydrology, soil properties, and vegetation [79]. Local variation in snow depth is a primary driver of soil temperature heterogeneity across the arctic [76, 123, 156]. Feedback loops are important in these systems,

as some controls on high-latitude soil temperatures, such as soil organic matter content [182] and vegetation cover [34, 76, 125], respond to heterogeneity in soil temperatures via changes in microbial activity [168] and vegetation dynamics [11, 76, 108]. Soil thermal state also has a strong impact on nitrogen availability [44, 84] and carbon fluxes [12, 121] at high latitudes.

While many relationships between environmental factors and spatial variability in soil temperature, vegetation dynamics, and carbon fluxes have been identified, system complexity complicates field and modeling efforts to characterize the relative importance of each driver in producing local heterogeneity [7]. Further, these environmental factors operate in the context of the local climate, and quantification of the strength of each driver relative to variability in regional climate controls, while important, is an added challenge. Landscape heterogeneity is a characteristic feature of ecosystems across the globe and efforts have been made to characterize and represent the impacts of heterogeneity in vegetation cover [21], hillslope position [108], and microtopography [60, 61] on soil temperatures, vegetation, and carbon fluxes. Nevertheless, the level of detail in representation of sub-grid heterogeneity needed to accurately represent key system processes in TEMs remains unclear. In particular, more work is needed to understand how missing model representation of landscape heterogeneity (e.g., snow depths, landscape position, soil thermal and hydrologic condition, and vegetation cover) in a TEM grid-cell impacts representation of carbon cycle dynamics in discontinuous permafrost ecosystems.

In this study, we explore how variability in soil properties, landscape position, and weather forcing affect variability in soil thermal regimes, vegetation dynamics, and carbon cycling as simulated in a one-dimensional TEM. We perform a global sensitivity analysis (GSA) using *ecosys*, varying soil properties, boundary conditions, and weather forcings over ranges that represent the variability found in a watershed on the Seward Peninsula in Alaska. Because of the computational demands, process richness, and nonlinearity of this model, we use the Morris one-at-a-time method, a difference-based GSA with computational costs that scale linearly with the number of factors explored [167, 114]. We first show that the simulations generated in the GSA cover the range of soil temperatures, water contents, and surface CO_2 fluxes observed within the watershed. Then, we use the GSA results to identify and rank the drivers of variation in soil temperatures, permafrost distribution, and vegetation composition. Finally, we explain how this variation impacts ecosystem productivity and explore the prediction uncertainty associated with ignoring observed landscape heterogeneity.

4.2 Methods

Morris Sensitivity Analysis

The Morris Method is a one-factor-at-a-time sensitivity analysis designed to cover large factor spaces efficiently [167, 114]. The Morris Method is a GSA, meaning that it is robust to non-linearity and interaction effects among factors. In this method, each factor is allowed to vary within a prescribed range that defines the factor space to be explored. The factor

space is not continuous, however, since each factor can only take p discrete values that are equally distributed throughout the prescribed range. Trajectories or paths of runs are generated, where each of the k factors is changed by a fixed increment Δ from a randomly selected initial value, where Δ represents $p/(2(p\text{-}1))$ times the factor range. The order in which the factors change is also randomly generated, and the process is repeated r times (Morris, 1991). An approach pioneered by Campolongo et al (2007) [22] and improved by Ruano et al (2012) [139] to generate sets of trajectories that optimally cover the factor space is used in this work.

In a Morris sensitivity analysis, the metric used to characterize the influence of a factor x on an output y is called the elementary effect (EE). The EE of x on y is defined as the difference in the output y between two neighboring runs (where only one factor, x, has been changed) divided by Δ. Since there are r trajectories, the EE for each x and y can be calculated r times. Typically, the mean EE, the mean of the absolute value of the EE, and the standard deviation of the EE are calculated. These metrics give information on the relative importance of each factor on each output, the sign of the effect, and the presence or absence of non-linearities or interaction effects. These metrics can be combined to give a rule-of-thumb threshold of factor significance. The impact of a factor on a model output is considered to be significant if the mean EE or mean absolute EE are larger than two times standard error of the EE, as in Morris (1991) [114].

Site Data and Meteorological Forcing

This study is undertaken as part of the Next-Generation Ecosystem Experiment (NGEE-Arctic project). The NGEE-Arctic project aims at improving Earth System models through interdisciplinary and coordinated investigation of arctic terrestrial ecosystems. In this work, we focus on a watershed within the Seward Peninsula that has been the subject of extensive investigation by the NGEE Arctic project [93, 162].

The studied watershed is located about 40 km northwest of Nome along Teller road and occupies an area of approximately 2.3 km^2. The topography of the watershed is characterized by a 130 m elevation gradient that leads to the emergence of heterogeneous properties. Solifluction lobes, drainage paths, and other meter-scale microtopographic features generated by variable permafrost degradation are found throughout the watershed. At some locations, the permafrost table is close to the surface, at 0.5 m or shallower, and at others there is a talik below the active layer and the permafrost table is deep or absent. Across the watershed, bedrock depth likely varies from meters to tens of meters, O-horizon thickness varies from a few centimeters to tens of centimeters, and mixtures of low-lying tundra vegetation (dwarf shrubs, bryophytes, graminoids, and sedges) are interspersed with patches of deciduous willow shrubs (Salix spp) reaching heights of 3m.

Nine intensive monitoring stations are distributed around the watershed, each with soil temperature at 2, 25, 50, 100, and 150 cm depths and volumetric water content (VWC) sensors at 10, 25, and 50 cm depths [138]. At 1.5 m depth, measured peak soil temperatures at these sites vary by more than 5 °C (from -0.2 °C to 5.7 °C). While some sites never rise

above 0 °C at 1.5 m depth for the years 2016-2018, others never freeze at depths much closer to the surface (Figure 4.3). In 2017, 2018, and 2019, snowpack thickness was measured across the watershed in the spring before the onset of snowmelt. In 2019, a high snow year, snow depths measured across the watershed on April 1 (near peak snowpack) ranged from 14 cm to 214 cm. At six sites characterized by distinct vegetation cover and soil saturation in a small subset of the studied watershed, we deployed Eosense FD chambers to measure soil CO_2 fluxes throughout the 2019 growing season and into the fall. At these sites, peak daily mean CO_2 flux ranged from 1 µmol m^{-2} s^{-1} to greater than 5 µmol m^{-2} s^{-1} and the date that soil CO_2 flux dropped below 0.5 µmol m^{-2} s^{-1} ranged from early August to mid November.

The GSA *ecosys* simulations were run from 1836 to 2019 at hourly temporal resolution. For the years 1836-1979, values for air temperature at 2 m, incoming shortwave radiation, precipitation, wind speed at 10 m, and relative humidity at 2 m were taken from the NOAA-CIRES-DOE 20th Century Reanalysis V3 product [149]. For the years 1980-2019, values for air temperature at 2 m, wind speed at 10 m, and relative humidity at 2 m were taken from the North American Regional Reanalysis (NARR) [171], and values for incoming shortwave radiation and precipitation were taken from the Modern-Era Retrospective Analysis for Research and Applications, version 2 (MERRA-2) [49]. Data from two weather stations located at the top and near the bottom of the watershed [20] for the years 2017-2019 were used to bias correct these weather products.

Sensitivity Analysis Design

Here, we run a Morris sensitivity analysis of the *ecosys* model to changes in 24 factors related to soil properties, boundary conditions, and weather forcings. The range chosen for each factor is meant to capture the possible range of values that might be observed within a 100 km radius of the studied watershed. Some of these ranges are chosen to create differences in our 1D simulations consistent with differences expected from landscape position in a fully 3D model (e.g., snow interactions with microtopography and vegetation, water table interactions with hillslope position, radiation interactions with aspect). Each factor in the analysis can take 6 discrete and evenly distributed values within the prescribed range (Table 4.1).

The simulated soil column is 40 m thick with 20 layers that are grouped into three types (O-horizon, A/B horizon, bedrock). The thickness and other properties of each soil type are modified independently. The O-horizon has high organic matter content (50-100% by weight) and a variable thickness of 0 - 40 cm. Water retention and drainage in organic soils are highly variable. Hemic and sapric peat soils have high water retention, but fibric peat soils, which have large macropore fractions, are typically well drained [36]. We represent this in the GSA by varying the macroporosity of the O-horizon from 50 - 100% by volume. The A/B horizon is primarily mineral soil that extends from the bottom of the O-horizon to the top of the bedrock. The organic matter content of this layer ranges from 0.5 - 20% by weight. Sand content of this layer can range from 0 - 100% of the non-organic soil by weight, and clay content can range from 0 - 20% by weight, and the remaining mineral soil is silt. The impacts of gravelly soil on thermal properties and drainage are represented by

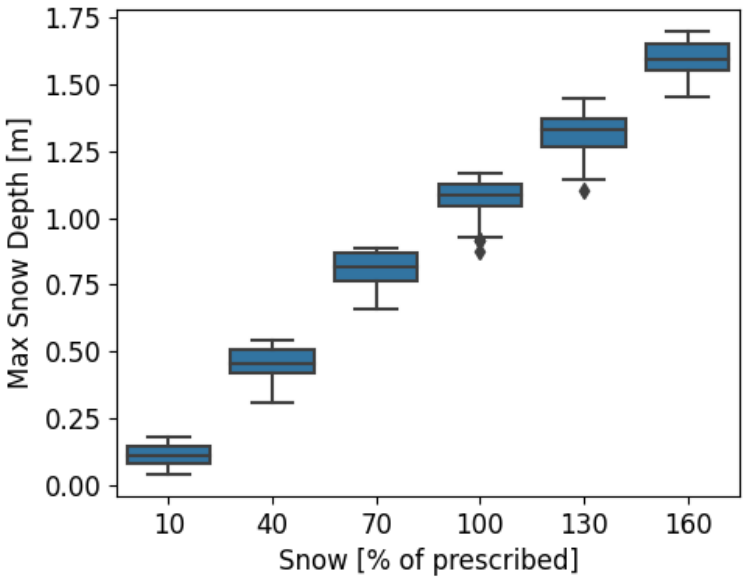

Figure 4.1: Maximum snow depth responds linearly to changes in prescribed snow precipitation. Mean maximum annual snow depth for the years 2015-2019 is plotted against the percent of prescribed snow precipitation. The R^2 coefficient for these two variables is 0.99.

the A/B-horizon rock and macroporosity, both of which can vary from 0 - 15% by volume. The bedrock is solid rock with fractures represented by variation in bedrock macroporosity from 0-15% by volume. In the GSA, depth to bedrock can take values of 0.8, 1.5, 2.5, 5, 15, or greater than 40 m. C:N, C:P, pH, and ion concentrations are modified throughout the soil profile. Changes in the lateral hydrological boundary conditions and the mean annual temperature of the bottom of the modeled soil column affect heat and water flux boundary conditions and thereby soil moisture and temperature.

In the GSA, we also modify site weather conditions. These modifiers remain constant throughout the entire 183 year simulation. Snow precipitation is varied from 10% to 160% of the prescribed value in order to represent the large variability in snow depths across the watershed created by wind redistribution of snow to microtopographic lows and areas of tall shrubs. Modeled maximum annual snow depths respond linearly to these changes in snow precipitation (Figure 4.1), so for simplicity we assume snow precipitation is a direct proxy for snow depth in the analysis below. Air temperature, rain, wind, and incoming shortwave radiation are modified to reflect measurement uncertainty and watershed- to regional-scale variations. For example, we vary mean annual air temperature over a 2 °C range, which corresponds to a 140 km north-south distance at our site (NARR) [171].

We calculate mean EEs and mean absolute EEs for mean soil temperatures (at the

Name	Description	Units	Min	Max
OH thickness	O-horizon thickness	m	0	0.40
BR depth	Soil layer of top of bedrock	-	10	20
OH MP	Macroporosity of the O-horizon	%	0	50
A/B MP	Macroporosity of the A/B horizon	%	0	15
BR MP	Macroporosity of the bedrock	%	0	15
A/BH rock	A/B-horizon rock content	%	0	15
OH OM	O-horizon organic matter content	gC kg^{-1}	500	1000
A/BH OM	A/B-horizon organic matter content	gC kg^{-1}	5	200
A/BH Sand	A/B-horizon sand content	g kg^{-1}	0	1000
A/BH Clay	A/B-horizon clay content	g kg^{-1}	0	200
pH	pH of soil profile	-	4.5	8
C:N	C:N of soil profile	-	10	30
C:P	C:P of soil profile	-	50	300
Minerals	Exponential modifier of soil concentration of Ca, Mg, Na, Sulfate, and Cl	-	-3	2
Sulfate	Exponential modifier of soil concentration of sulfate	-	-3	3
Initial Ice	Initial soil ice content	% of porosity	0	95
Snow	Percent of prescribed snow precipitation	%	10	160
Rain	Percent of prescribed rain precipitation	%	66	133
Air T	Degrees added to prescribed air temperature	℃	-1	1
Wind	Percent of prescribed wind	%	50	200
SW In	Percent of prescribed Incoming SW radiation	%	75	125
Slope	Slope	-	0	25
MAT	Mean annual temperature at lower boundary	℃	-1	1
WT	Depth to external water table, sets lateral hydrological boundary conditions	m	0.2	3.2

Table 4.1: Factor description for the Morris GSA. The name, description, units, and range of values is given for each factor that is varied in the GSA. Since ion concentrations can vary by many orders of magnitudes in arctic soils (Wu et al., 2018), Ca is varied from 10-3 - 102 mg/L, Mg is varied from 10-2 - 103 mg/L, Na is varied from 10-1 - 104 mg/L, K is varied from 10-3 - 102 mg/L, SOx is varied from 10-3 - 103 mg/L, and Cl is varied from 10-1 - 104 mg/L.

surface, 90 cm, and 275 cm), carbon fluxes (R_h, NPP, and NEE), and PFT mean annual NPP (shrub, moss, and sedge). To aid analysis of interactions between soil thermal regimes, vegetation dynamics, and carbon cycling, we classify each GSA simulation using mean annual soil temperatures at 90 cm (90 cm MAT) for the years 2015-2019. In this classification, Talik runs have minimum annual temperatures greater than -0.1 °C at 90 cm, shallow permafrost runs (shallow PF table) have maximum annual temperatures less than -0.1 °C at 90 cm, and all other runs are classified as deep active layer runs (deep AL). Runs classified as deep AL may or may not be underlain by permafrost. The runs for each class are located in a different quadrant in the second row of Figure 4.2. We chose to perform this classification at 90 cm depth to balance relevance of biological processes and permafrost dynamics. At shallower depths, MATs exhibit large interannual variability and there are few runs with permafrost, whereas at deeper depths, soil thermal processes become largely disconnected with biological activity. MAT at a similar depth has been used in previous studies in the region to connect permafrost and vegetation dynamics [21].

4.3 Results and Discussion

GSA outputs reflect the spatial variability observed in the watershed

The system dynamics are spatially heterogeneous, depending on the different soil physical conditions, snow depths, and vegetation cover that can be found across the watershed. This spatial variability is well captured by the outputs of the GSA. In the GSA, the 10th (90th) percentile for peak soil temperatures at 1.5 m depth is -0.5 °C (10 °C). Throughout the years 2015-2019, soil temperatures at 30 cm never dropped below -0.1 °C in 80 simulations and soil temperatures at 90 cm never rose above -0.1 °C in 54 simulations. The 10th (90th) percentile snow depth on April 1, 2019 is 12 cm (196 cm), and the 10th (90th) percentile peak daily mean soil CO_2 flux for the year 2019 is 1.6 µmol m^{-2} s^{-1} (6.2 µmol m^{-2} s^{-1}). In general, the GSA outputs cover the range of soil temperatures, water contents, snow depth, and soil CO_2 fluxes observed in the studied watershed (Section 2.4; Figure 4.3).

In general, we do not expect distributions of soil physical conditions, snow depths, or carbon fluxes in the GSA to match the distributions of these variables in the watershed. The GSA is designed not to recreate the distributions of each weather forcing, soil property, and boundary condition in the watershed, but to quantify the effect of each factor across the entire space. It is likely, therefore, that some combinations of factors in the GSA simulate conditions that do not exist in the watershed. However, the GSA outputs cover the range of observed soil physical conditions, snow depths, or carbon fluxes and thereby provides important confirmation that the chosen ranges for each factor are appropriate for the site.

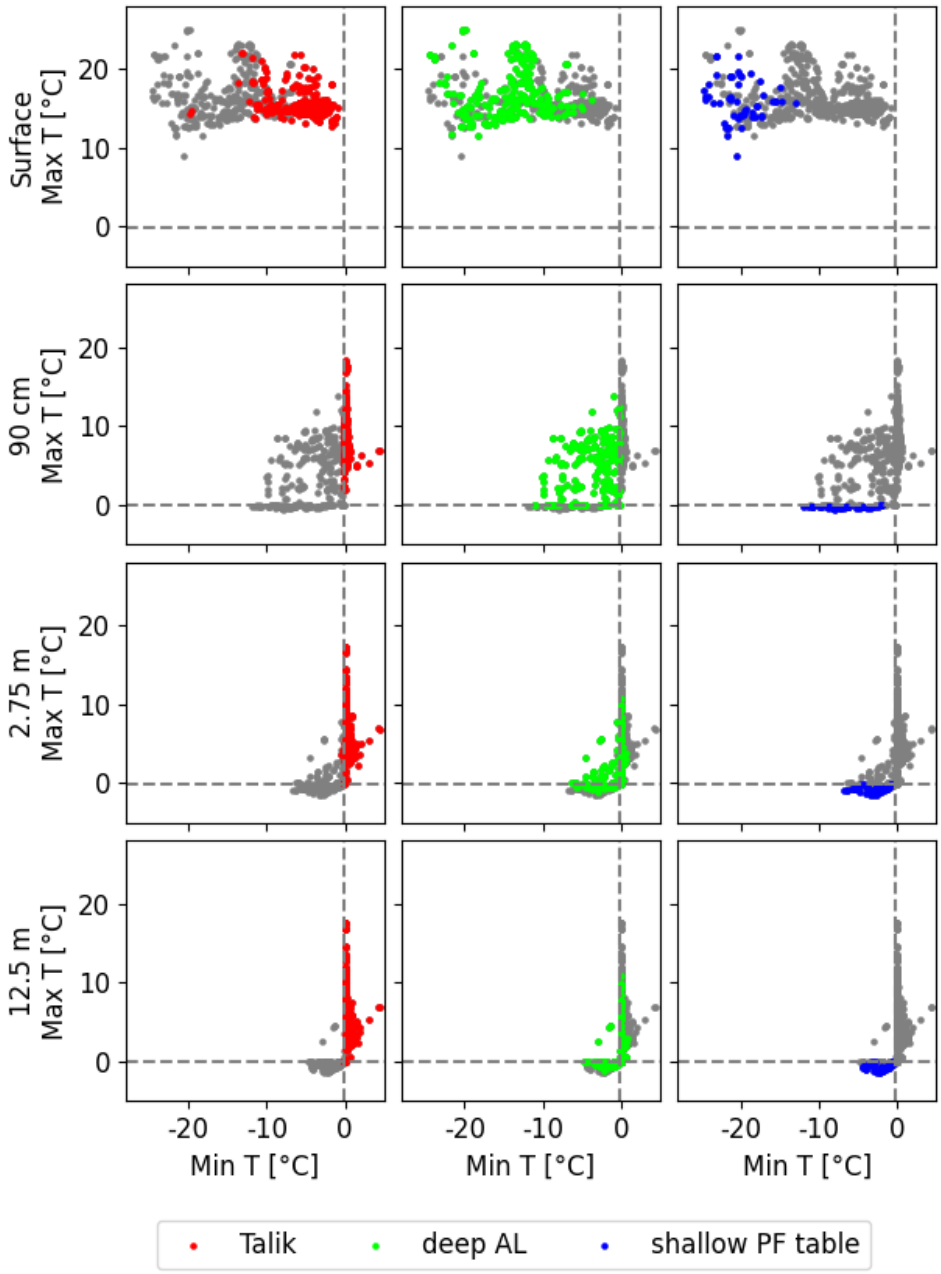

Figure 4.2: Simulated soil temperature profiles are classified into three groups. Maximum annual soil temperature is plotted against minimum annual soil temperature at the surface (a), 90 cm depth (b), 2.75 m depth (c), and 12.75 m depth (d). Each simulation is classified into Talik (red), shallow PF table (blue), and deep AL (green) based on soil temperatures at 90 cm depth.

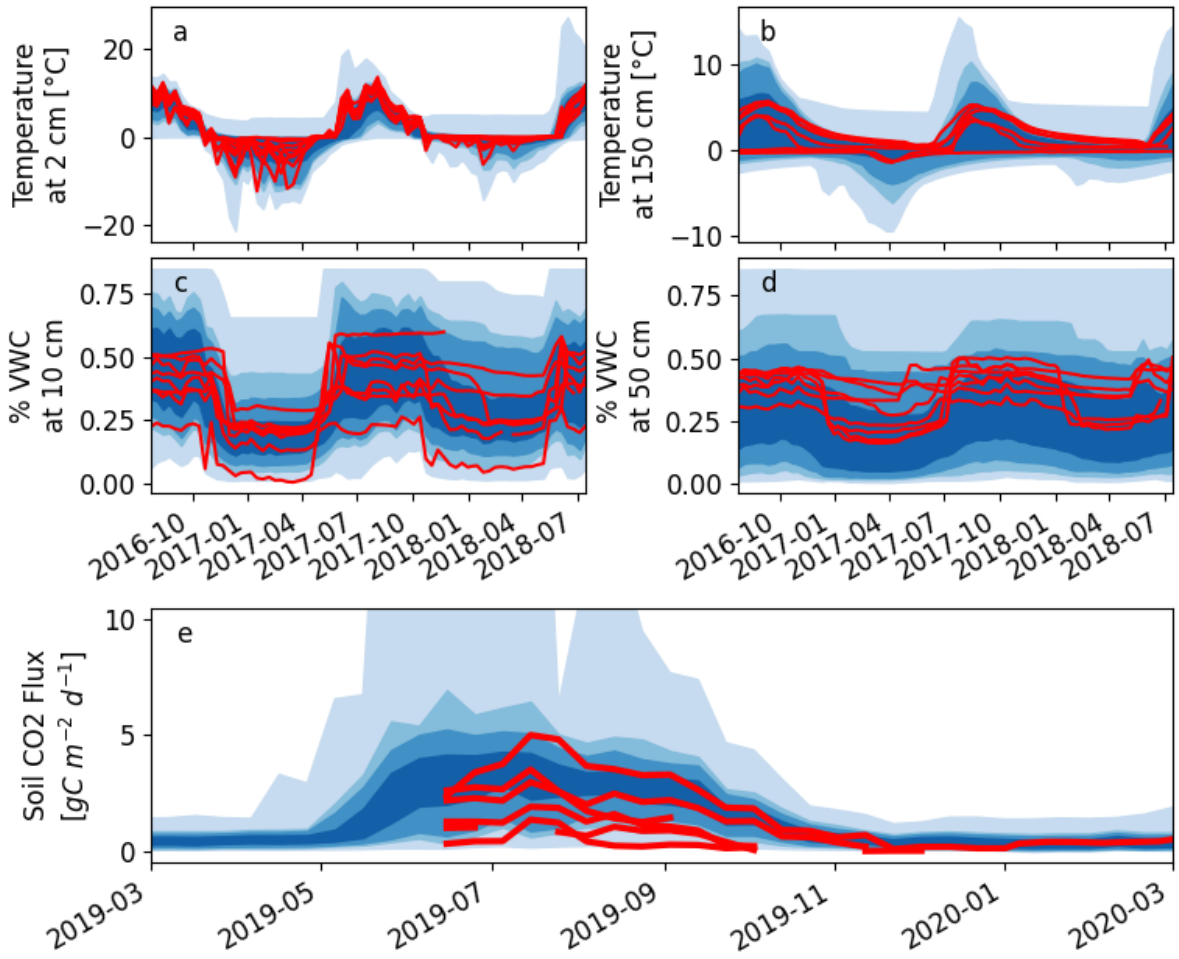

Figure 4.3: Site soil conditions are represented in the sensitivity analysis runs. Monitoring data (red lines) is shown for soil temperature for the shallowest (**a**, 2 cm) and deepest measurement (**b**, 150 cm) and soil volumetric water content (%VWC) for the shallowest (**c**, 10 cm) and deepest (**d**, 50 cm) measurement at seven distinct ecotypes distributed across the watershed between August 2016 and August 2018. Observed at six locations (red lines) and ensemble modeled (blue) soil CO_2 fluxes (**e**) for the 2019 growing season and into the fall. Distributions for the sensitivity analysis model outputs for each variable are shown blue (blue shades from light to dark represent the 0-100th, 5-95th, 10-90th, and 25-75th percentile ranges, respectively).

		Talik	deep AL	shallow PF table
Number of Runs		314	234	54
Surface	**Min**	-5.4 (2.9)	-14.0 (4.3)	-20.1 (2.7)
	Max	15.7 (2.2)	16.9 (3.0)	16.1 (2.6)
90 cm	**Min**	0.14 (0.4)	-3.7 (2.9)	-6.9 (2.6)
	Max	9.0 (2.8)	4.7 (3.4)	-0.25 (0.12)
2.75 m	**Min**	0.4 (0.6)	-1.1 (1.6)	-3.3 (1.6)
	Max	6.4 (3.8)	1.5 (2.7)	-0.8 (0.4)
12.5 m	**Min**	0.4 (0.6)	-0.7 (1.1)	-2.2 (1.1)
	Max	5.8 (4.2)	1.2 (2.7)	-0.7 (0.4)

Table 4.2: Soil temperatures (°C) for runs grouped by thermal state at 90 cm depth differ throughout soil profile. Group means for minimum and maximum soil temperatures for the years 2015-2019 at the surface, 90 cm depth, and 275 cm depth are given for Talik, deep AL, and shallow PF table runs. These groups are classified by soil temperatures at 90 cm depth. The standard deviation for each value is given in parentheses. Also shown are the number of runs for each group.

Near-surface hydrology and soil properties drive large spatial heterogeneity in soil temperatures

The Morris GSA employed in this study allows for quantitative comparison of the drivers of modeled soil temperatures. We find that local variation in near-surface hydrology and soil properties are the primary drivers of variation in soil temperature heterogeneity in the studied watershed. Specifically, snow depth, O-horizon macroporosity, external water table depth (which sets the lateral hydrological boundary conditions), and O-horizon thickness have similar or larger mean absolute EEs on 90 cm MAT than does a 2 °C offset in air temperature (MAAT; Figure 4.4a,b). The EEs of each factor on MAT are very similar throughout the soil profile (Figure 4.5). At the surface, however, MAAT has a larger relative mean EE than deeper in the soil profile, and is ranked second only to snow depth. Most of the simulations in the GSA are classified as talik (Table 4.2). Consistent with the controls on soil temperature identified by the Morris GSA, permafrost is only modeled under conditions of shallow snowpack, high O-horizon macroporosity, and low air temperature (Figure 4.6).

In the GSA, snow depth has a larger impact on modeled soil temperatures than do any of the other factors, consistent with extensive literature documenting the strong influence of snow depth on soil and ground surface temperatures in the arctic [76, 123, 156]. For the years 2015-2019, the mean absolute EE of snow precipitation on 90 cm MAT is 3.3 °C. This effect is twice as large as the mean absolute EE of the next most important factor. By providing strong insulation from cold winter air temperatures, snow creates an offset between MAAT and mean annual ground surface temperature (MAGST; Figure 4.4a,b), thereby warming soil temperatures [150]. However, interactions between snow and soil temperatures are highly

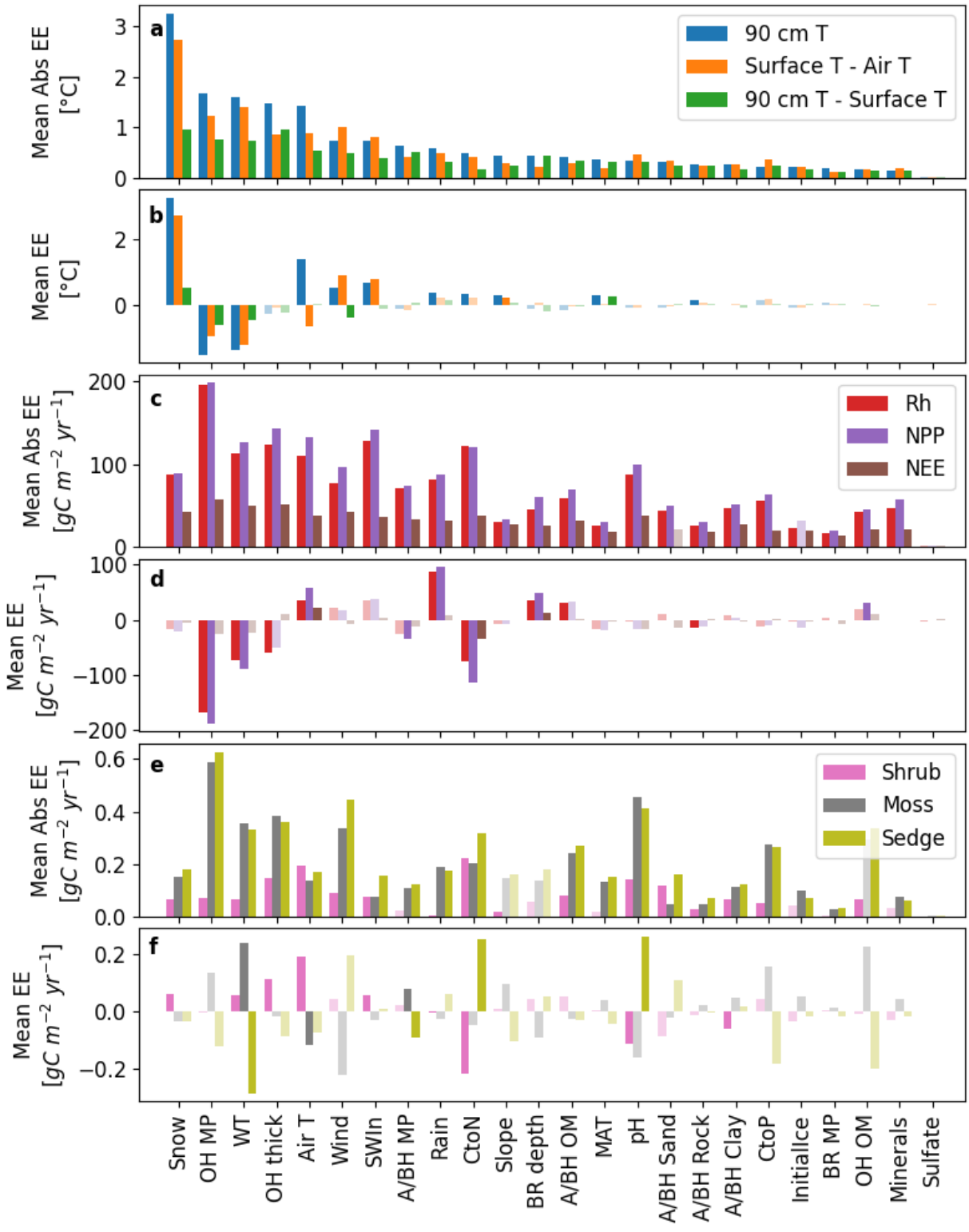

Figure 4.4: (Caption next page.)

Figure 4.4: (Previous page.) **Sensitivity analysis showing controls for soil temperature, carbon fluxes, and PFT responses.** Mean Elementary Effect (EE) and mean absolute EE for each factor are shown for mean annual soil temperature at 90 cm depth, difference between mean annual ground surface temperature and mean annual air temperature, and difference between mean annual soil temperature at 90 cm depth and mean annual ground surface temperature(**a**,**b**); mean annual R_h, NPP, and NEE (**c**,**d**); and relative dominance of shrub, moss, and sedge mean annual NPP (**e**,**f**) for the years 2015-2019. Significant factors for each variable and metric are shown in solid colors, non-significant factors are shown in semi-transparent colors. Following the methodology described in Morris (1991) [114], a factor is determined to be significant if the mean EE or mean absolute EE are larger than two times the standard error of the EE. factor descriptions and ranges can be found in Table 4.1.

nonlinear and the soil warming effect of an increasing snowpack is much larger at lower snow depths. MAT at 90 cm increases rapidly as snow precipitation approaches 70% of the prescribed value (corresponding to peak snow thickness of 80 cm), but does not change much if more snow is added to the simulation (Figure 4.7). In the GSA, a large range of soil temperatures can occur at a given snow depth, since many factors influence soil temperature, but colder temperatures are found at shallower snow depths. This simulated relationship between soil temperature at 75 cm and snow depth is consistent with site observations (Figure 4.8).

O-horizon thickness is frequently cited as an important driver of permafrost distribution at high-latitudes, with thicker O-horizons associated with shallower active layer depths and colder soil temperatures due to the low thermal diffusivity of organic matter [78, 182]. Zhu et al., 2019). Here, in contrast, O-horizon thickness EE can be either positive or negative due to interaction effects with other factors (Figure 4.7). The net result is a small and non-significant mean EE for O-horizon thickness on mean annual 90 cm depth soil T, even though the mean absolute EE of O-horizon thickness on 90 cm MAT is comparable to the mean absolute EE of air temperature (Figure 4.7). The sign of the EE of the O-horizon thickness on 90 cm MAT is linked to the water content of the top 20 cm of soil such that an increase in O-horizon thickness results in an increase in soil temperature in wet soils and a decrease in soil temperatures in dry soils ($R^2 = 0.65$, Figure 4.9). The water content of the O-horizon impacts heat transfer to deeper soils by modifying soil thermal properties and latent heat exchanges in the short-term, and PFT competitive dynamics over longer time frames.

The response of soil temperatures to near-surface soil properties that affect water fluxes in the GSA demonstrates that near-surface hydrology is an important control on soil temperature. The magnitude of the offset between MAAT and MAGST created by seasonal snowpack is dependent on heat transfer from the atmosphere to the soil during the summer months, which is strongly affected by the water content of near-surface soils [137, 140].

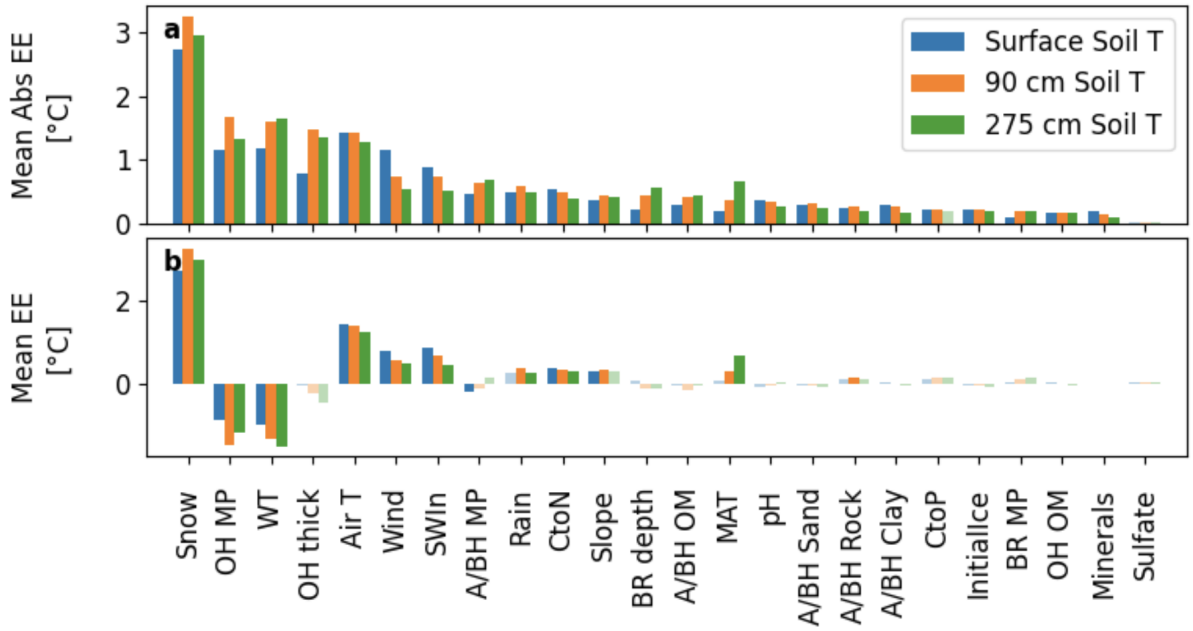

Figure 4.5: Controls on mean annual soil temperatures are similar across depths. Mean Elementary Effect (EE; **a**) and mean absolute EE (**b**) for each factor are shown for mean annual soil temperature at the surface, 90 cm depth, and 275 cm depth. Significant factors for each variable and metric are shown in solid colors, non-significant factors are shown in semi-transparent colors. Following the methodology described in Morris (1991), a factor is determined to be significant if the mean EE or mean absolute EE are larger than two times the standard error of the EE. factor descriptions and ranges can be found in Table 4.1.

The presence of macropores in soils (or fractures in bedrock) increases laminar flow and drainage in the model, particularly in organic soils which otherwise have high water retention. O-horizon macroporosity, which affects the drainage of near-surface soils, has a large mean absolute EE (1.7 °C, ranked second of all factors) and a large negative mean EE (-1.5 °C) on 90 cm MAT (Figure 4.4a,b). In contrast, the mean absolute EE on 90 cm MAT of A/B-horizon macroporosity, which affects the drainage of deeper soils, is much smaller (0.6 °C), and the mean EE is not significant (Figure 4.4a,b). Below the water table, soils will be saturated even if they have large drainage capacity. In these simulations, the external water table factor sets the depth of lateral discharge and recharge of water such that a shallower (deeper) external water table will have wetter (drier) near-surface soils. This factor has a large mean absolute EE (1.6 °C) and a large negative mean EE on 90 cm MAT (-1.4 °C; Figure 4.4a,b), but the influence of the external water table is highly non-linear. MAT at 90 cm increases if the external water table rises close to the surface, causing more surface

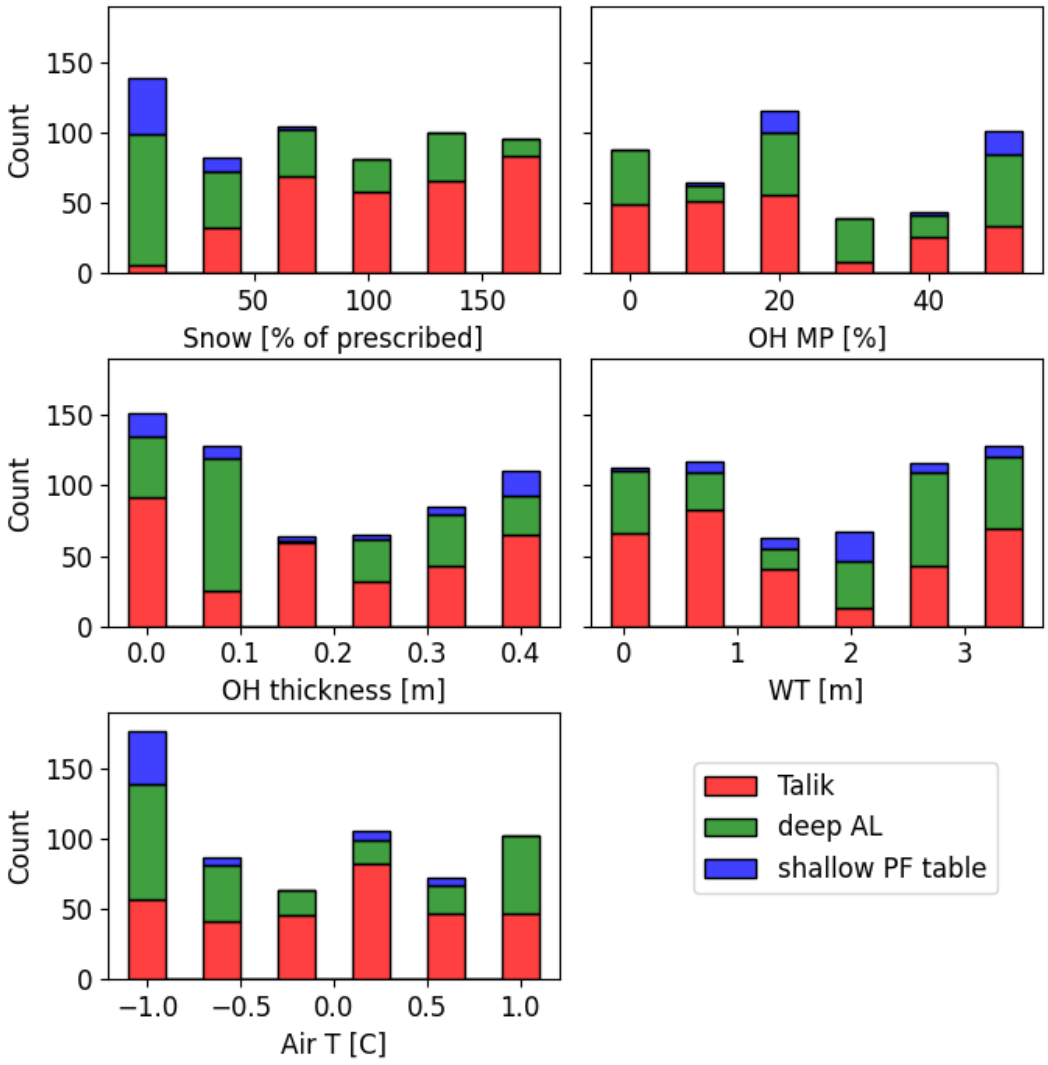

Figure 4.6: Soil thermal regimes are driven by air temperature and landscape heterogeneity. The number of runs classified as talik (red), deep AL (green), and shallow PF table (blue) are shown for each factor value for the snow, O-horizon macroporosity, water table depth, O-horizon width, and air temperature factors. factor descriptions and ranges can be found in Table 4.1.

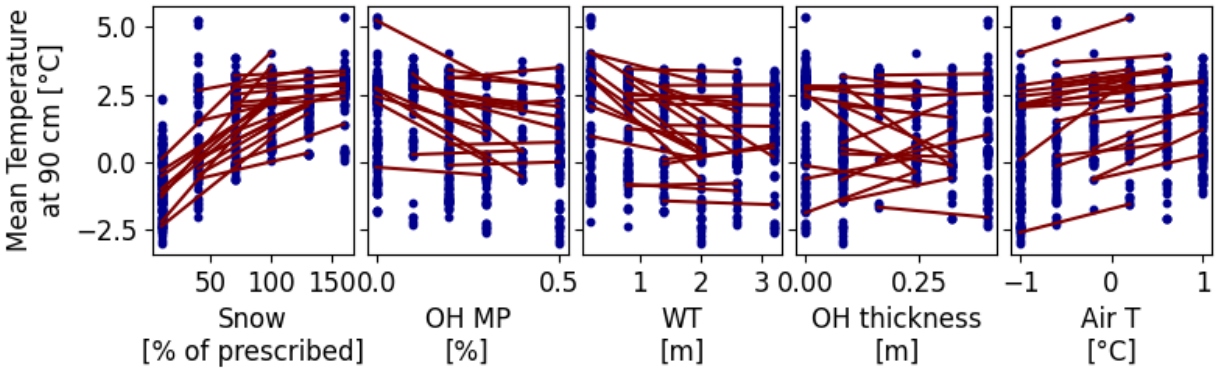

Figure 4.7: Responses of modeled soil temperature to factor changes are nonlinear and exhibit interaction effects. Mean annual soil temperature at 90 cm depth is plotted against the normalized snow precipitation, O-horizon macroporosity, water table depth, O-horizon thickness, and air temperature factor values for each model run (blue dots). In each subplot, the red lines link two runs associated by a change in the factor and represent the corresponding change in soil temperature. factor descriptions and ranges can be found in Table 4.1.

wetting and consequently heat transfer, but does not change much for external water tables deeper than 1 m (Figure 4.7).

Soil water content further influences 90 cm MAT via changes in thermal conductivities associated with freeze-thaw processes. In permafrost systems, increased thermal conductivity and therefore heat transfer in frozen vs unfrozen soils creates a negative offset between MAGST and mean annual soil temperatures [137, 140]. Because of their impact on soil porosity and water influx, drainage, and retention, the O-horizon thickness, O-horizon macroporosity, and external water table depth control changes in soil water and ice content that are responsible for seasonal differences in soil thermal conductivity in *ecosys*. These factors are the most important controls in the GSA on the thermal offset between MAGST and 90 cm MAT (Figure 4.4a,b). Snow also has a strong impact on the modeled thermal offset, even though it is not the dominant control, because it has a strong influence on the ratio of freezing days to thawing days throughout the soil profile.

Tall deciduous shrub growth is associated with specific combination of subsurface properties

Vegetation composition in *ecosys* is emergent rather than prescribed, and results from competition for light, water, and nutrients. Shrub, moss, and sedge were the most successful PFTs in the GSA, while lichen and grass were never the dominant PFT. We found that the relative success of the shrub, moss, and sedge PFTs are linked to variability in modeled

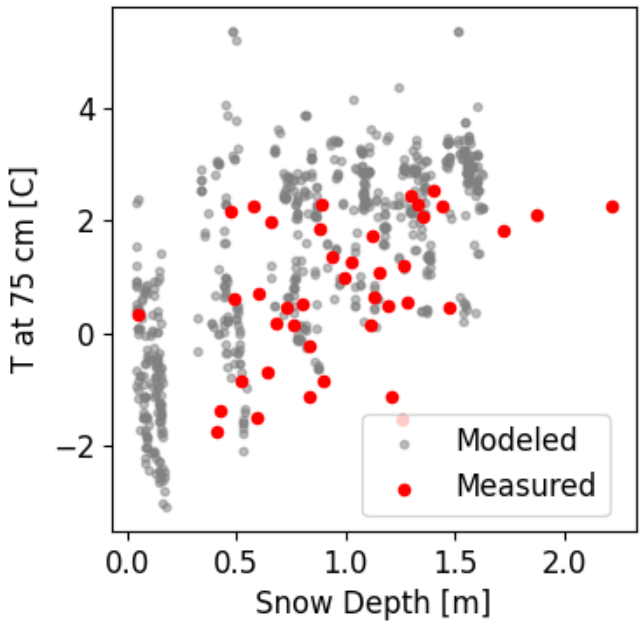

Figure 4.8: Modeled response of soil temperature to differences in snow depths is consistent with site data. Mean annual soil temperature at 75 cm depth is plotted against maximum snow depth for simulations (gray) and site data (red) that was collected at many locations across the studied watershed between 2019 and 2020 [32].

subsurface conditions. In particular, factors that affect soil temperature and water content (OH MP, WT, OH thickness, Air T), nitrogen availability, (C:N, OH OM, A/B OM), and pH have large impacts on PFT competition (Figure 4.4e,f).

Whereas moss and sedge PFTs are productive over a large range of conditions, the shrub PFT is sensitive to thermal and hydrological controls on nitrogen uptake and grows only in a specific combination of subsurface conditions (Figure 4.10). In particular, tall deciduous shrubs grow almost exclusively in simulations with talik, near-surface winter temperatures warmer than -1 ℃, summertime near-surface water content between 30% and 75% of soil porosity, and low humus C:N ratios (10-15). In these simulations, humus C:N ratios are a strong control on soil nitrogen availability. Since minimum C:N ratios of microbial biomass are fixed in the model, microbial decomposition in nutrient rich soils leads to net mineralization and increased plant nutrient availability [63]. Additionally, soil water content is

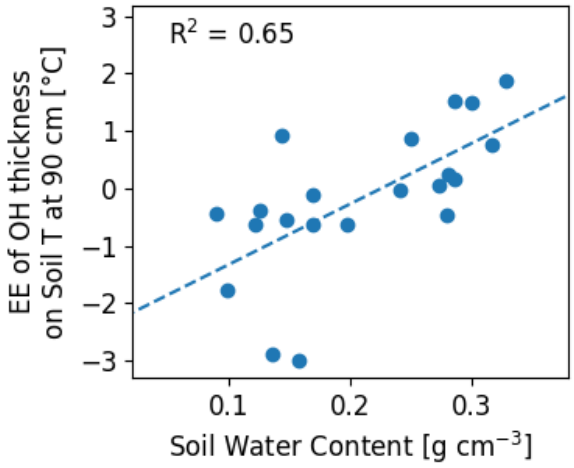

Figure 4.9: The change in soil temperature associated with an increase in O-horizon thickness depends on soil hydrology. The change in mean annual soil temperature at 90 cm depth that results from a 24 cm increase in O-horizon thickness is plotted against the water content of the top 20 cm of soil. Here, the water content is calculated as the sum of the ice and liquid water content weighted by density.

an important control on shrub nutrient acquisition, as nutrient mineralization, fixation, and uptake are inhibited by water stress at low soil water contents and by oxygen stress at high soil water contents [108]. Finally, the association between warm winter soils and shrub productivity is driven by non-growing season nitrogen uptake. Plant community structure and species dominance is shaped by differing nutrient acquisition strategies in high-latitude ecosystems [101] and non-growing season nutrient uptake, which occurs at high rates only in Talik runs (Figure 4.11), gives a competitive advantage to shrub PFTs at high-latitudes [134]. We note that non-growing season nutrient dynamics and plant uptake has also been shown to be important for global carbon and nitrogen dynamics [133].

Talik runs have higher rates of biological activity than shallow PF table runs

The response of ecosystem carbon fluxes to subsurface heterogeneity is complex. In the GSA, R_h and NPP range from near zero to more than 600 gC m^{-2} yr^{-1} (Figure 4.13). The mean absolute EEs of many of the factors in the GSA on R_h and NPP are large. Air temperature is an important control on ecosystem carbon fluxes, but incoming shortwave radiation has a larger mean absolute EE for both R_h and NPP. In addition, there are several factors related to subsurface properties (OH MP, WT, OH thickness, C:N) that have similar or larger mean

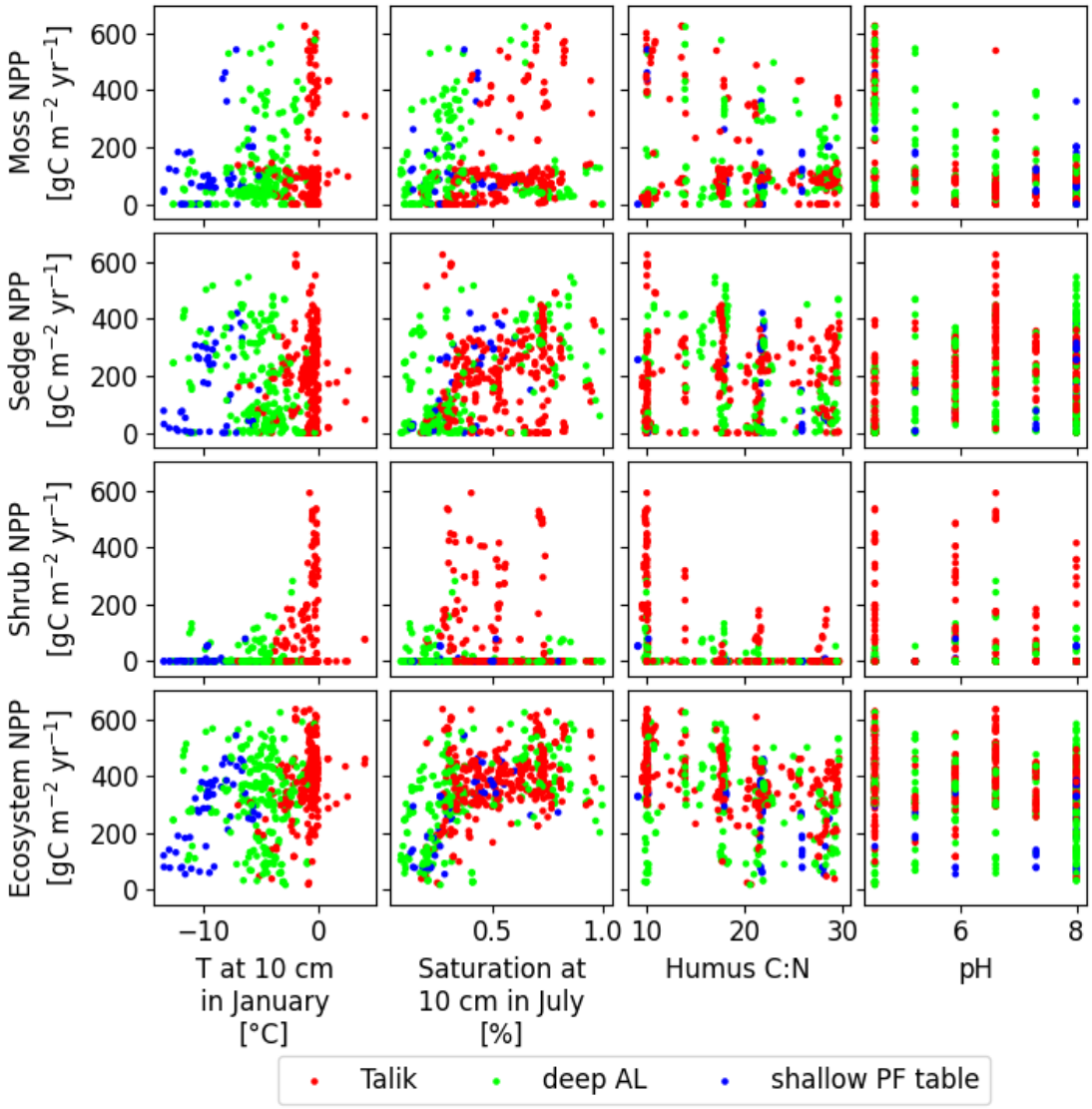

Figure 4.10: Modeled shrubs are only productive in a specific set of subsurface conditions. Moss, sedge, and shrub NPP for each simulation are plotted against January soil temperature at 10 cm depth, July soil saturation at 10 cm depth, humus C:N, and pH. Each simulation is classified into Talik (red), deep AL (green), or shallow PF table (blue) based on soil temperatures at 90 cm depth.

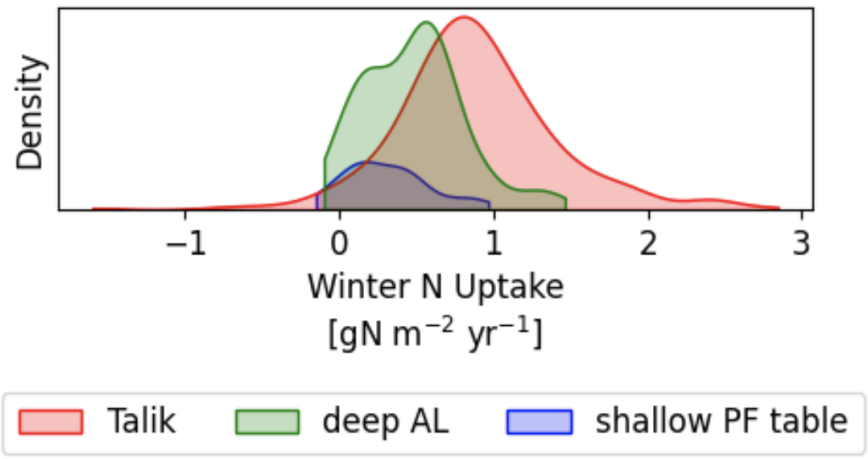

Figure 4.11: Non-growing season plant N uptake is associated with soil thermal state. Kernel density estimates of distributions of plant N uptake for the months October - March are shown for groups of simulations classified by soil temperatures at 90 cm depth (shallow PF table - blue; Deep AL - green; Talik - red). The distributions share a common normalization, such that the area under all curves for a given flux sums to one.

absolute EEs on R_h and NPP than both air temperature and incoming shortwave radiation (Figure 4.4c,d). In general, many of the factors that are important for soil temperatures are also important for R_h and NPP, although the relative importance of each factor is different for the carbon fluxes than for the soil temperatures.

Due to the complexity of the system, we found that a large range of modeled conditions can reproduce observed soil CO_2 fluxes. At one site, we identified 22 of the GSA simulations that accurately matched the observed soil CO_2 fluxes (Nash-Sutcliffe coefficient > 0.93, Figure 4.12). We note that these 22 simulations span the range of model factors and emergent soil moisture, temperature, and vegetation cover, highlighting the equifinality inherent in this complex system [97, 154]. This equifinality is likely due to interactions between soil temperature and moisture with other factors such as soil carbon, nitrogen cycling, pH, and incoming shortwave radiation, that are shown in the GSA to have a large impact on vegetation dynamics and carbon fluxes (Figure 4.4c-f).

Although system complexity creates large variability in modeled R_h and NPP, soil thermal state is an important driver of carbon flux heterogeneity in the GSA. In particular, R_h (NPP) is 78.0 gC m^{-2} yr^{-1} (104.9 gC m^{-2} yr^{-1}) higher when drawn from the Talik distribution than when drawn from the shallow PF table distribution according to the Wilcoxon rank sum test (Figure 4.13, Table 4.3). Indeed, the impact of the soil thermal regime on NPP and R_h is larger than the impact of air temperature over the range covered by this GSA. R_h (NPP) is only 55.0 gC m^{-2} yr^{-1} (62.1 gC m^{-2} yr^{-1}) larger in runs with high air temperature (Air T

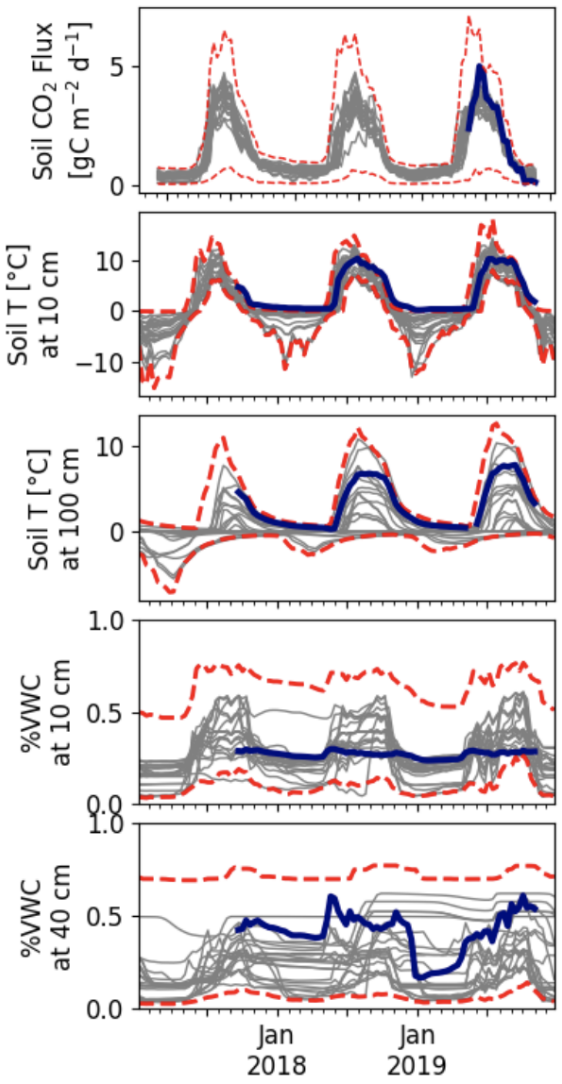

Figure 4.12: Observed soil CO_2 fluxes can be reproduced with a large range of modeled soil thermal and hydrological conditions. Observations of soil CO_2 flux, soil temperature at 10 and 100 cm, and % VWC at 10 and 40 cm for the years 2017-2019 are shown in blue. Outputs for 22 model runs that matched the observed CO_2 flux with Nash-Sutcliffe coefficient > 0.93 are shown in gray for each variable. For each variable, 5th and 95th quantiles of the GSA simulations are shown in dashed red lines.

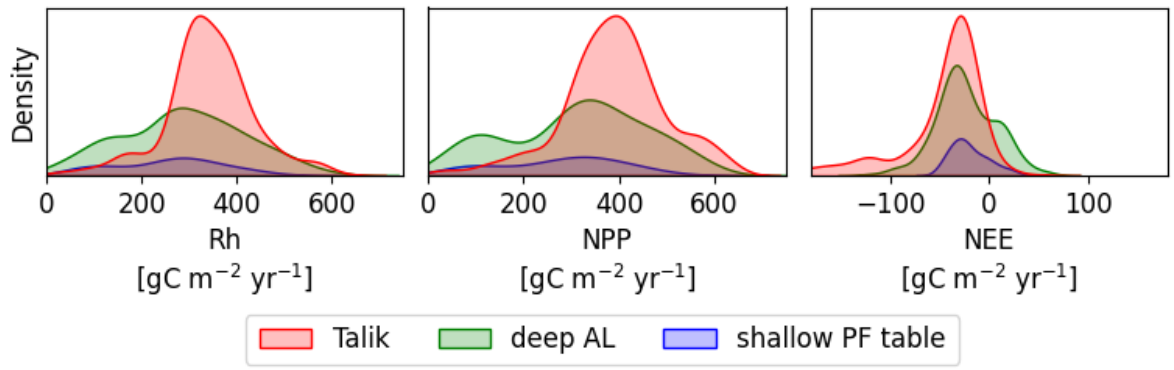

Figure 4.13: Distributions of carbon fluxes for groups classified by soil temperature at 90 cm depth are distinct. Kernel density estimates of distributions of microbial respiration (R_h), NPP, and NEE (negative values correspond to carbon uptake) are shown for groups of simulations classified by soil temperatures at 90 cm depth (shallow PF table - blue; Deep AL - green; Talik - red). The distributions share a common normalization, such that the area under all curves for a given flux sums to one.

offset >= 0.6 °C) than in runs with low air temperature (Air T offset <= -0.6 °C; Wilcoxon rank sum test; Table 4.3).

Missing representation of subgrid heterogeneity introduces bias in estimates of watershed NEE

Plant and microbial activity are tightly coupled through exchanges of carbon and nitrogen, so simulated R_h and NPP generally respond jointly to subsurface heterogeneity. Increased microbial activity leads to increased plant nitrogen uptake ($R^2 = 0.88$; Figure 4.14b) which supports increased carbon fixation by plants ($R^2 = 0.89$, Figure 4.14d). Conversely, increased NPP leads to increased labile carbon inputs into the soil ($R^2 = 0.97$; Figure 4.14c) that drives increased microbial activity, and hence R_h ($R^2 = 0.99$; Figure 4.14a). Because of this strong coupling between R_h and NPP, NEE has much lower variability across the simulations (Figure 4.13). NEE for a sample drawn from the Talik distribution is 15.6 gC m^{-2} yr^{-1} more negative than a sample drawn from the shallow PF table distribution (i.e., greater carbon uptake in the Talik simulations; Wilcoxon rank sum test; Table 4.3), but this difference is small compared to the differences between the distributions of NPP and R_h discussed above. In fact, this difference may be attributed to the long left tail in the Talik distribution that is not present in the shallow PF table or deep AL distributions. Simulations with NEE more negative than -100 gC m^{-2} yr^{-1} (i.e., higher net ecosystem carbon uptake) were found almost exclusively in Talik simulations.

Two mechanisms are responsible for breaking the coupling between R_h and NPP in the

	R_h [gC m^{-2} yr^{-1}]	NPP [gC m^{-2} yr^{-1}]	NEE [gC m^{-2} yr^{-1}]
Talik - shallow PF Table	$78.0^{110.5}_{49.8}$ ***	104.9—$69.7^{141.9}$ * **	-$15.6^{-23.5}_{-8.6}$ * **
High air T - low air T	$55.0^{77.8}_{31.4}$ * **	$62.1^{88.9}_{35.9}$ * **	-$4.8^{-9.4}_{-0.5}$*

Table 4.3: Distributions of biogeochemical fluxes are statistically distinct when grouped by soil thermal state and air temperature. Estimates from the Wilcoxon rank-sum test for differences in location of the median of a biogeochemical flux when grouped by soil thermal state (Talik - shallow PF Table) and air temperature (high air T - low air T) are given for R_h, NPP, and NEE. 95% confidence intervals are given in the subscripts and superscripts. The Wilcoxon rank-sum test is used to reject the null hypothesis that there is no shift in the locations of two distributions. P-values for this test are given for each flux and pairs of distributions. P-values less than 0.05 are denoted by *, and p-values less than 10^{-5} are denoted by ***.

runs with the highest values of net carbon uptake. First, saturated conditions caused by a shallow water table slow decomposition of plant carbon inputs due to lower energy yields from redox reactions conducted by anaerobic heterotrophic microbial populations, suppressing R_h relative to NPP (Figure 4.15). Second, allocation to woody structural carbon leads to high carbon retention in tall, productive shrubs (NPP > 200 gC m^{-2} yr^{-1}). While moss and sedge PFTs with NPP > 200 gC m^{-2} yr^{-1} lose on average 92% and 97% of above- and below-ground carbon fixed each year to litter carbon or root exudates, productive shrubs lose only 66%. Greater carbon retention reduces the percentage of newly fixed and highly labile carbon that is available to microbial decomposition each year, and nearly all of the simulations with productive shrubs have net carbon uptake greater than 100 gC m^{-2} yr^{-1} (Figure 4.15).

Inclusion of landscape heterogeneity can have a large impact on modeled estimates of watershed-scale NEE. To demonstrate this point, we ran a single simulation of the studied watershed using soil data extracted from the Northern Circumpolar Soil Carbon Database (Hugelius et al., 2013) and unmodified weather forcing data. This simulation mimics the setup of a typical large-scale land model used in Earth System Models (e.g., [133, 182]). In this simulation, sedge is the dominant PFT and the shrub PFT did not grow at all. The mean net carbon uptake for GSA outputs without tall shrubs is 24 gC m^{-2} yr^{-1}. According to a vegetation map of the watershed, however, 45% of the studied watershed is covered by willow shrubs ([86]). If this vegetation data is used to weight the GSA outputs, the estimated net carbon uptake for the watershed is 77 gC m^{-2} yr^{-1}. The estimate of watershed net carbon uptake that includes landscape heterogeneity is three times larger than the estimate of a single model run that does not simulate productive shrub growth.

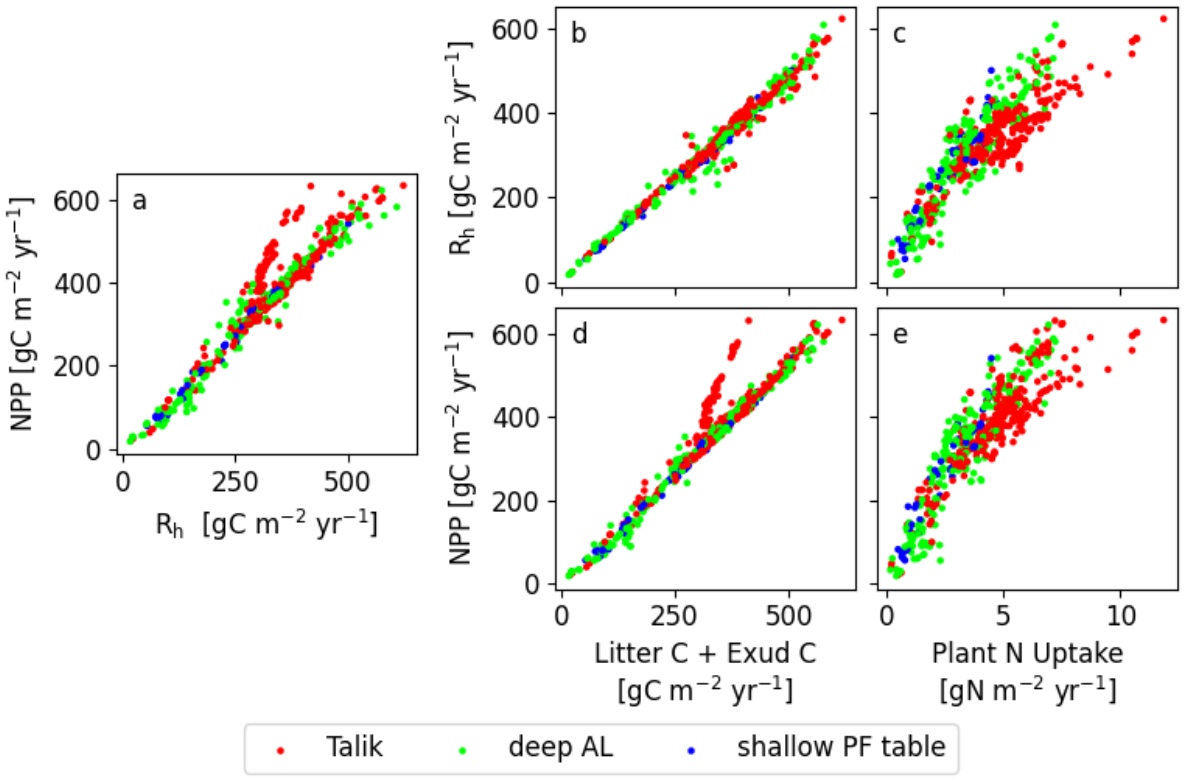

Figure 4.14: Plant and microbial activity are tightly coupled through exchanges of carbon and nitrogen. Annual R_h and NPP are plotted against annual carbon inputs to the soil (litter carbon + root exudate carbon) and against annual plant nitrogen uptake. Each simulation is classified into Talik (red), deep AL (green), or shallow PF table (blue) based on soil temperatures at 90 cm depth.

Methane Production is Sensitive to Hydrology and Vegetation

Most of the runs in the sensitivity analysis had very low methane fluxes. 75% of the simulations were characterized by annual methane fluxes less than 1 gC m^{-2} yr^{-1}. This is consistent with recent findings that a small surface area contributes an outsize proportion of the high-latitude methane budget [40].

In the GSA, we find that simulations with outlying values of methane emission (methane flux greater than 15-20 gC m^{-2} yr^{-1}) are characterized by a specific set of environmental conditions related to the energetics of microbial metabolism (Figure 4.16). First, these outlying runs are associated with anaerobic conditions caused by moderately to fully saturated near surface soils. Near-surface anaerobic conditions are necessary since methanogenic bacteria cannot grow in the presence of oxygen and methanotrophs (soil bacteria that oxidize methane

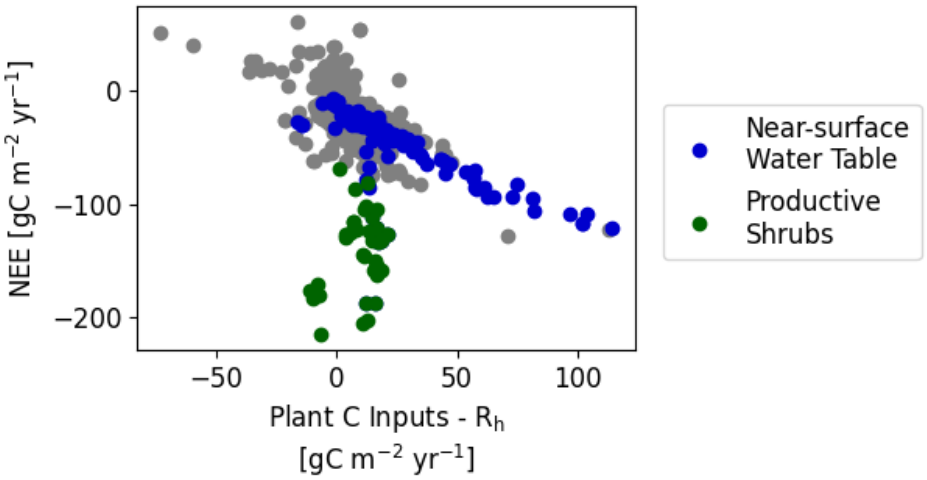

Figure 4.15: Large net carbon uptake in simulations with near-surface water tables and productive shrubs is achieved via different carbon storage mechanisms for each group. NEE is plotted against the difference between yearly plant C inputs to the soil (litter C and root exudates) and yearly microbial respiration (R_h) for each simulation. Runs with a near-surface water table (depth to external water table = 0.2 m) are shown in blue, runs with productive shrubs (shrub NPP > 200 gC m^{-2} yr^{-1}) are shown in green, and all other runs are shown in gray.

before it can be emitted to the atmosphere) are aerobic [119]. Second, the outlying runs are associated with warm winter soils at 90 cm depth that allow microbial activity to continue for longer. Finally, the sedge PFT grows in all of the simulations with high methane fluxes. Sedges have arenchyma (tube-like structure that allows for gas exchange between leaves and roots) which allow them to grow in saturated conditions. Sedge arenchyma have also been shown to facilitate transfer of methane from the subsurface to the atmosphere [159].

The sustained global warming potential ($SGWP_{100}$) of the highest methane fluxes in the GSA (20 - 100 gC (CH_4) m^{-2} yr^{-1}) is equivalent to a CO_2 flux of 330 - 1620 gC (CO_2) m^{-2} yr^{-1} [120]. This is 1.5 to 8 times higher than the value of the highest net carbon uptake in the GSA (Figure 4.15).

Caveats and uncertainties

Although our *ecosys* simulations represented many of the important processes for high-latitude carbon cycling, we did not explore here dynamics associated with thermokarst, fire, or herbivory [105]. Additionally, the simulations were performed using a 1D soil column which is typical of current large-scale land models but may overlook important processes that occur in 3D such lateral flow of heat, water, carbon and nutrients [76, 108]. Further,

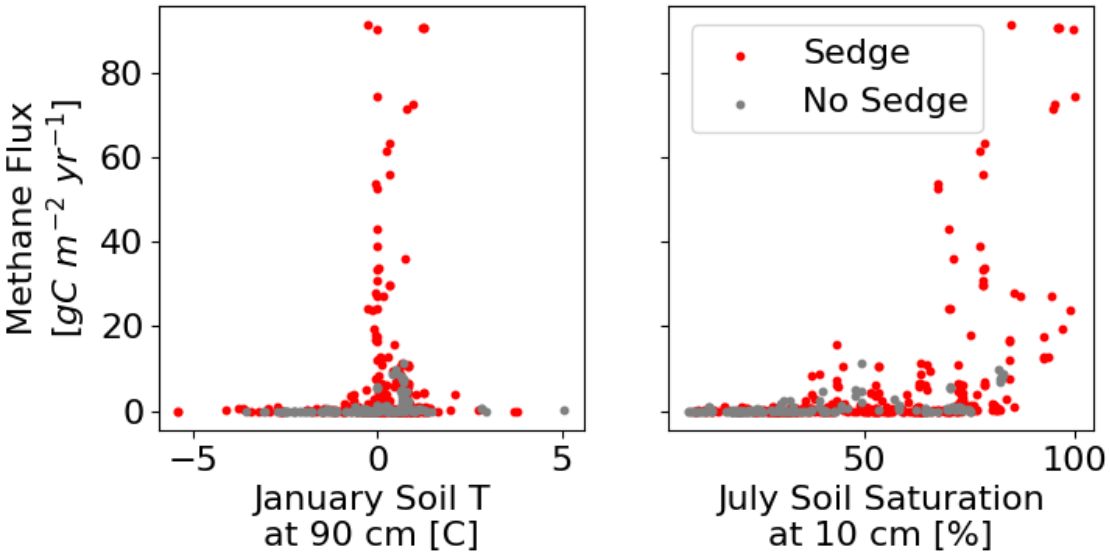

Figure 4.16: Methane hotspots are associated with warm, near-freezing winter soils, saturated near-surface condtions, and the presence of sedges. Annual methane fluxes are plotted against January soil temperatures at 90 cm (left) and July soil saturation at 10 cm (left). The simulations with sedge NPP greater than 50 gC m^{-2} yr^{-1} are shown in red, and all other runs are shown in gray.

our weather forcing perturbations were imposed for the full duration of the simulations (i.e., 183 years), so that short-term dynamics responses to changes were not analyzed, although they can be important (e.g., [16]).

4.4 Conclusions

We show that near-surface hydrology and soil properties drive heterogeneity in soil temperatures, PFT dynamics, and carbon fluxes. We performed a Morris Global Sensitivity Analysis (GSA) of factors related to soil properties, landscape position, and weather forcings. The resulting simulations cover the range of soil temperatures, soil water contents, and soil CO_2 fluxes observed throughout the watershed. In the GSA, snow and factors that affect O-horizon saturation and drainage have a larger impact on soil temperatures than a 2 °C variation in MAAT. We split the simulation runs into groups based on soil temperatures at 90 cm depth and found that near-surface talik soils have higher R_h and NPP than near-surface permafrost soils. Because of strong coupling between NPP and R_h, the distribution of NEE is strongly peaked at a value of moderate carbon uptake for near-surface permafrost and near-surface talik runs. The near-surface talik NEE distribution is strongly left skewed,

however. Tall productive shrubs grow only when talik is present, January near-surface soil temperatures are warmer than -1 °C, summertime near-surface water content is between 30% and 75% of soil porosity, and C:N ratios are lower than 15. Simulations with high shrub productivity decouple R_h from NPP by accumulating carbon in woody material, leading to very high net carbon uptake.

Besides the strong impact of snow on subsurface thermal regimes, organic soils are typically thought to protect permafrost, regardless of water content [39, 79]. Here, however, we find that the water content of the O-horizon determines whether it will insulate soils. To our knowledge, this finding has not been discussed previously. This result has important implications for ecosystem responses to climate warming at high latitudes. Further investigation is needed to verify this effect in the field, and to determine if it holds only in warm, transitional permafrost environments or if it applies more broadly in the high latitudes.

In arctic tundra ecosystems, patches of tall shrubs are associated with warmer winter soils and increased likelihood for talik formation than surrounding patches of low-lying tundra vegetation [45, 115]. This association is attributed to wind-driven accumulation of snow in shrub canopies, implying that talik formation follows shrub growth [76]. In the simulations presented here, however, there is no representation of snow trapping in shrub canopies. Nevertheless, we find that tall shrubs are only productive in talik soils when winter soils are warm enough to permit high rates of nutrient uptake. This result is important because it demonstrates that the association between talik and tall shrubs is driven by biogeochemical processes in addition to the physical snow-trapping mechanism.

Our results indicate that missing representation of landscape heterogeneity in large-scale Earth System Models (which are typically run at resolutions coarser than 50 km) can bias estimates of soil temperatures, vegetation dynamics, and carbon balance. For example, the success of the shrub PFT in our simulations is strongly dependent on local variability in near-surface hydrological conditions and estimated net carbon uptake for the studied watershed is three times higher when the measured shrub distribution is accounted for. These results demonstrate the need for better representation of subgrid hydrology and vegetation dynamics in terrestrial ecosystem models, and higher-resolution observations of soil and vegetation properties for model parameterization and validation.

Chapter 5

Machine learning models inaccurately predict current and future high-latitude carbon balances

Estimates of current and future high-latitude carbon balance are highly uncertain. This uncertainty can be attributed to high spatial variability in ecosystem processes (as discussed in Chapter 4), a complex and interacting set of environmental drivers that will shift with climate changes (as discussed in Chapter 3), and limited data due to harsh environmental conditions and remoteness of northern lands. Machine learning methods are capable of extracting highly complex and non-linear relationships between driving and response variables, and such methods have been applied in a number of recent high-profile studies to upscale site observations of ecosystem processes and forecast their response to climate change. In this chapter, machine learning models of high-latitude carbon fluxes are trained on outputs from *ecosys* and their performance is evaluated under current and future climate conditions. The results demonstrate that there is currently insufficient data to produce reliable estimates of current high-latitude carbon budgets using machine learning. Further, because of changing CO_2 concentration, vegetation dynamics, and litter carbon inputs, machine learning models cannot forecast the response of high-latitude carbon fluxes to climate change.

5.1 Introduction

Direct measurements of ecosystem carbon exchanges are performed using techniques such as eddy-covariance (EC), chambers and long-term plot based observations, but these methods can only be applied at local scales and provide spatially sparse estimates. Uses of this data to inform regional estimates of current-day carbon fluxes are typically divided into two approaches. Process-based terrestrial ecosystem models, which simulate physical, chemical, and biological responses to driving environmental variables, use site data for calibration and to validate model predictions. Upscaling methods, in contrast, use the data to generate

statistical or machine learning (machine learning) models which are then applied to predict across a larger study domain. machine learning models typically outperform statistical regression-based approaches in predictive power due to their ability to capture complexity, non-linearities, and interaction effects [165]. In recent years, many studies have applied machine learning models to upscale carbon fluxes at regional [1, 165, 118, 127, 132] and global [80, 179] scales. Machine learning approaches have also been applied to upscale other ecosystem processes including vegetation dynamics [10, 126], crop yields [30], and changes in soil carbon stocks [117, 113].

Machine learning model performance is strongly dependent on the size and spatial distribution of the training dataset, particularly as the complexity of the modeled system increases [131]. High-latitude ecosystems are highly complex systems with tightly coupled carbon, heat, water, and nutrient cycles characterized by strong heterogeneity, feedback loops, and interaction effects [44, 84, 121, 12, 168, 11, 76, 108, 60, 21, 79, 7]. However, data availability at high-latitudes is very limited. Alaska is the high-latitude region with the highest density of EC flux towers (25 AmeriFLUX towers were active at some point during the period 2010-2020) but, given a footprint of each flux tower of 1 km^2 [160], these EC flux towers monitor only 0.002% of the Alaskan land surface (1,481,346 km^2). Performance of machine learning models of highly complex ecosystem processes trained on such limited data may suffer from underspecification [31], shortcut learning [48], and other structural mismatches between the available data and the underlying dynamics [5]. Since these effects cannot be quantified using the training dataset, commonly employed techniques like k-fold cross-validation (CV) may lead to overestimation of model performance. This in turn may lead to overconfidence in the machine learning model predictions, particularly since they are derived from data.

Some machine learning upscaling studies [118, 10, 126, 117] use machine learning models generated using training data from current climate conditions to forecast responses of ecosystem processes to decades of climate change. This approach is attractive because while machine learning models are challenging to generate they are easy to use for predictions. However, many factors that drive and interact with ecosystem processes will change significantly under future climate conditions (e.g., atmospheric CO_2 concentration, air and soil temperatures, nutrient availability, vegetation composition that are beyond the training domain), leading to an expected degradation of machine learning model performance. Validation of machine learning model performance under future climate conditions is not possible today, and given the low interpretability of typical machine learning models, it is not clear how strongly machine learning model performance will be affected by these types of future changes.

In this study, we use outputs from *ecosys* to train and evaluate the performance of boosted regression tree (BRT) machine learning models across Alaska. We first examine the impact of variation in spatial and temporal training data coverage on machine learning model predictions of microbial respiration (R_h), net primary productivity (NPP), and net ecosystem exchange (NEE) across Alaska. Then, we evaluate the ability of the highest performing machine learning model to forecast the response of these carbon fluxes to climate change throughout the 21st century. Finally, we use convergent cross-mapping (CCM) to identify

and rank the drivers of machine learning model bias in R_h and NPP at the end of the century. Since the internal complexity of a process-model is much smaller than that of real-world ecosystem processes and the quality of simulated data is perfect, the performance of these machine learning models is significantly better than if they were trained on real-world datasets. However, this exercise allows us to estimate the 'best-case' performance of machine learning models used to upscale and forecast high-latitude carbon balances.

5.2 Methods

Boosted Regression Trees

Boosted regression tree (BRT) machine learning models are linear combinations of decision trees that have been iteratively fit to reduce a loss function. BRT models are able to capture non-linear response curves and interaction effects between variables [41] and were used to upscale carbon fluxes in Natali et al (2019) [118] and Virkkala et al (2021) [165]. We implemented our BRT models in R using the 'gbm' package [66] with a gaussian error distribution, bag fraction of 0.5, tree complexity of 5, and a learning rate of 0.1. Cross validation was used to identify the optimal number of trees for each model.

Convergence Cross-Mapping

Convergence cross-mapping (CCM) is a method of causal inference that uses nonlinear state space reconstruction to test for causation in weakly coupled dynamical systems [153]. CCM has been used to infer causal relationships in several climate, earth science, and ecological studies [164, 170, 37, 153]. In CCM, reconstructed state space of one variable is used to predict the reconstructed state space of a second variable. Cross-map skill is the correlation between the predicted and actual reconstructed state space, with high skill indicating a strong causative effect.

Experimental Design

In this study, we create BRT models to upscale and forecast 10-daily R_h, NPP, and NEE simulated by *ecosys* across Alaska at 0.25° resolution. The predictor variables for the BRT models (Table 5.1) were chosen to represent the major variables that control high-latitude carbon exchanges and a realistic upscaling effort that might be attempted with current publicly available data (Table 5.2) and that are also climate forcing and *ecosys* outputs.

In order to evaluate the impact of the spatial and temporal coverage of the training dataset on machine learning model performance, we trained BRT models of each carbon flux using seven training data configurations. The first training dataset (AF) is intended to represent the current availability of EC flux tower data in Alaska. In this configuration, we selected training data according to the temporal coverage for years 2010-2019 of all

Name	Description	Units	Timescale
Air T	Daily mean air temperature	°C	Daily
SW_{in}	Daily mean incoming shortwave radiation	W m^{-2}	Daily
Soil T - 10 cm	Daily mean soil temperature at 10 cm	°C	Daily
Soil T - 2 m	Daily mean soil temperature at 2 m	°C	Daily
SSM	Surface Soil Moisture; Daily mean soil water content 0-5 cm	m^3 m^{-3}	Daily
RZSM	Root-zone Soil Moisture; Daily mean soil water content 0-100 cm	m^3 m^{-3}	Daily
SOC	Soil organic carbon in top 30 cm of soil	gC m^{-2}	Yearly
LAI	Ecosystem leaf area index	-	Daily
Sand	Soil sand content	g g^{-1}	Fixed
Silt	Soil silt content	g g^{-1}	Fixed
Tundra/Boreal	Tundra or boreal region	-	Fixed

Table 5.1: Variables used to train the machine learning model. Name, description, units, and timescale are given for each variable used to train the machine learning models.

Variable Name	Product Name	RMSE	Reference
Air T	NARR	2.32 (winter); 2.17 (summer)	[87]
SWin	NARR	58 W m^{-2}	[169]
LAI	MODIS	0.66	[178]
SSM	SMAP	0.09 m^3 m^{-3}	[180]
RZSM	SMAP	0.075 m^3 m^{-3}	[175]
SOC	Mishra et al, 2020	6.75 kg m^{-2}	[112]
Soil T - 10 cm	GIPL	1.39 °C	[47]
Soil T - 2 m	GIPL	0.74 °C	[47]
Sand/Silt/Clay	Unified North America Soil Map	-	-

Table 5.2: Gridded product availability for variables used to train the machine learning models. Publicly available gridded data products and associated uncertainty are given for variables used to train the machine learning models.

AmeriFLUX [122] sites that lie within each *ecosys* gridcell. The second training dataset (AFfc) repeats the spatial coverage of the AF dataset, but assumes full temporal coverage for years 2010-2019. The third training dataset (km15) uses the same number of gridcells (15) and temporal coverage as AFfc, but optimizes the locations of these gridcells using the predictor variables across Alaska. To do this, we used spatially-constrained k-means clustering (SKATER algorithm) [9] to identify 15 contiguous regions across Alaska and used data from the centroid gridcell for each region. Following Hoffman et al (2013) [69], we chose the centroids by minimizing the distance between the gridcells in each cluster and the cluster centroid. For each of the four remaining training datasets, we doubled the number of gridcells, choosing the locations using k-means clustering as above. We used each model to extrapolate carbon fluxes across Alaska, and excluded gridcells used in the training dataset for evaluation of model performance.

We then evaluated the ability of machine learning models to forecast carbon fluxes. The model trained on the largest dataset (km240) was used to predict Alaska R_h, NPP, and NEE throughout the 21st century. Sources of bias between the machine learning model predictions and *ecosys* simulations were evaluated using CCM. We explored the extent to which changes in atmospheric CO_2 concentration, air and soil temperature, deciduous shrub NPP dominance, and fire introduced bias into machine learning predictions of NPP, and the extent to which changes in litter C, soil temperature, deciduous shrub NPP dominance, and fire introduced bias into machine learning predictions of R_h.

5.3 Results and Discussion

Machine learning model trained with current AmeriFLUX availability and coverage misidentifies sign of present-day Alaskan net carbon exchange

Alaska is one of the most well-studied high-latitude regions, but the spatial coverage of AmeriFLUX towers is low. All 25 Alaska AmeriFLUX towers that were active between years 2010 - 2019 are located in 15 of 4319 *ecosys* 0.25° x 0.25° grid cells, and these towers are not optimally distributed to capture spatial and temporal variability. We used spatially constrained k-means clustering of simulated environmental data (Methods) to define 15 eco-regions in Alaska (Methods) and found that the AmeriFLUX towers occupy only 6 of these regions. The number of active Alaska AmeriFLUX sites increased throughout the decade from 10 sites in 2010 to 18 sites in 2019, but year-round data coverage is not available at all sites. Coverage is high during the growing season in June and July but drops to less than 50% in winter (Figure 5.1).

When evaluated using CV techniques, the performance of the machine learning models trained using existing AmeriFLUX site locations and coverage (AF) appears to be excellent. CV correlation coefficients for each carbon flux (R_h: $r = 0.95$; NPP: $r = 0.92$; NEE: $r = 0.86$) are much higher than estimated in machine learning carbon flux upscaling studies that use

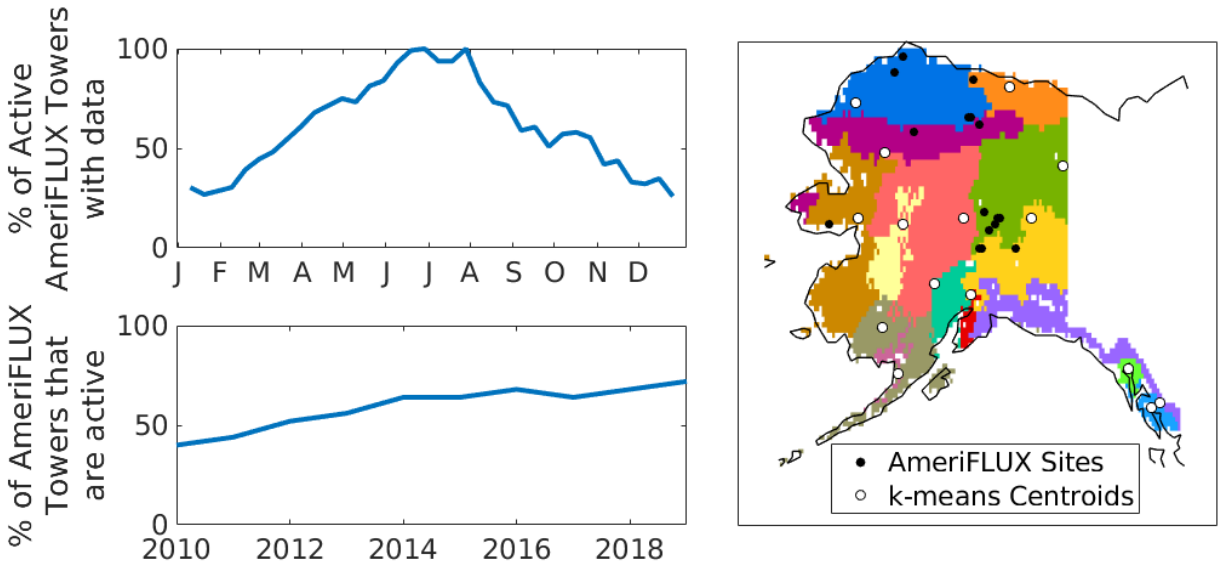

Figure 5.1: Alaskan AmeriFLUX sites exhibit uneven spatial and temporal coverage. (top left) Temporal coverage of active AmeriFLUX sites throughout the year. (bottom left) Percent of Alaskan AmeriFLUX sites that are active in each year. (right) Locations of 15 Alaskan AmeriFLUX sites with data for years 2010-2019 (black dots) and of 15 sites chosen by spatially constrained k-means clustering of simulated carbon fluxes and environmental data (open circles; SKATER algorithm). Ecoregions identified by the clustering algorithm are shown in randomly assigned colors.

real data (e.g., Natali et al (2019) [118] - NEE, non-growing season only: r = 0.75; Virkkala et al (2021) [165] - NEE: r = 0.27; Tramontana et al (2016) [160] - NEE: r = 0.68). Our machine learning model performs better than machine learning models trained on real data because the training data used in this study is idealized and *ecosys*, while complex and process-rich, is simpler than real ecosystems. When outputs from the entire modeled domain are used for validation the apparent performance of the AF model decreases significantly. Correlation coefficients for each flux are substantially lower (R_h: r = 0.75; NPP: r = 0.77; NEE: r = 0.68), and mean absolute bias is high relative to the Alaska mean for each carbon flux (Figure 5.2). This result demonstrates that CV methods can give unreliably high confidence in the performance of machine learning models used to upscale or spatially extrapolate outside of the training set.

When extrapolated across Alaska, the AF model misidentifies the sign of present-day net carbon exchange simulated by *ecosys*. Whereas Alaska is a slight sink of carbon according to *ecosys* (-19.7 gC m^2 yr^{-1}), the AF model predicts that it is a strong source of carbon (60.7 gC m^2 yr^{-1}). The AF prediction of Alaska mean R_h is close to the target value and mean absolute bias (MAB) for R_h is much lower than for NPP with this training data. These results imply that the mismatch between *ecosys* and AF predictions of Alaska NEE is primarily due to

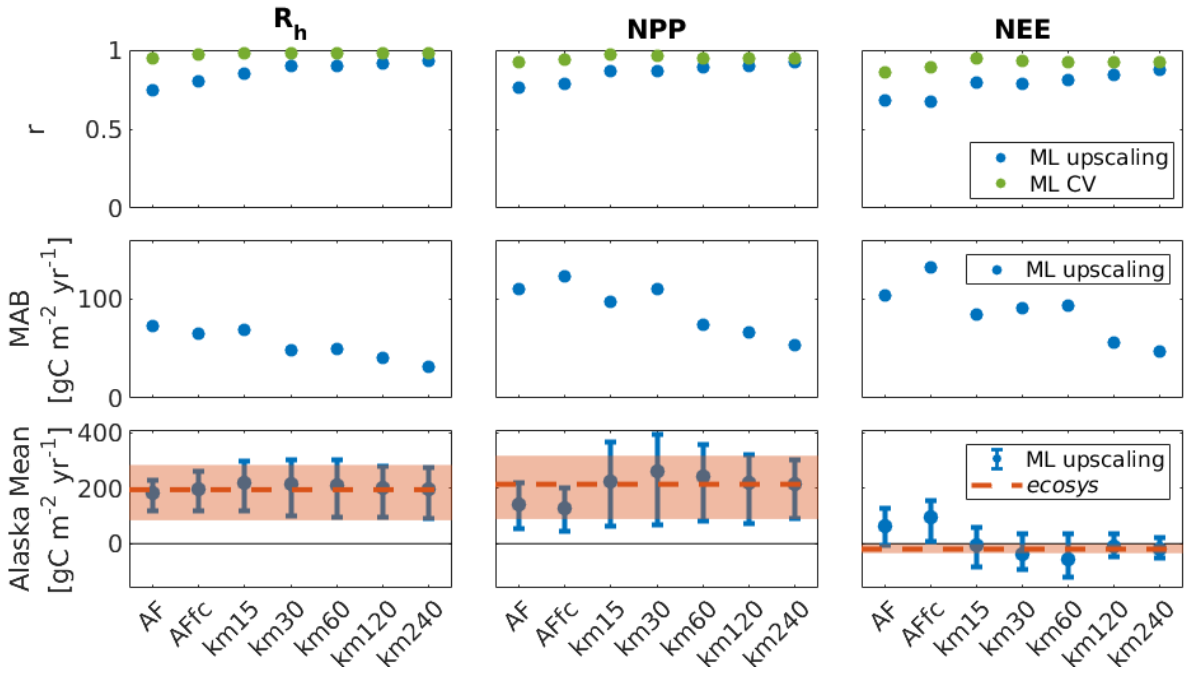

Figure 5.2: Machine learning estimation of *ecosys* carbon fluxes improves with increased spatial coverage of training data. Performance of machine learning predictions is evaluated for R_h (left column), NPP (middle column), and NEE (right column). Correlation coefficients (top row) are shown as evaluated by comparison of machine learning upscaling to *ecosys* simulations (blue) and cross-validation using the training dataset (red). Mean absolute bias (MAB) for each flux is shown in the middle row. Carbon fluxes averaged across Alaska (bottom row) are shown for machine learning upscaling (blue) and *ecosys* simulations (Target, green). The 25^{th} to 75^{th} percentile range of Alaska carbon fluxes is also shown for the machine learning upscaling (error bars) and *ecosys* simulations (shaded regions). The AF model was trained using Alaska AmeriFLUX spatial and temporal coverage for years 2010-2019, the AFfc model was trained using AmeriFLUX spatial coverage and full temporal coverage, and the kmN models were trained using N gridcells selected using spatially constrained k-means clustering.

large underestimation of plant productivity, particularly throughout southern Alaska (Figure 5.3).

Increased spatial coverage of training data improves machine learning predictions of present-day Alaska net carbon exchange

While the coverage of the AmeriFLUX network in Alaska is both spatially and temporally incomplete, we found that redistribution of sites used for training data leads to much larger

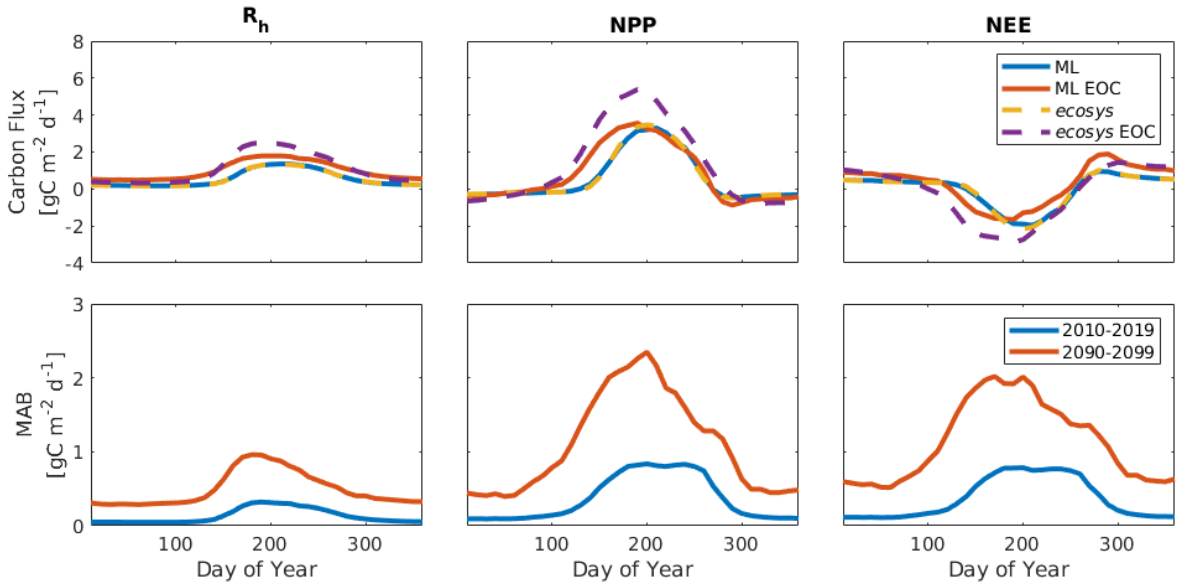

Figure 5.3: Bias of the machine learning model is largest in spring at present and at the end of the century. machine learning predictions for 2010-2019 (blue, solid), machine learning predictions for 2090-2099 (red, solid), *ecosys* simulations for 2010-2019 (yellow, dashed), and *ecosys* simulations for 2090-2099 (purple, dashed) are shown for Alaska mean R_h (top left), NPP (top middle), and NEE (top right) throughout the year. Alaska mean absolute bias in machine learning predictions for 2010-2019 (blue, solid) and 2090-2099 (red, solid) is shown for R_h (bottom left), NPP (bottom middle), and NEE (bottom right) throughout the year.

improvements in machine learning model predictions of Alaska net carbon exchange than does increased temporal coverage. Surprisingly, NPP and NEE MAB increase when the full time series for the years 2010-2019 from each AmeriFLUX site is included in the training data, and the machine learning model predicts that Alaska is an even stronger net carbon source (Figure 5.2). On the other hand, when the training data is taken from the centroid of 15 identified eco-regions, instead of from the AmeriFLUX site locations, NPP and NEE MAB decrease significantly, correlation coefficients increase, and the machine learning model correctly predicts that Alaska is a slight net sink of carbon (Figure 5.2).

Next, we added more sites to the training dataset and found additional gains in machine learning model performance. As the number of training data sites increases from 15 to 240, correlation coefficients for each flux increase and approach the values estimated by CV. While MAB does not strictly decrease for each training site doubling, MAB for the model trained with 15 sites is nearly twice as large as for the model trained with 240 sites for each flux (Figure 5.2). Additionally, the spatial distribution of bias changes as more sites are added. With fewer sites, the bias is regional, with spatially coherent patches that either

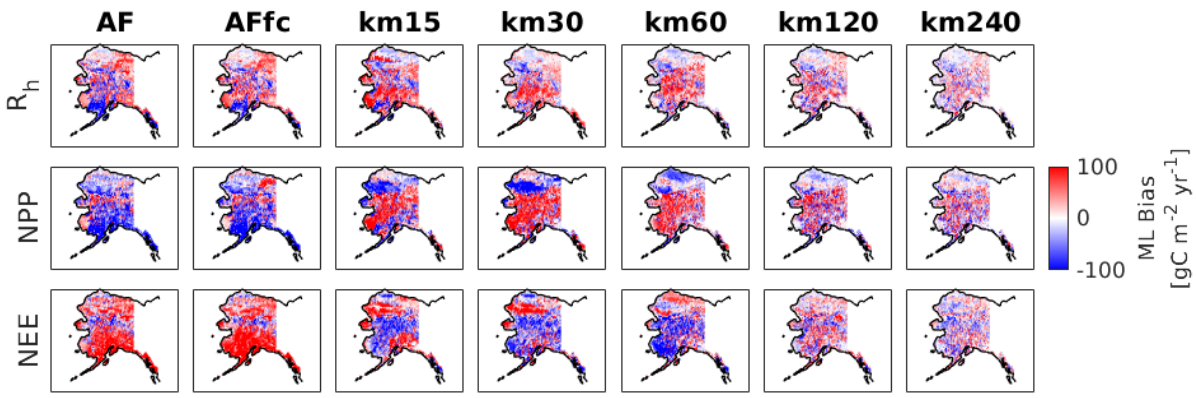

Figure 5.4: Machine learning model bias decreases and becomes less clustered with increased spatial coverage of training data. Biases in R_h (top row), NPP (middle row), and NEE (bottom row) relative to *ecosys* simulations are shown across Alaska for machine learning models trained with different *ecosys* datasets. The AF model was trained using Alaska AmeriFLUX spatial and temporal coverage for years 2010-2019, the AFfc model was trained using AmeriFLUX spatial coverage and full temporal coverage, and the kmN models were trained using N gridcells selected using spatially constrained k-means clustering.

overestimate or underestimate R_h, NPP, and NEE. As the number of sites increases, positive and negative biases decrease and become more evenly distributed across Alaska (Figure 5.4). Finally, the machine learning model distribution for each flux converges on the target distribution simulated by *ecosys* as the number of sites increases above 100 (Figure 5.2).

Machine learning model performance degrades throughout the century

In this section we investigate how the performance of the machine learning model trained on 240 sites changes throughout the 21st century. This model was trained with data from years 2010-2019, and for this period model performance is excellent. machine learning estimates of Alaska mean annual carbon fluxes agree very well with *ecosys* (R_h: 197.6 vs 194.4 gC m^2 yr^{-1}; NPP: 214.3 vs 214.0 gC m^2 yr^{-1}; NEE: -19.6 vs -19.9 gC m^2 yr^{-1}) and the model successfully captures the seasonal dynamics of each carbon flux (Figure 5.3). Further, the relative influence of each training variable for the machine learning models is consistent with expectations and processes included in *ecosys*. The models for NPP and NEE depend most strongly on air and soil temperature, radiation, and LAI, whereas the model for R_h is dependent primarily on soil temperature and LAI (Figure 5.5). EC flux tower sites are expensive, so actually installing and running 240 sites across Alaska is extremely optimistic. However, we use this ideal scenario to set an upper boundary on the ability of machine

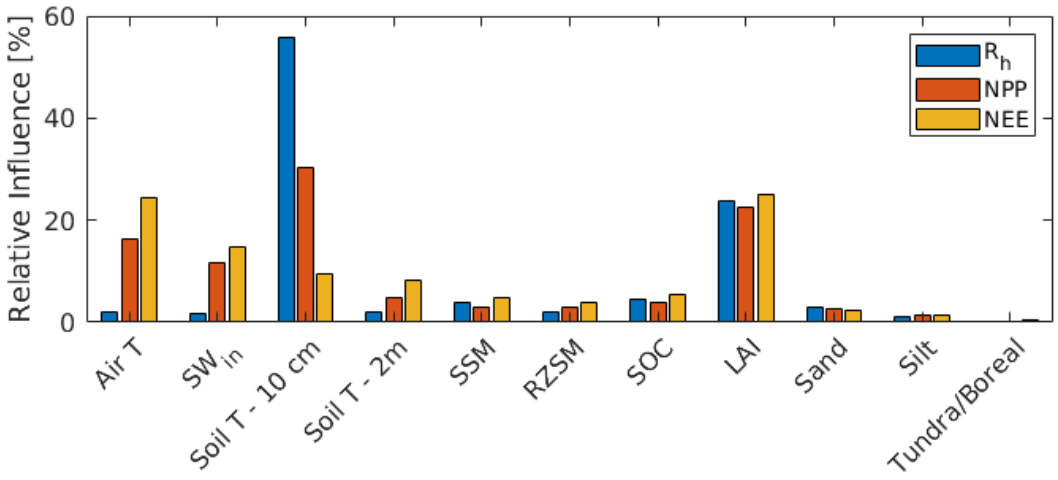

Figure 5.5: Temperature, radiation, and LAI are the most important machine learning predictor variables. Relative influence of the predictor variables (defined as percentage of trees that include a given variable) for the km240 machine learning model is shown for R_h (blue), NPP (red), and NEE (yellow). Descriptions of each variable are given in Table 5.1.

learning models trained with real-world data to forecast ecosystem responses to climate change.

We find that the machine learning model trained on the 240 sites is unable to respond to changes in ecosystem processes induced by climate change over the 21st century and that its performance degrades substantially throughout the 21st century. We observe a two-fold increase in NEE MAB, a three-fold increase in R_h MAB, and a four-fold increase in NPP MAB by year 2100 (Figure 5.6). machine learning model predictions of annual mean Alaska R_h are reasonably similar to *ecosys* through year 2040, but by the end of the century are underestimated by 104 gC m^2 yr^{-1}. The performance of the NPP machine learning model is even worse: its estimates of annual mean Alaska NPP diverge from *ecosys* by year 2030, leading to an underestimation of 204 gC m^2 at the end of the century. For both R_h and NPP, the largest increase in bias occurs during the spring (Figure 5.3). While the machine learning model is able to capture an increase in end-of-century growing season length (because it was trained on daily data), it is unable to capture increases in peak carbon fluxes at the height of the growing season (Figure 5.3).

This degradation of ML model performance with changes in climate leads to a striking discrepancy between ecosys and ML model estimates of end-of-century Alaska net C exchange. Whereas ecosys predicts that Alaska C sink strength will steadily increase throughout the century, the km240 ML model predicts that Alaska will be net C neutral from mid-century and onwards (Figure 5.7) and the AF ML model predicts that Alaska will remain a C sink until 2100 (Figure 5.8). The km240 ML model predicts that 46% of grid cells will be C

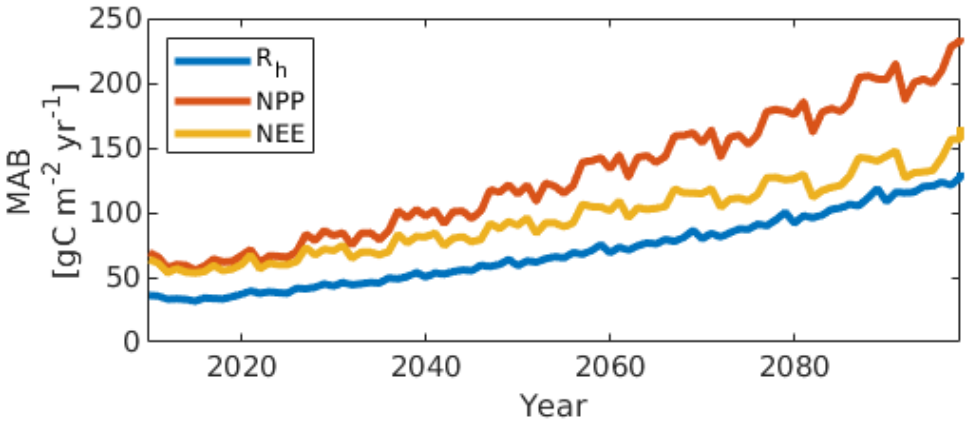

Figure 5.6: Mean absolute bias of machine learning model increases throughout the century. Alaska mean annual absolute bias (MAB) of the km240 machine learning model is shown for R_h (blue), NPP (red), and NEE (yellow) for years 2010-2099. Bias is defined as the difference between machine learning model and *ecosys* simulation for each gridcell and year.

sources in the 2090s, whereas only 7% of ecosys grid cells are identified as sources. This result demonstrates that even an ideal ML model trained and evaluated on ideal data is unable to correctly predict even the sign of net C exchange in Alaska after a century of climate change.

Machine learning model cannot predict ecosystem responses to changing CO_2 atmospheric concentrations and vegetation structure

Over the 21st century, climate change will induce large and complex changes to soil-plant-atmosphere interactions. Process models like *ecosys* are designed to simulate ecosystem responses to these changes, but machine learning models can only make predictions based on relationships contained in the training data. To quantify which 21st century changes in soil-plant-atmosphere interactions are primarily responsible for the observed degradation in machine learning model performance, we apply the convergence cross-mapping method (CCM), which uses state space reconstruction to quantify causal relationships between non-stationary and non-linear time series (Methods, Figure 5.9). Here, we explore the extent to which changes in atmospheric CO_2 concentrations, litter carbon inputs, vegetation composition, air and soil temperatures, and fire frequency generate biases in machine learning predictions of NPP and R_h.

We find that increasing atmospheric CO_2 concentrations are the primary driver of machine learning underestimation of 21st century NPP. Increases in machine learning NPP bias

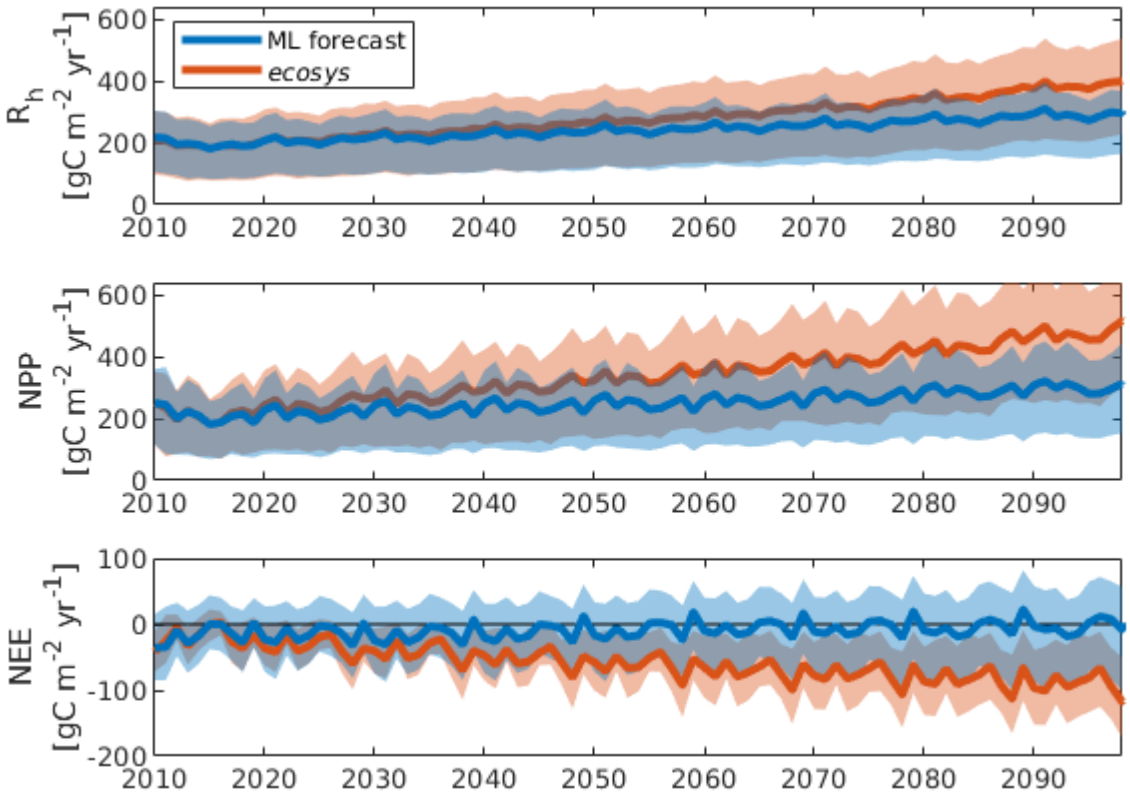

Figure 5.7: Performance of machine learning models degrades throughout the century. Alaska mean annual R_h, NPP, and NEE are shown for *ecosys* simulations (blue) and machine learning model trained on data from 240 sites (km240) for 2010-2019 (red). Shaded areas represent 25th to 75th percentile ranges.

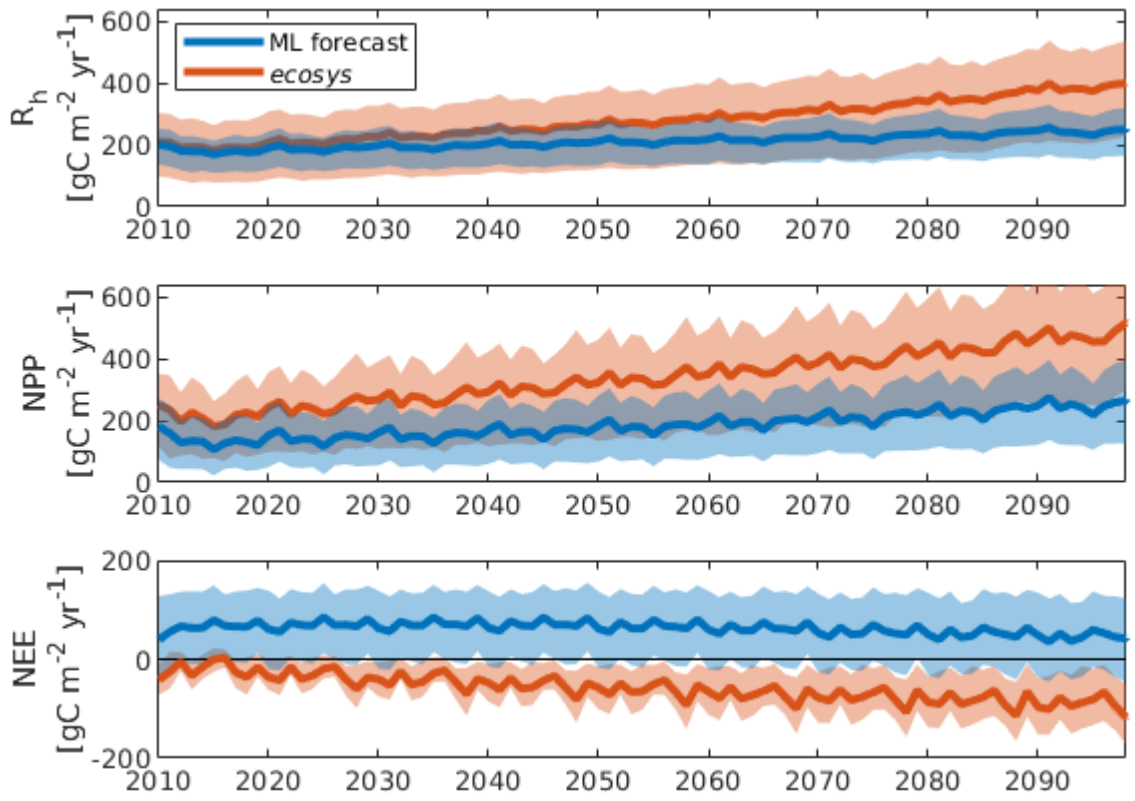

Figure 5.8: Performance of AF machine learning models remains poor throughout the century. Alaska mean annual R_h, NPP, and NEE are shown for *ecosys* simulations (blue) and machine learning model trained on data from AmeriFLUX sites and coverage (AF) for 2010-2019 (red). Shaded areas represent 25th to 75th percentile ranges.

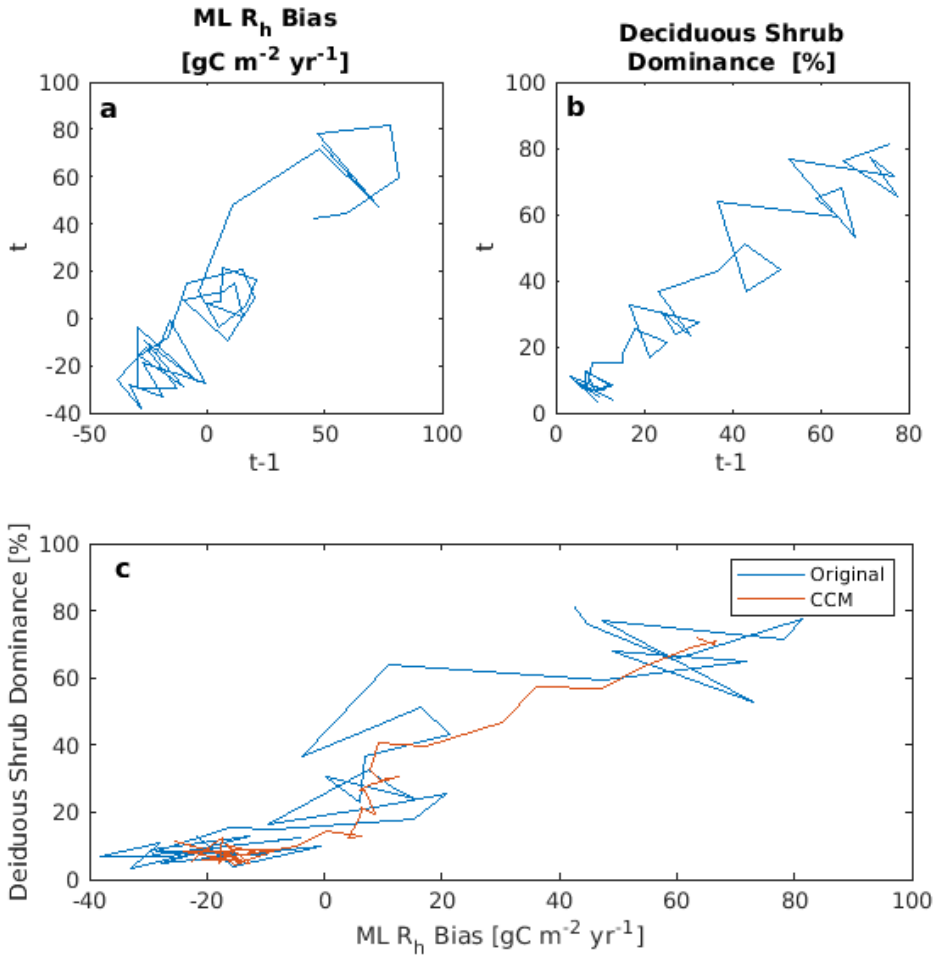

Figure 5.9: CCM example for R_h Bias and Deciduous Shrub Dominance Shadow manifolds of 1 year time lag are shown for the ML R_h Bias (**a**) and Deciduous Shrub Dominance (**b**) of the example grid cell. (**c**) Deciduous Shrub Dominance is plotted against ML R_h Bias as observed in the simulated data (blue) and reconstructed by CCM (red). The correlation coefficient of the CCM reconstruction for this example is 0.94. See [153] for more details on this method.

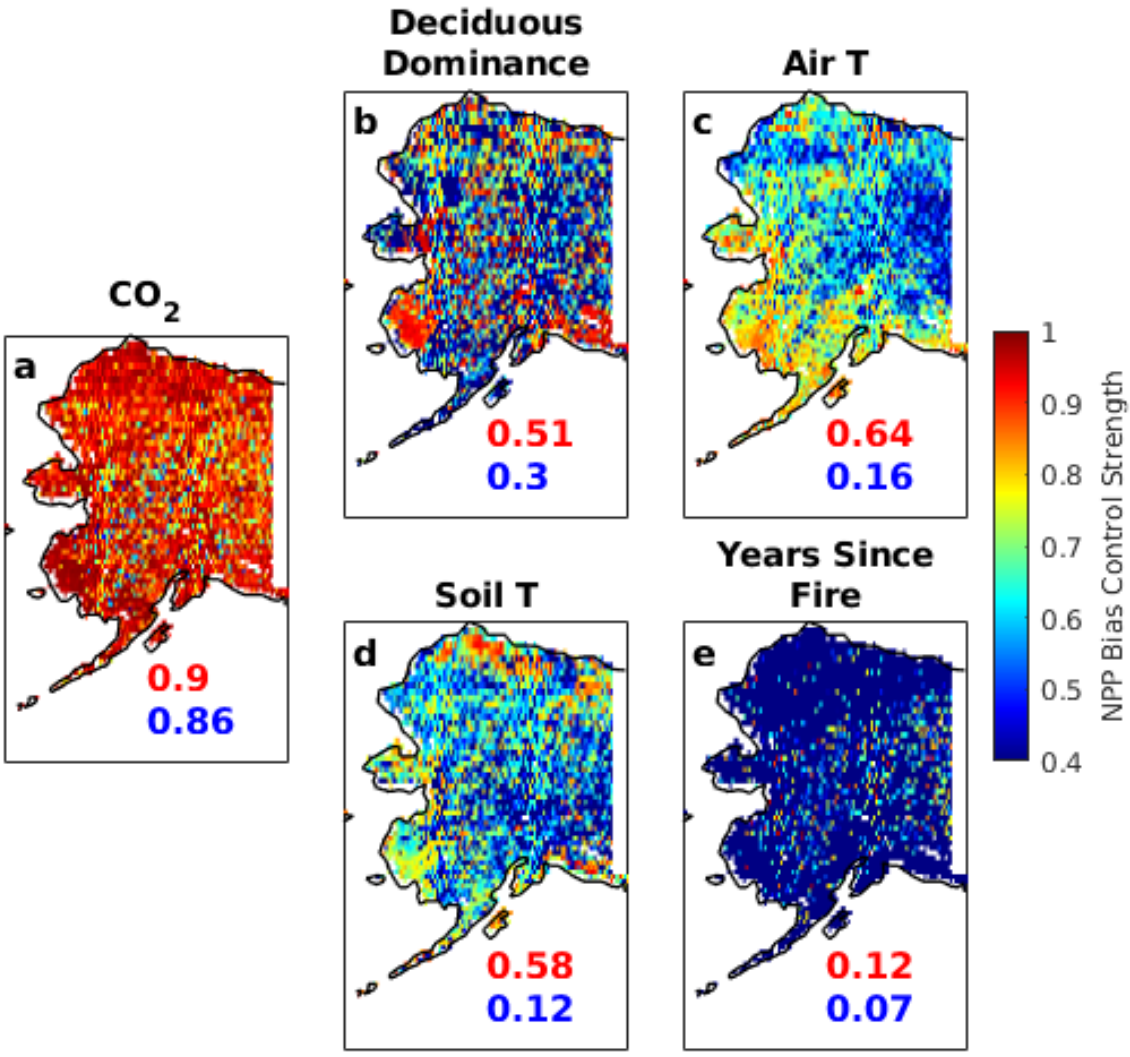

Figure 5.10: Atmospheric CO_2 concentration is the dominant control of bias in machine learning predictions of NPP throughout the century. The following drivers of machine learning model bias in NPP throughout the 21st century are identified and ranked using CCM: (**a**) atmospheric CO_2 concentration, (**b**) mean annual air temperature, (**c**) mean annual temperature in the top 25 cm of soil, (**d**) NPP dominance of deciduous PFT, (**e**) and years since the last fire. Mean bias control strength for each driver is shown in red. Drivers are ranked by the fraction of grid cells with bias control strength greater than 0.8 (shown in blue).

are strongly coupled to rising CO_2 concentrations in 86% of grid cells (Figure 5.10). Elevated CO_2 concentrations increase photosynthetic fixation rates through changes to carboxylation, photorespiration, and water and nitrogen use efficiency [3]. These processes are represented in *ecosys*, and have been tested against data from free air CO_2 enrichment experiments [57]. Because training data is generated under present day CO_2 concentrations, machine learning techniques are unable to capture changes to the relationships between environmental variables and NPP under elevated CO_2 concentrations.

Since increases in NPP generate increases in plant litter, underestimation of litter carbon is implicit in the underestimation of NPP by the machine learning model. Root and shoot litter is highly labile, so increases in litter carbon typically lead to increases in microbial respiration in field studies [2] and in the *ecosys* model [54]. Indeed, we find that litter carbon is the leading driver of machine learning underestimation of 21st century R_h, with increases in machine learning R_h bias strongly tied to increases in litter carbon in 40% of grid cells (Figure 5.11).

Shifting high-latitude vegetation composition is a secondary but strong control on both NPP and R_h machine learning biases. Increases in growth and abundance of deciduous trees and shrubs have been observed in high-latitude ecosystems in recent decades [155]. The *ecosys* model projects that this shift in vegetation composition will continue throughout the 21st century, impacting carbon cycling via changes in phenology, litter quality, nutrient acquisition and partitioning, and surface energy budgets [105, 107]. These changes drive increasing machine learning NPP (R_h) bias in 30% (34%) of grid cells. We also find that warming air and soil temperatures and increasing fire frequency are weaker drivers of machine learning bias for both NPP and R_h (Figure 5.10,5.11).

5.4 Conclusions

We performed a 'best-case' machine learning model development analysis to provide insights into approaches to spatially and temporally upscale ecosystem carbon cycle processes. We first used a well-tested mechanistic ecosystem model (*ecosys*) to simulate current and future heterotrophic respiration, net primary production, and net ecosystem carbon exchange at 0.25° resolution across Alaska. The present-day *ecosys* simulations and their climate forcing and ecosystem properties were then used to train a commonly-applied machine learning model (boosted regression tree) for these carbon fluxes. This approach represents a best-case machine learning model development scenario since (1) the process-model complexity, although substantial, is lower than real-world ecosystems and (2) the 'measurements' are free of noise, bias, and gaps.

We found that the ability of machine learning models to upscale and forecast high-latitude carbon fluxes is limited by data availability and future changes to ecosystem processes. Cross-validation methods, though widely used in machine learning applications, give poor indication of true predictive skill when training datasets do not provide adequate coverage of the prediction space. Regarding spatial scaling under current conditions, the machine

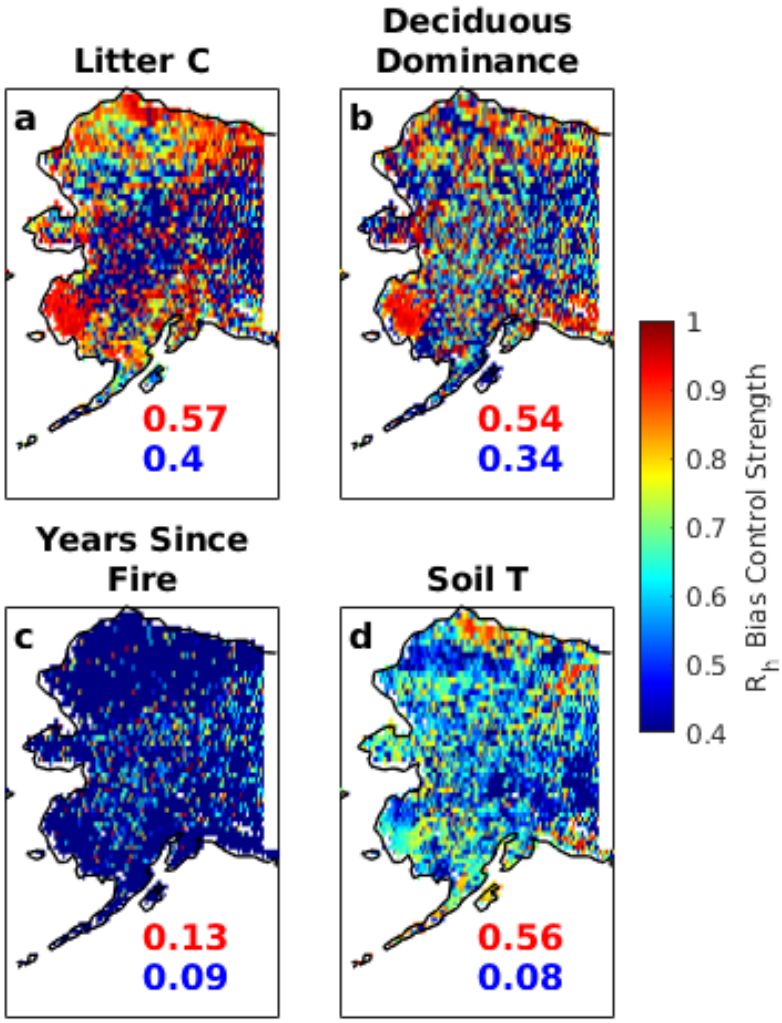

Figure 5.11: Plant litter carbon is the dominant control of bias in machine learning predictions of R_h throughout the century. The following drivers of machine learning model bias in R_h throughout the 21st century are identified and ranked using CCM: (**a**) shoot and root litter carbon, (**b**) NPP dominance of deciduous PFT, (**c**) years since the last fire, and (**d**) mean annual temperature in the top 25 cm of soil. Mean bias control strength for each driver is shown in red. Drivers are ranked by the fraction of grid cells with bias control strength greater than 0.8 (shown in blue).

learning model trained with *ecosys* simulations at existing AmeriFLUX sites predicts an opposite sign of the Alaska carbon balance. This result mirrors the current mismatch between ecosystem model and machine learning-based estimates of high-latitude carbon balances and suggests that sampling biases in generation of machine learning models, rather than incomplete ecosystem model process representation, may be at fault. We also found that increased spatial coverage of the training dataset (well beyond the current Alaska AmeriFLUX sites and beyond what is practical with current funding) significantly improves machine learning upscaling. Our results highlight the importance of intentional site selection for training data collection and that a substantial increase in optimally-located high-latitude EC flux tower site coverage is needed to produce accurate machine learning estimates of large-scale net carbon exchanges.

Regarding temporal upscaling, we found that the machine learning model has poor predictive capability at multi-decadal scales. Even using the machine learning model trained with more than ten times the EC flux tower sites that currently exist, limitations associated with out-of-sample changes in CO_2 concentrations, litter C, and vegetation structure led to large Alaska carbon flux prediction biases under 21st century climate change. Therefore, we conclude that machine learning models trained under current climate conditions should be used with caution for spatial extrapolation and not used to forecast ecosystem carbon cycle responses to climate change.

Chapter 6

Conclusions

The research presented in this thesis was conducted in order to improve understanding of the controls of carbon cycling heterogeneity and response to climate change in high-latitude ecosystems. This work relied on observations and process model representation of carbon fluxes and associated ecosystem processes. In particular, *ecosys*, a process-rich mechanistic ecosystem model that has been extensively tested at high-latitudes, was used throughout the thesis to explore the controls on high-latitude ecosystem processes.

This thesis is organized around three guiding questions: how will the large-scale controls on high-latitude carbon balance be affected by climate change, what are the primary drivers of the high level of landscape heterogeneity observed in high-latitude ecosystems, and how successfully can site-scale observations of carbon fluxes be used to predict regional carbon balances under current and future climate conditions. In this concluding section, I summarize the findings for each question and outline how future observational and modeling work can best refine and add to these findings.

6.1 Large-scale Controls on High-latitude Carbon Balance

At high-latitudes, sunlight and air temperature change dramatically with the seasons. Summer days are warm and very long. Winter days are freezing and very short. Because of this, plants and microbes are most active in summer. Recent observations and modeling studies have demonstrated that ongoing and projected climate change will increase plant productivity, microbial respiration, and growing season lengths at high-latitude, potentially shifting the magnitude and sign of the high-latitude carbon balance. In the third chapter of this thesis, *ecosys* was used to explore how climate warming will impact large-scale controls on high-latitude carbon balance and shift carbon cycle seasonality in Alaska throughout the 21st century.

We found that seasonal changes in plant productivity simulated by *ecosys* throughout the coming century could be explained using a simple model of the limitations to photosynthesis

imposed by air temperature and light availability. Under current climate conditions, fall and winter plant activity are limited by both cold temperatures and low light, whereas spring plant activity is limited only by cold temperatures. Under future climate conditions, temperatures will warm by 7 °C throughout the year, whereas light-availability will not change. Therefore, we can predict that plant carbon fixation will increase dramatically in spring, which will be both light and warm at the end of the century. The fall, in contrast, will be warm but dark, so no increase in photosynthesis is expected. These predictions were borne out by the *ecosys* simulations. Simulated spring net carbon uptake increased from 19 to 144 gC m^{-2} $season^{-1}$ and fall and winter net carbon loss increased from 76 to 163 gC m^{-2} $season^{-1}$ by the end of the century across Alaska. These changes represent an important shift in the seasonality of the high-latitude carbon cycle. High-latitude plant and microbial activity is largely concentrated in the summer months under current climate conditions, but by the end of the century, both spring net carbon uptake and fall plus winter net carbon loss will be larger than summer net carbon uptake.

Taken together, the results outlined above suggest that the high-latitudes will continue to accumulate carbon throughout this century. Spring will become so amenable to plant productivity under future climates that increased net carbon uptake during those months will overpower the increased fall and winter carbon losses. This conclusion, however, is contingent on the ability of plants to acquire sufficient water and nutrients throughout the coming century to support these increases in carbon fixation.

In our results, there was little change in summer water stress, and summer net carbon uptake increased slightly throughout the century. Significant increases in water stress, particularly in the boreal forest, could introduce drastic changes in the summer carbon cycle. While there is general consensus that arctic precipitation will increase with climate change, the magnitude of this shift is uncertain because regional precipitation patterns are challenging to simulate in climate models. Further, changes to hydrology associated with permafrost thaw at high-latitudes are still poorly understood.

We also showed that increased carbon fixation is tied to large increases in plant nitrogen uptake throughout the coming century. In particular, our results suggest that plants rely on nitrogen taken up during fall and winter to support the large increase in spring carbon fixation. A number of recent field studies have demonstrated that non-growing season nitrogen uptake is an important component of the high-latitude nitrogen cycle. However, the controls that affect the balance between plant nitrogen uptake and soil nitrogen losses from leaching during the non-growing season are still highly uncertain, and process understanding of plant allocation and utilization of nitrogen acquired during these months is limited. Additionally, the rates of nitrogen fixation, an important source of biologically available nitrogen, are very challenging to measure and these rates are highly uncertain under both current and future climate conditions. An important next step in this research would be to characterize the sensitivity of the results presented in this section to uncertainties in future plant water and nitrogen availability.

Methane production, while not a focus of this thesis, is a very important topic for the high-latitude carbon cycle. Methane is a much more potent greenhouse gas than CO_2, and

recent observational studies [111, 172] estimate that present-day methane emissions across Alaska have a similar sustained global warming potential ($SGWP_{100}$) as the net CO_2 uptake of the region as estimated by *ecosys*. As we showed in Chapter 4 (and has been documented extensively in the literature, e.g., [159, 40]), the highest rates of methane production are found in saturated soils, as can be found in wetland sites. However, changes in high-latitude wetland extent caused by climate change are very challenging to predict, leading to large uncertainties in estimates of future high-latitude methane budgets. Continued efforts to characterize current high-latitude methane emissions and improve predictions of future changes to methane production are vital.

6.2 Drivers of watershed-scale variability in ecosystem processes

At high-latitudes, properties such as soil temperatures, soil wetness, snowpack, and vegetation cover vary considerably across a landscape. The scale of this variation can be as small as 1-10 m (for example, a patch of tall shrubs with a deep snowpack and warm soil temperatures can transition abruptly to low-lying tundra vegetation with shallow snowpack and cold soil temperatures). The resolution of terrestrial ecosystem models that are used to predict global responses to climate change, however, is much coarser ($\sim$100-300 km). The mismatch between the scales of landscape variation and the scales of models may introduce bias into predictions of ecosystem processes. In order to better understand the causes and implications of landscape variability, we explored the response of *ecosys* to variation in soil properties, boundary conditions, and weather forcing in the fourth chapter of this thesis.

In this chapter, we showed that landscape heterogeneity strongly impacts soil temperatures and vegetation composition. Snow depth, O-horizon thickness, and near-surface water content, which vary at scales of O(m), control the soil thermal regime more than an air temperature gradient corresponding to a 140 km north-south distance. High shrub productivity is simulated only in talik (perennially unfrozen) soils with high nitrogen availability. Through these effects on plant and permafrost dynamics, landscape heterogeneity impacts ecosystem productivity. Simulations with near-surface taliks have higher microbial respiration (by 78.0 gC m^{-2} yr^{-1}) and higher net primary productivity (by 104.9 gC m^{-2} yr^{-1}) compared to runs with near-surface permafrost, and simulations with high shrub productivity have outlying values of net carbon uptake. We explored the prediction uncertainty associated with ignoring observed landscape heterogeneity, and found that watershed net carbon uptake is three times larger when heterogeneity is accounted for.

Our results highlight the complexity inherent in high-latitude ecosystems. Even if the large-scale controls on high-latitude carbon cycling are well represented, the results from this chapter demonstrate that missing representation of subgrid heterogeneity in ecosystem models leads to biased predictions of the high-latitude carbon budget. The analysis presented in this section is centered on a watershed characterized by coastal climate, warm

discontinuous permafrost, and tundra vegetation but the controls on watershed-scale variability are expected to vary dramatically throughout the high-latitudes. Repetition of this sensitivity analysis at different high-latitude sites characterized by different vegetation types, permafrost temperatures, and weather conditions would provide valuable insights into high-latitude ecosystem dynamics. An improved understanding of regional variation in the controls on watershed-scale heterogeneity would help to guide field measurements and inform which types of sub-grid heterogeneity are most important for inclusion in process models.

Water introduces considerable complexity into high-latitude ecosystems. The important thermal characteristics of water are easily measured - 334,000 J of energy are required to thaw 1 kg of ice, and the thermal diffusivity of ice is close to ten times larger than the thermal diffusivity of water - but freeze-thaw processes in real systems create non-linearities that complicate efforts to predict how soil thermal regimes will respond to changes in soil saturation in different climatic conditions. For instance, in this chapter we showed that while thick organic horizons are often assumed to protect permafrost, in the studied watershed the impact of the organic horizon on the soil thermal regime varied strongly with its water content. Additionally, water movement, which is complicated enough without considering freeze-thaw processes, both impacts and is impacted by permafrost and talik dynamics. By demonstrating that soil water content, soil temperatures, and plant and microbial dynamics are so strongly coupled in these ecosystems, the results of this chapter emphasize the importance of improved understanding and model representation of high-latitude hydrology.

6.3 Upscaling and forecasting carbon fluxes using site observations

Even though the high-latitude carbon cycle is a key feedback to the global climate system there is currently disagreement over whether the region is a source or sink of carbon. While there is general consensus among process models that the high-latitudes are currently a carbon sink, a number of recent high-profile observation-based estimates (e.g., Natali et al (2019) and Commane et al (2017)) have suggested that the high-latitudes are currently a source of carbon. This disagreement stems from high spatial and temporal variability, a complex and interacting set of environmental drivers and feedbacks, incomplete process-representation in ecosystem models, and limited data due to harsh environmental conditions and remoteness of northern lands, particularly during the winter months.

Natali et al (2019) and Commane et al (2017) use observations of high-latitude fall and winter carbon fluxes to argue that incorrect process representation of winter soil biogeochemistry in ecosystem models leads to incorrect estimates of net annual carbon balance. Indeed, most process models cited in Natali et al (2019) estimated much lower winter carbon fluxes than the observationally upscaled product. But, as we showed in Chapter 3, fall and winter processes are not independent of spring and summer processes, and a mismatch between model and observation products in the fall and winter could be complemented by a parallel

mismatch during the spring and summer. Because *ecosys* has a better representation of soil biogeochemistry and nitrogen cycling than most ecosystem models, it is able to reproduce the large fall and winter losses predicted by these studies across Alaska. Nevertheless, winter mineralization and plant nutrient uptake associated with these carbon losses supports increased growing season carbon uptake, and the model predicts that the region is a net carbon sink even with such large winter carbon losses.

Recent advances in big data analytics and computing power have popularized the use of machine learning algorithms to upscale site measurements of ecosystem processes, and in some cases forecast the response of these processes to climate change. Due to limited data availability, however, machine learning model predictions of these processes are almost never validated with independent datasets. In Chapter 5, we used *ecosys* to train machine-learning models and then evaluate their ability to upscale and forecast high-latitude carbon fluxes under current and future climate. This approach allowed us to evaluate the performance of machine learning models under a best-case scenario, with a simpler-than-reality model and noise-free data.

Cross-validation, in which the entire dataset is iteratively split into training and testing sets, is the most commonly applied technique to evaluate machine learning model performance when data is limited. When we trained a machine learning model mimicking the existing data availability from the AmeriFLUX network of carbon flux measurements, cross-validation metrics pointed to excellent model performance. However, when we evaluated the machine learning model on data from the rest of the model grid cells not used in the training dataset (truly out-of-sample data), we found that actual predictive skill of the model was very poor, with high bias and low correlation to the target dataset. This result points to strong deficiencies in cross-validation techniques, particularly when the training datasets do not provide adequate coverage of the prediction space. Development of a technique to evaluate confidence in cross-validation estimates of model performance using the overlap between training and prediction spaces is important future work. Until such metrics have been developed, cross-validation evaluations of machine learning models should be treated with skepticism.

Estimates of regional ecosystem processes that are based on upscaled site observations are usually more highly valued than estimates produced by process models, even if those observations are scarce, and are often even used to evaluate process model performance. The upscaling process itself is full of uncertainties, and does not necessarily provide trustworthy estimates of regional processes. For example, *ecosys* estimates that Alaska is currently a net sink of carbon, but the machine learning model trained using existing data availability predicts that Alaska is a strong source of carbon. This model was trained using noise- and error-free outputs from *ecosys*, and simply got the regional carbon balance wrong. This result emphasizes the fact that sampling biases in upscaling estimates can be as problematic as incomplete process representation in ecosystem models.

A priority for the high-latitude earth and environmental science community should be a discussion of the best way to focus future efforts to improve estimates of high-latitude carbon balance. The simplest way to improve upscaling estimates is to collect more data. As

we showed in Chapter 5, machine learning model performance improves substantially with increased spatial coverage, and the bias of carbon flux estimates was halved when 240 sites across Alaska were used instead of 15. However, obtaining reasonably confident estimates of regional carbon balance using upscaling techniques would require an enormous, and likely infeasible, investment in deployment and maintenance of eddy-covariance towers. Even a moderate increase in eddy covariance tower coverage, however, would be very useful for validation of process model predictions. Atmospheric inversion is a different technique that uses measurements of atmospheric CO_2 concentrations to estimate land surface carbon fluxes, but these methods rely on atmospheric transport models that have their own associated uncertainties and data limitations. Future efforts should also prioritize more robust uncertainty characterization in reported estimates of carbon balance, regardless of the method used to produce them.

Finally, this thesis demonstrates that mechanistic, process-based ecosystem models are the best tool available for predicting carbon fluxes under future climate conditions. There has been a recent upsurge in the use of machine learning models to forecast the response of ecosystem processes to climate change. However, there have been no attempts to test the capability of machine learning models to make these types of predictions. In Chapter 5, we show that machine learning model performance degrades significantly throughout the century. Climate induced changes in atmospheric CO_2 concentrations, litter carbon inputs, and vegetation composition change the response of ecosystem carbon fluxes to environmental variables in ways that cannot be inferred from ecosystem processes in current climate conditions by machine learning models. This result is clear evidence that predictions of terrestrial ecosystem response to climate change can best be improved by prioritizing the development and application of process models.

Bibliography

[1] Hassan Abbasian et al. "Modeling terrestrial net ecosystem exchange using machine learning techniques based on flux tower measurements". In: *Ecological Modelling* 466 (2022), p. 109901.

[2] Magdalene Adamczyk et al. "Strong shifts in microbial community structure are associated with increased litter input rather than temperature in High Arctic soils". In: *Soil Biology and Biochemistry* 151 (2020), p. 108054.

[3] Elizabeth A Ainsworth and Alistair Rogers. "The response of photosynthesis and stomatal conductance to rising [CO2]: mechanisms and environmental interactions". In: *Plant, cell & environment* 30.3 (2007), pp. 258–270.

[4] AM Arft et al. "Responses of tundra plants to experimental warming: meta-analysis of the international tundra experiment". In: *Ecological monographs* 69.4 (1999), pp. 491–511.

[5] Martin Arjovsky et al. "Invariant risk minimization". In: *arXiv preprint arXiv:1907.02893* (2019).

[6] Kyle A Arndt et al. "Arctic greening associated with lengthening growing seasons in Northern Alaska". In: *Environmental Research Letters* 14.12 (2019), p. 125018.

[7] Bhavna Arora et al. "Evaluating temporal controls on greenhouse gas (GHG) fluxes in an Arctic tundra environment: An entropy-based approach". In: *Science of the total environment* 649 (2019), pp. 284–299.

[8] VK Arora and GJ Boer. "Terrestrial ecosystems response to future changes in climate and atmospheric CO 2 concentration". In: *Biogeosciences* 11.15 (2014), pp. 4157–4171.

[9] Renato M Assunção et al. "Efficient regionalization techniques for socio-economic geographical units using minimum spanning trees". In: *International Journal of Geographical Information Science* 20.7 (2006), pp. 797–811.

[10] Jean-Francois Bastin et al. "The global tree restoration potential". In: *Science* 365.6448 (2019), pp. 76–79.

[11] Michael S Becker, T Jonathan Davies, and Wayne H Pollard. "Ground ice melt in the high Arctic leads to greater ecological heterogeneity". In: *Journal of Ecology* 104.1 (2016), pp. 114–124.

[12] EF Belshe et al. "Incorporating spatial heterogeneity created by permafrost thaw into a landscape carbon estimate". In: *Journal of Geophysical Research: Biogeosciences* 117.G1 (2012).

[13] WD Billings. "Arctic and alpine vegetations: similarities, differences, and susceptibility to disturbance". In: *BioScience* 23.12 (1973), pp. 697–704.

[14] Richard Bintanja and Olivier Andry. "Towards a rain-dominated Arctic". In: *Nature Climate Change* 7.4 (2017), pp. 263–267.

[15] Anne D Bjorkman et al. "Status and trends in Arctic vegetation: Evidence from experimental warming and long-term monitoring". In: *Ambio* 49.3 (2020), pp. 678–692.

[16] Nicholas J Bouskill et al. "Alaskan carbon-climate feedbacks will be weaker than inferred from short-term experiments". In: *Nature communications* 11.1 (2020), pp. 1–12.

[17] Jason E Box et al. "Key indicators of Arctic climate change: 1971–2017". In: *Environmental Research Letters* 14.4 (2019), p. 045010.

[18] Wolfgang Buermann et al. "Earlier springs decrease peak summer productivity in North American boreal forests". In: *Environmental Research Letters* 8.2 (2013), p. 024027.

[19] Eleanor J Burke, Yu Zhang, and Gerhard Krinner. "Evaluating permafrost physics in the Coupled Model Intercomparison Project 6 (CMIP6) models and their sensitivity to climate change". In: *The Cryosphere* 14.9 (2020), pp. 3155–3174.

[20] Bob Busey et al. *Surface Meteorology at Teller Site Stations, Seward Peninsula, Alaska, Ongoing from 2016.* Tech. rep. Next Generation Ecosystem Experiments Arctic Data Collection, Oak Ridge National Laboratory, U.S. Department of Energy, Oak Ridge, Tennessee, USA., 2017. URL: `https://doi.org/10.5440/1437633`.

[21] William L Cable, Vladimir E Romanovsky, and M Torre Jorgenson. "Scaling-up permafrost thermal measurements in western Alaska using an ecotype approach". In: *The Cryosphere* 10.5 (2016), pp. 2517–2532.

[22] Francesca Campolongo, Jessica Cariboni, and Andrea Saltelli. "An effective screening design for sensitivity analysis of large models". In: *Environmental modelling & software* 22.10 (2007), pp. 1509–1518.

[23] Kuang-Yu Chang et al. "Large carbon cycle sensitivities to climate across a permafrost thaw gradient in subarctic Sweden". In: *The Cryosphere* 13.2 (2019), pp. 647–663.

[24] Kuang-Yu Chang et al. "Methane production pathway regulated proximally by substrate availability and distally by temperature in a high-latitude mire complex". In: *Journal of Geophysical Research: Biogeosciences* 124.10 (2019), pp. 3057–3074.

[25] Rachel Y-W Chang et al. "Methane emissions from Alaska in 2012 from CARVE airborne observations". In: *Proceedings of the National Academy of Sciences* 111.47 (2014), pp. 16694–16699.

[26] FS Chapin and A Bloom. "Phosphate absorption: adaptation of tundra graminoids to a low temperature, low phosphorus environment". In: *Oikos* (1976), pp. 111–121.

[27] F Stuart Chapin III et al. "Plant functional types as predictors of transient responses of arctic vegetation to global change". In: *Journal of vegetation Science* 7.3 (1996), pp. 347–358.

[28] Hans W Chen et al. "Characterization of regional-scale CO2 transport uncertainties in an ensemble with flow-dependent transport errors". In: *Geophysical Research Letters* 46.7 (2019), pp. 4049–4058.

[29] Róisın Commane et al. "Carbon dioxide sources from Alaska driven by increasing early winter respiration from Arctic tundra". In: *Proceedings of the National Academy of Sciences* 114.21 (2017), pp. 5361–5366.

[30] Andrew Crane-Droesch. "Machine learning methods for crop yield prediction and climate change impact assessment in agriculture". In: *Environmental Research Letters* 13.11 (2018), p. 114003.

[31] Alexander D'Amour et al. "Underspecification presents challenges for credibility in modern machine learning". In: *arXiv preprint arXiv:2011.03395* (2020).

[32] Baptiste Dafflon et al. *A Distributed Temperature Profiling System for Vertically and Laterally Dense Acquisition of Soil and Snow Temperature: Supporting Data.* Tech. rep. Next Generation Ecosystem Experiments Arctic Data Collection, Oak Ridge National Laboratory, U.S. Department of Energy, Oak Ridge, Tennessee, USA., 2021. URL: `https://doi.org/10.5440/181936`.

[33] Taraka Davies-Barnard et al. "Nitrogen cycling in CMIP6 land surface models: progress and limitations". In: *Biogeosciences* 17.20 (2020), pp. 5129–5148.

[34] MV Debolskiy et al. "Modeling present and future permafrost distribution at the Seward Peninsula, Alaska". In: *Journal of Geophysical Research: Earth Surface* 125.8 (2020), e2019JF005355.

[35] FJ Dentener. "Global maps of atmospheric nitrogen deposition, 1860, 1993, and 2050". In: *ORNL DAAC* (2006).

[36] Dimitre D Dimitrov et al. "Modeling the subsurface hydrology of Mer Bleue Bog". In: *Soil Science Society of America Journal* 74.2 (2010), pp. 680–694.

[37] Emiliano Dıaz et al. "Inferring causal relations from observational long-term carbon and water fluxes records". In: *Scientific Reports* 12.1 (2022), pp. 1–12.

[38] Randall J Donohue et al. "Impact of CO2 fertilization on maximum foliage cover across the globe's warm, arid environments". In: *Geophysical Research Letters* 40.12 (2013), pp. 3031–3035.

[39] Ran Du et al. "The role of peat on permafrost thaw based on field observations". In: *CATENA* 208 (2022), p. 105772.

[40] Clayton Drew Elder et al. "Characterizing methane emission hotspots from thawing permafrost". In: *Global Biogeochemical Cycles* 35.12 (2021), e2020GB006922.

[41] Jane Elith, John R Leathwick, and Trevor Hastie. "A working guide to boosted regression trees". In: *Journal of animal ecology* 77.4 (2008), pp. 802–813.

[42] Jessica G Ernakovich et al. "Predicted responses of arctic and alpine ecosystems to altered seasonality under climate change". In: *Global Change Biology* 20.10 (2014), pp. 3256–3269.

[43] Graham D Farquhar, S von von Caemmerer, and Joseph A Berry. "A biochemical model of photosynthetic CO2 assimilation in leaves of C3 species". In: *planta* 149.1 (1980), pp. 78–90.

[44] Rebecca A Finger et al. "Effects of permafrost thaw on nitrogen availability and plant–soil interactions in a boreal Alaskan lowland". In: *Journal of Ecology* 104.6 (2016), pp. 1542–1554.

[45] Gerald V Frost et al. "Seasonal and long-term changes to active-layer temperatures after tall shrubland expansion and succession in Arctic tundra". In: *Ecosystems* 21.3 (2018), pp. 507–520.

[46] Angela V Gallego-Sala et al. "Latitudinal limits to the predicted increase of the peatland carbon sink with warming". In: *Nature climate change* 8.10 (2018), pp. 907–913.

[47] A Garnello et al. "Projecting Permafrost Thaw of Sub-Arctic Tundra With a Thermodynamic Model Calibrated to Site Measurements". In: *Journal of Geophysical Research: Biogeosciences* 126.6 (2021), e2020JG006218.

[48] Robert Geirhos et al. "Shortcut learning in deep neural networks". In: *Nature Machine Intelligence* 2.11 (2020), pp. 665–673.

[49] Ronald Gelaro et al. "The modern-era retrospective analysis for research and applications, version 2 (MERRA-2)". In: *Journal of climate* 30.14 (2017), pp. 5419–5454.

[50] RF Grant. "Modeling carbon and nitrogen dynamics for soil management". In: (2001).

[51] RF Grant. "Simulation in ecosys of root growth response to contrasting soil water and nitrogen". In: *Ecological Modelling* 107.2-3 (1998), pp. 237–264.

[52] RF Grant. "Simulation of methanogenesis in the mathematical model ecosys". In: *Soil Biology and Biochemistry* 30.7 (1998), pp. 883–896.

[53] RF Grant. "Simulation of methanotrophy in the mathematical model ecosys". In: *Soil Biology and Biochemistry* 31.2 (1999), pp. 287–297.

[54] RF Grant, Miles Dyck, and Dick Puurveen. "Nitrogen and phosphorus control carbon sequestration in agricultural ecosystems: modelling carbon, nitrogen, and phosphorus balances at the Breton Plots with ecosys under historical and future climates". In: *Canadian Journal of Soil Science* 100.4 (2020), pp. 408–429.

[55] RF Grant, ER Humphreys, and PM Lafleur. "Ecosystem CO2 and CH4 exchange in a mixed tundra and a fen within a hydrologically diverse Arctic landscape: 1. Modeling versus measurements". In: *Journal of Geophysical Research: Biogeosciences* 120.7 (2015), pp. 1366–1387.

[56] RF Grant, ZA Mekonnen, and WJ Riley. "Modeling climate change impacts on an Arctic polygonal tundra: 1. Rates of permafrost thaw depend on changes in vegetation and drainage". In: *Journal of Geophysical Research: Biogeosciences* 124.5 (2019), pp. 1308–1322.

[57] RF Grant et al. "Crop water relations under different CO2 and irrigation: testing of ecosys with the free air CO2 enrichment (FACE) experiment". In: *Agricultural and Forest Meteorology* 95.1 (1999), pp. 27–51.

[58] RF Grant et al. "Ecological controls on net ecosystem productivity of a mesic arctic tundra under current and future climates". In: *Journal of Geophysical Research: Biogeosciences* 116.G1 (2011).

[59] RF Grant et al. "Interannual variation in net ecosystem productivity of Canadian forests as affected by regional weather patterns–A Fluxnet-Canada synthesis". In: *Agricultural and Forest Meteorology* 149.11 (2009), pp. 2022–2039.

[60] RF Grant et al. "Mathematical modelling of arctic polygonal tundra with ecosys: 1. Microtopography determines how active layer depths respond to changes in temperature and precipitation". In: *Journal of Geophysical Research: Biogeosciences* 122.12 (2017), pp. 3161–3173.

[61] RF Grant et al. "Mathematical modelling of Arctic polygonal tundra with Ecosys: 2. Microtopography determines how CO2 and CH4 exchange responds to changes in temperature and precipitation". In: *Journal of Geophysical Research: Biogeosciences* 122.12 (2017), pp. 3174–3187.

[62] RF Grant et al. "Modeling climate change impacts on an Arctic polygonal tundra: 2. Changes in CO2 and CH4 exchange depend on rates of permafrost thaw as affected by changes in vegetation and drainage". In: *Journal of Geophysical Research: Biogeosciences* 124.5 (2019), pp. 1323–1341.

[63] RF Grant et al. "Net ecosystem productivity of temperate and boreal forests after clearcutting—a Fluxnet-Canada measurement and modelling synthesis". In: *Tellus B: Chemical and Physical Meteorology* 62.5 (2010), pp. 475–496.

[64] Robert F Grant and Larry B Flanagan. "Modeling stomatal and nonstomatal effects of water deficits on CO2 fixation in a semiarid grassland". In: *Journal of Geophysical Research: Biogeosciences* 112.G3 (2007).

[65] HD Graven et al. "Enhanced seasonal exchange of CO2 by northern ecosystems since 1960". In: *Science* 341.6150 (2013), pp. 1085–1089.

[66] Brandon Greenwell, Bradley Boehmke, and Jay Cunningham. *G B M 2020 gbm: Generalized Boosted Regression Models*. Tech. rep. R Package, 2017. URL: `https://CRAN.R-project.org/package=gbm`.

[67] Melanie A Harsch et al. "Are treelines advancing? A global meta-analysis of treeline response to climate warming". In: *Ecology letters* 12.10 (2009), pp. 1040–1049.

[68] Jeffrey A Hicke et al. "Satellite-derived increases in net primary productivity across North America, 1982–1998". In: *Geophysical Research Letters* 29.10 (2002), pp. 69–1.

[69] Forrest M Hoffman et al. "Representativeness-based sampling network design for the State of Alaska". In: *Landscape Ecology* 28.8 (2013), pp. 1567–1586.

[70] Marika M Holland and Laura Landrum. "Factors affecting projected Arctic surface shortwave heating and albedo change in coupled climate models". In: *Philosophical Transactions of the Royal Society A: Mathematical, Physical and Engineering Sciences* 373.2045 (2015), p. 20140162.

[71] G Hugelius et al. "Short communication: a new dataset for estimating organic carbon storage to 3 m depth in soils of the northern circumpolar permafrost region". In: *Earth System Science Data Discussions* 6 (2013), pp. 73–93.

[72] IPCC. *Climate Change 2013: The Physical Science Basis*. Ed. by T.F. Stocker et al. Contribution of Working Group I to the Fifth Assessment Report of the Intergovernmental Panel on Climate Change. Cambridge University Press (In Press), 2013.

[73] IPCC. *Climate Change 2021: The Physical Science Basis*. Ed. by V. Masson-Delmotte et al. Contribution of Working Group I to the Sixth Assessment Report of the Intergovernmental Panel on Climate Change. Cambridge University Press (In Press), 2021. URL: `https://www.ipcc.ch/report/ar6/wg1/downloads/report/IPCC_AR6_WGI_Full_Report.pdf`.

[74] Akihiko Ito, Kazuya Nishina, and Hibiki M Noda. "Impacts of future climate change on the carbon budget of northern high-latitude terrestrial ecosystems: an analysis using ISI-MIP data". In: *Polar Science* 10.3 (2016), pp. 346–355.

[75] Andrew R Jacobson et al. "CarbonTracker CT2019". In: *NOAA Earth System Research Laboratory, Global Monitoring Division: Boulder, CO, USA* (2020).

[76] Elchin E Jafarov et al. "Modeling the role of preferential snow accumulation in through talik development and hillslope groundwater flow in a transitional permafrost landscape". In: *Environmental Research Letters* 13.10 (2018), p. 105006.

[77] Hans Jenny. "Derivation of state factor equations of soils and ecosystems". In: *Soil Science Society of America Journal* 25.5 (1961), pp. 385–388.

[78] Kristofer D Johnson et al. "Permafrost and organic layer interactions over a climate gradient in a discontinuous permafrost zone". In: *Environmental Research Letters* 8.3 (2013), p. 035028.

[79] M Torre Jorgenson et al. "Resilience and vulnerability of permafrost to climate change". In: *Canadian Journal of Forest Research* 40.7 (2010), pp. 1219–1236.

[80] Martin Jung et al. "Scaling carbon fluxes from eddy covariance sites to globe: synthesis and evaluation of the FLUXCOM approach". In: *Biogeosciences* 17.5 (2020), pp. 1343–1365.

[81] Anna Karion et al. "Investigating Alaskan methane and carbon dioxide fluxes using measurements from the CARVE tower". In: *Atmospheric Chemistry and Physics* 16.8 (2016), pp. 5383–5398.

[82] Charles D Keeling, JFS Chin, and TP Whorf. "Increased activity of northern vegetation inferred from atmospheric CO2 measurements". In: *Nature* 382.6587 (1996), pp. 146–149.

[83] TF Keenan and WJ Riley. "Greening of the land surface in the world's cold regions consistent with recent warming". In: *Nature climate change* 8.9 (2018), pp. 825–828.

[84] Frida Keuper et al. "A frozen feast: Thawing permafrost increases plant-available nitrogen in subarctic peatlands". In: *Global Change Biology* 18.6 (2012), pp. 1998–2007.

[85] Miko UF Kirschbaum. "The temperature dependence of soil organic matter decomposition, and the effect of global warming on soil organic C storage". In: *Soil Biology and biochemistry* 27.6 (1995), pp. 753–760.

[86] Venkata Shashank Konduri and Jitendra Kumar. *Hyperspectral remote sensing based vegetation communities around NGEE-Arctic intensive research watersheds at Seward Peninsula, Alaska*. Tech. rep. Next Generation Ecosystem Experiments Arctic Data Collection, Oak Ridge National Laboratory, U.S. Department of Energy, Oak Ridge, Tennessee, USA., 2017. URL: `https://doi.org/10.5440/1828604`.

[87] Rick Lader et al. "Two-meter temperature and precipitation from atmospheric reanalysis evaluated for Alaska". In: *Journal of Applied Meteorology and Climatology* 55.4 (2016), pp. 901–922.

[88] MJ Lara et al. "Local-scale Arctic tundra heterogeneity affects regional-scale carbon dynamics". In: *Nature communications* 11.1 (2020), pp. 1–10.

[89] Klaus S Larsen et al. "Nitrogen uptake during fall, winter and spring differs among plant functional groups in a subarctic heath ecosystem". In: *Ecosystems* 15.6 (2012), pp. 927–939.

[90] David M Lawrence et al. "Permafrost thaw and resulting soil moisture changes regulate projected high-latitude CO2 and CH4 emissions". In: *Environmental Research Letters* 10.9 (2015), p. 094011.

[91] Hanna Lee et al. "Effects of excess ground ice on projections of permafrost in a warming climate". In: *Environmental Research Letters* 9.12 (2014), p. 124006.

[92] A Joshua Leffler et al. "Coupled long-term summer warming and deeper snow alters species composition and stimulates gross primary productivity in tussock tundra". In: *Oecologia* 181.1 (2016), pp. 287–297.

[93] Emmanuel Léger et al. "A distributed temperature profiling method for assessing spatial variability in ground temperatures in a discontinuous permafrost region of Alaska". In: *The Cryosphere* 13.11 (2019), pp. 2853–2867.

[94] Tapio Linkosalo et al. "The time series of flowering and leaf bud burst of boreal trees (1846–2005) support the direct temperature observations of climatic warming". In: *Agricultural and forest meteorology* 149.3-4 (2009), pp. 453–461.

[95] Shishi Liu et al. "The Unified North American Soil Map and its implication on the soil organic carbon stock in North America". In: *Biogeosciences* 10.5 (2013), pp. 2915–2930.

[96] Zhihua Liu et al. "Increased high-latitude photosynthetic carbon gain offset by respiration carbon loss during an anomalous warm winter to spring transition". In: *Global Change Biology* 26.2 (2020), pp. 682–696.

[97] Z Luo et al. "Convergent modelling of past soil organic carbon stocks but divergent projections". In: *Biogeosciences* 12.14 (2015), pp. 4373–4383.

[98] Andrey V Malyshev and Hugh AL Henry. "Frost damage and winter nitrogen uptake by the grass Poa pratensis L.: consequences for vegetative versus reproductive growth". In: *Plant Ecology* 213.11 (2012), pp. 1739–1747.

[99] A David McGuire et al. "Dependence of the evolution of carbon dynamics in the northern permafrost region on the trajectory of climate change". In: *Proceedings of the National Academy of Sciences* 115.15 (2018), pp. 3882–3887.

[100] AD McGuire et al. "An assessment of the carbon balance of Arctic tundra: comparisons among observations, process models, and atmospheric inversions". In: *Biogeosciences* 9.8 (2012), pp. 3185–3204.

[101] Robert B McKane et al. "Resource-based niches provide a basis for plant species diversity and dominance in arctic tundra". In: *Nature* 415.6867 (2002), pp. 68–71.

[102] Zelalem A Mekonnen, Robert F Grant, and Christopher Schwalm. "Sensitivity of modeled NEP to climate forcing and soil at site and regional scales: Implications for upscaling ecosystem models". In: *Ecological Modelling* 320 (2016), pp. 241–257.

[103] Zelalem A Mekonnen, William J Riley, and Robert F Grant. "21st century tundra shrubification could enhance net carbon uptake of North America Arctic tundra under an RCP8. 5 climate trajectory". In: *Environmental Research Letters* 13.5 (2018), p. 054029.

[104] Zelalem A Mekonnen, William J Riley, and Robert F Grant. "Accelerated nutrient cycling and increased light competition will lead to 21st century shrub expansion in North American Arctic tundra". In: *Journal of Geophysical Research: Biogeosciences* 123.5 (2018), pp. 1683–1701.

[105] Zelalem A Mekonnen et al. "Arctic tundra shrubification: a review of mechanisms and impacts on ecosystem carbon balance". In: *Environmental Research Letters* 16.5 (2021), p. 053001.

[106] Zelalem A Mekonnen et al. "Changes in precipitation and air temperature contribute comparably to permafrost degradation in a warmer climate". In: *Environmental Research Letters* 16.2 (2021), p. 024008.

[107] Zelalem A Mekonnen et al. "Expansion of high-latitude deciduous forests driven by interactions between climate warming and fire". In: *Nature plants* 5.9 (2019), pp. 952–958.

[108] Zelalem A Mekonnen et al. "Topographical controls on hillslope-scale hydrology drive shrub distributions on the Seward peninsula, Alaska". In: *Journal of Geophysical Research: Biogeosciences* 126.2 (2021), e2020JG005823.

[109] KA Metivier, E Pattey, and RF Grant. "Using the ecosys mathematical model to simulate temporal variability of nitrous oxide emissions from a fertilized agricultural soil". In: *Soil Biology and Biochemistry* 41.12 (2009), pp. 2370–2386.

[110] Carl J Mikan, Joshua P Schimel, and Allen P Doyle. "Temperature controls of microbial respiration in arctic tundra soils above and below freezing". In: *Soil biology and biochemistry* 34.11 (2002), pp. 1785–1795.

[111] Scot M Miller et al. "A multiyear estimate of methane fluxes in Alaska from CARVE atmospheric observations". In: *Global Biogeochemical Cycles* 30.10 (2016), pp. 1441–1453.

[112] Umakant Mishra et al. "Ensemble machine learning approach improves predicted spatial variation of surface soil organic carbon stocks in data-limited northern circumpolar region". In: *Frontiers in big Data* (2020), p. 40.

[113] Umakant Mishra et al. "Spatial heterogeneity and environmental predictors of permafrost region soil organic carbon stocks". In: *Science advances* 7.9 (2021), eaaz5236.

[114] Max D Morris. "Factorial sampling plans for preliminary computational experiments". In: *Technometrics* 33.2 (1991), pp. 161–174.

[115] Isla H Myers-Smith and David S Hik. "Shrub canopies influence soil temperatures but not nutrient dynamics: an experimental test of tundra snow–shrub interactions". In: *Ecology and Evolution* 3.11 (2013), pp. 3683–3700.

[116] Ranga B Myneni et al. "Increased plant growth in the northern high latitudes from 1981 to 1991". In: *Nature* 386.6626 (1997), pp. 698–702.

[117] Dilip GT Naidu and Sumanta Bagchi. "Greening of the earth does not compensate for rising soil heterotrophic respiration under climate change". In: *Global Change Biology* 27.10 (2021), pp. 2029–2038.

[118] Susan M Natali et al. "Large loss of CO2 in winter observed across the northern permafrost region". In: *Nature Climate Change* 9.11 (2019), pp. 852–857.

[119] Loıc Nazaries et al. "Methane, microbes and models: fundamental understanding of the soil methane cycle for future predictions". In: *Environmental microbiology* 15.9 (2013), pp. 2395–2417.

[120] Scott C Neubauer. "Global warming potential is not an ecosystem property". In: *Ecosystems* (2021), pp. 1–11.

[121] Sonia Nobrega and Paul Grogan. "Landscape and ecosystem-level controls on net carbon dioxide exchange along a natural moisture gradient in Canadian low arctic tundra". In: *Ecosystems* 11.3 (2008), pp. 377–396.

[122] Kimberly Ann Novick et al. "The AmeriFlux network: A coalition of the willing". In: *Agricultural and Forest Meteorology* 249 (2018), pp. 444–456.

[123] HB O'Neill and Christopher R Burn. "Talik formation at a snow fence in continuous permafrost, Western Arctic Canada". In: *Permafrost and Periglacial Processes* 28.3 (2017), pp. 558–565.

[124] Nicholas C Parazoo et al. "Detecting the permafrost carbon feedback: talik formation and increased cold-season respiration as precursors to sink-to-source transitions". In: *The Cryosphere* 12.1 (2018), pp. 123–144.

[125] Hotaek Park et al. "Modeling the effect of moss cover on soil temperature and carbon fluxes at a tundra site in northeastern Siberia". In: *Journal of Geophysical Research: Biogeosciences* 123.9 (2018), pp. 3028–3044.

[126] Richard G Pearson et al. "Shifts in Arctic vegetation and associated feedbacks under climate change". In: *Nature climate change* 3.7 (2013), pp. 673–677.

[127] Olli Peltola et al. "Monthly gridded data product of northern wetland methane emissions based on upscaling eddy covariance observations". In: *Earth System Science Data* 11.3 (2019), pp. 1263–1289.

[128] Shilong Piao et al. "Growing season extension and its impact on terrestrial carbon cycle in the Northern Hemisphere over the past 2 decades". In: *Global Biogeochemical Cycles* 21.3 (2007).

[129] Shilong Piao et al. "Leaf onset in the northern hemisphere triggered by daytime temperature". In: *Nature communications* 6.1 (2015), pp. 1–8.

[130] Eric W Pop, Steven F Oberbauer, and Gregory Starr. "Predicting vegetative bud break in two arctic deciduous shrub species, Salix pulchra and Betula nana". In: *Oecologia* 124.2 (2000), pp. 176–184.

[131] Sarunas J Raudys, Anil K Jain, et al. "Small sample size effects in statistical pattern recognition: Recommendations for practitioners". In: *IEEE Transactions on pattern analysis and machine intelligence* 13.3 (1991), pp. 252–264.

[132] O Reitz et al. "Upscaling net ecosystem exchange over heterogeneous landscapes with machine learning". In: *Journal of Geophysical Research: Biogeosciences* 126.2 (2021), e2020JG005814.

[133] William J Riley, Qing Zhu, and JY Tang. "Weaker land–climate feedbacks from nutrient uptake during photosynthesis-inactive periods". In: *Nature Climate Change* 8.11 (2018), pp. 1002–1006.

[134] William J Riley et al. "Non-growing season plant nutrient uptake controls Arctic tundra vegetation composition under future climate". In: *Environmental Research Letters* 16.7 (2021), p. 074047.

[135] Joeri Rogelj et al. "Estimating and tracking the remaining carbon budget for stringent climate targets". In: *Nature* 571.7765 (2019), pp. 335–342.

[136] Matthew G Rollins. "LANDFIRE: a nationally consistent vegetation, wildland fire, and fuel assessment". In: *International Journal of Wildland Fire* 18.3 (2009), pp. 235–249.

[137] VE Romanovsky and TE Osterkamp. "Interannual variations of the thermal regime of the active layer and near-surface permafrost in northern Alaska". In: *Permafrost and Periglacial Processes* 6.4 (1995), pp. 313–335.

[138] Vladimir Romanovsky, William Cable, and Kirill Dolgikh. *Soil Temperature and Moisture, Teller Road Mile Marker 27, Seward Peninsula, Alaska, beginning 2016.* Tech. rep. Next Generation Ecosystem Experiments Arctic Data Collection, Oak Ridge National Laboratory, U.S. Department of Energy, Oak Ridge, Tennessee, USA., 2022. URL: `https://doi.org/10.5440/1581437`.

[139] MV Ruano et al. "An improved sampling strategy based on trajectory design for application of the Morris method to systems with many input factors". In: *Environmental Modelling & Software* 37 (2012), pp. 103–109.

[140] TS Sazonova and VE Romanovsky. "A model for regional-scale estimation of temporal and spatial variability of active layer thickness and mean annual ground temperatures". In: *Permafrost and Periglacial Processes* 14.2 (2003), pp. 125–139.

[141] Garry L Schaefer, Michael H Cosh, and Thomas J Jackson. "The USDA natural resources conservation service soil climate analysis network (SCAN)". In: *Journal of Atmospheric and Oceanic Technology* 24.12 (2007), pp. 2073–2077.

[142] Andrew E Schuh et al. "Quantifying the impact of atmospheric transport uncertainty on CO2 surface flux estimates". In: *Global biogeochemical cycles* 33.4 (2019), pp. 484–500.

[143] Edward AG Schuur et al. "Climate change and the permafrost carbon feedback". In: *Nature* 520.7546 (2015), pp. 171–179.

[144] Mark C Serreze and Roger G Barry. "Processes and impacts of Arctic amplification: A research synthesis". In: *Global and planetary change* 77.1-2 (2011), pp. 85–96.

[145] MC Serreze et al. "The emergence of surface-based Arctic amplification". In: *The Cryosphere* 3.1 (2009), pp. 11–19.

[146] USDA Natural Resources Conservation Service. *SNOwpack TELemetry Network (SNOTEL)*. Tech. rep. NRCS, 2020. URL: `https://data.nal.usda.gov/dataset/snowpack-telemetry-network-snotel`.

[147] Drew T Shindell, Bernadette P Walter, and Greg Faluvegi. "Impacts of climate change on methane emissions from wetlands". In: *Geophysical Research Letters* 31.21 (2004).

[148] Ian A Shirley et al. "Rapidly changing high-latitude seasonality: implications for the 21st century carbon cycle in Alaska". In: *Environmental Research Letters* 17.1 (2022), p. 014032.

[149] LC Slivinski et al. "An evaluation of the performance of the twentieth century reanalysis version 3". In: *Journal of Climate* 34.4 (2021), pp. 1417–1438.

[150] MW Smith and DW Riseborough. "Climate and the limits of permafrost: a zonal analysis". In: *Permafrost and Periglacial Processes* 13.1 (2002), pp. 1–15.

[151] Sharon L Smith et al. "The changing thermal state of permafrost". In: *Nature Reviews Earth & Environment* 3.1 (2022), pp. 10–23.

[152] Gustav Strandberg and Petter Lind. "The importance of horizontal model resolution on simulated precipitation in Europe–from global to regional models". In: *Weather and Climate Dynamics* 2.1 (2021), pp. 181–204.

[153] George Sugihara et al. "Detecting causality in complex ecosystems". In: *science* 338.6106 (2012), pp. 496–500.

[154] Jinyun Tang and Qianlai Zhuang. "Equifinality in parameterization of process-based biogeochemistry models: A significant uncertainty source to the estimation of regional carbon dynamics". In: *Journal of Geophysical Research: Biogeosciences* 113.G4 (2008).

[155] KEN Tape, Matthew Sturm, and Charles Racine. "The evidence for shrub expansion in Northern Alaska and the Pan-Arctic". In: *Global change biology* 12.4 (2006), pp. 686–702.

[156] Brian Taras, Matthew Sturm, and Glen E Liston. "Snow–ground interface temperatures in the Kuparuk River Basin, arctic Alaska: Measurements and model". In: *Journal of Hydrometeorology* 3.4 (2002), pp. 377–394.

[157] Thejna Tharammal et al. "A review of the major drivers of the terrestrial carbon uptake: model-based assessments, consensus, and uncertainties". In: *Environmental Research Letters* 14.9 (2019), p. 093005.

[158] JHM Thornley. "A balanced quantitative model for root: shoot ratios in vegetative plants". In: *Annals of Botany* 36.2 (1972), pp. 431–441.

[159] Margaret Susan Torn and F Stuart Chapin III. "Environmental and biotic controls over methane flux from arctic tundra". In: *Chemosphere* 26.1-4 (1993), pp. 357–368.

[160] Gianluca Tramontana et al. "Predicting carbon dioxide and energy fluxes across global FLUXNET sites with regression algorithms". In: *Biogeosciences* 13.14 (2016), pp. 4291–4313.

[161] Claire C Treat et al. "Tundra landscape heterogeneity, not interannual variability, controls the decadal regional carbon balance in the Western Russian Arctic". In: *Global Change Biology* 24.11 (2018), pp. 5188–5204.

[162] Sebastian Uhlemann et al. "Geophysical monitoring shows that spatial heterogeneity in thermohydrological dynamics reshapes a transitional permafrost system". In: *Geophysical Research Letters* 48.6 (2021), e2020GL091149.

[163] Anna M Ukkola et al. "Reduced streamflow in water-stressed climates consistent with CO2 effects on vegetation". In: *Nature Climate Change* 6.1 (2016), pp. 75–78.

[164] Egbert H Van Nes et al. "Causal feedbacks in climate change". In: *Nature Climate Change* 5.5 (2015), pp. 445–448.

[165] Anna-Maria Virkkala et al. "Statistical upscaling of ecosystem CO2 fluxes across the terrestrial tundra and boreal domain: Regional patterns and uncertainties". In: *Global Change Biology* 27.17 (2021), pp. 4040–4059.

[166] Philipp de Vrese et al. "Diverging responses of high-latitude CO 2 and CH 4 emissions in idealized climate change scenarios". In: *The Cryosphere* 15.2 (2021), pp. 1097–1130.

[167] Haruko M Wainwright et al. "Making sense of global sensitivity analyses". In: *Computers & Geosciences* 65 (2014), pp. 84–94.

[168] MP Waldrop et al. "Carbon fluxes and microbial activities from boreal peatlands experiencing permafrost thaw". In: *Journal of Geophysical Research: Biogeosciences* 126.3 (2021), e2020JG005869.

[169] Kang Wang and Gary D Clow. "Newly collected data across Alaska reveal remarkable biases in solar radiation products". In: *International Journal of Climatology* 41.1 (2021), pp. 497–512.

[170] Yunqian Wang et al. "Detecting the causal effect of soil moisture on precipitation using convergent cross mapping". In: *Scientific reports* 8.1 (2018), pp. 1–8.

[171] Yaxing Wei et al. "The North American carbon program multi-scale synthesis and terrestrial model intercomparison project–Part 2: Environmental driver data". In: *Geoscientific Model Development* 7.6 (2014), pp. 2875–2893.

[172] Jane Whitcomb et al. "Wetlands map of Alaska using L-band radar satellite imagery". In: *2007 IEEE International Geoscience and Remote Sensing Symposium*. IEEE. 2007, pp. 2487–2490.

[173] William R Wieder et al. "Effects of model structural uncertainty on carbon cycle projections: biological nitrogen fixation as a case study". In: *Environmental Research Letters* 10.4 (2015), p. 044016.

[174] Alexander J Winkler et al. "Earth system models underestimate carbon fixation by plants in the high latitudes". In: *Nature Communications* 10.1 (2019), pp. 1–8.

[175] Lei Xu et al. "In-situ and triple-collocation based evaluations of eight global root zone soil moisture products". In: *Remote Sensing of Environment* 254 (2021), p. 112248.

[176] Xiyan Xu et al. "Heterogeneous spring phenology shifts affected by climate: supportive evidence from two remotely sensed vegetation indices". In: *Environmental Research Communications* 1.9 (2019), p. 091004.

[177] Xiyan Xu et al. "Observed and simulated sensitivities of spring greenup to preseason climate in northern temperate and boreal regions". In: *Journal of Geophysical Research: Biogeosciences* 123.1 (2018), pp. 60–78.

[178] Kai Yan et al. "Evaluation of MODIS LAI/FPAR product collection 6. Part 2: Validation and intercomparison". In: *Remote Sensing* 8.6 (2016), p. 460.

[179] Jiye Zeng et al. "Global terrestrial carbon fluxes of 1999–2019 estimated by upscaling eddy covariance data with a random forest". In: *Scientific data* 7.1 (2020), pp. 1–11.

[180] Runze Zhang, Seokhyeon Kim, and Ashish Sharma. "A comprehensive validation of the SMAP Enhanced Level-3 Soil Moisture product using ground measurements over varied climates and landscapes". In: *Remote sensing of environment* 223 (2019), pp. 82–94.

[181] Yao Zhang et al. "Light limitation regulates the response of autumn terrestrial carbon uptake to warming". In: *Nature Climate Change* 10.8 (2020), pp. 739–743.

[182] Dan Zhu et al. "Controls of soil organic matter on soil thermal dynamics in the northern high latitudes". In: *Nature communications* 10.1 (2019), pp. 1–9.

[183] SC Zoltai. "Cyclic development of permafrost in the peatlands of northwestern Alberta, Canada". In: *Arctic and Alpine Research* 25.3 (1993), pp. 240–246.